DYNAMICS OF VORTEX CAVITATION

DYNAMICS OF VORTEX CAVITATION

Proefschrift

ter verkrijging van de graad van doctor
aan de Technische Universiteit Delft,
op gezag van de Rector Magnificus prof. ir. K.C.A.M. Luyben,
voorzitter van het College voor Promoties,
in het openbaar te verdedigen op woensdag 6 april 2016 om 15:00 uur

door

Pepijn Christianus PENNINGS

Werktuigkundig Ingenieur,
Universiteit Twente, Nederland
geboren te Enkhuizen, Nederland

Dit proefschrift is goedgekeurd door de

promotor: prof. dr. ir. T.J.C. van Terwisga
promotor: prof. dr. ir. J. Westerweel

Samenstelling promotiecommissie:

Rector Magnificus,	voorzitter
Prof. dr. ir. T.J.C. van Terwisga,	Technische Universiteit Delft
Prof. dr. ir. J. Westerweel,	Technische Universiteit Delft
Onafhankelijke leden:	
Prof. dr. ir. R. Bensow,	Chalmers University of Technology
Prof. ir. J. Carlton,	City University London
Prof. dr. ir. H.W.M. Hoeijmakers,	Universiteit Twente
Prof. dr. M. Versluis,	Universiteit Twente
Prof. dr. ir. G.J.F. van Heijst,	Technische Universiteit Eindhoven
Reserve lid:	
Prof. dr. ir. B.J. Boersma,	Technische Universiteit Delft

Prof. dr. ir. T.J.C. van Terwisga en Prof. dr. ir. J. Westerweel hebben in belangrijke mate aan de totstandkoming van het proefschrift bijgedragen.

This research was funded by Lloyd's Register Foundation as part of a cooperation in the International Institute for Cavitation Research.

Keywords: cavitation, hydrodynamic noise, vortex dynamics

Printed by: Gildeprint Drukkerijen

Front & Back: Shadowgraphy of a tip vortex cavity trailing a stationary wing at incidence. Reproduced from Journal of Fluid Mechanics **778**, 288–313 (2015). http://dx.doi.org/10.1017/jfm.2015.379.

ISBN 978-94-6186-619-6

An electronic version of this dissertation is available at
http://repository.tudelft.nl/.

CONTENTS

SUMMARY

This thesis describes the mechanisms with which tip vortex cavitation is responsible for broadband pressure fluctuations on ship propellers. Hypotheses for these are described in detail by Bosschers (2009). Validation is provided by three main cavitation-tunnel experiments, one on a model propeller and two on a stationary wing. These have resulted in a model that can quantify the resonance frequency of a tip vortex cavity based on a limited number of propeller related parameters.

Simultaneous measurement of sound and high-speed video recordings of propeller tip-vortex cavitation were performed, in the presence and absence of an upstream wake inflow. In uniform inflow no significant sound production was observed. For conditions of wake inflow a strong tonal sound was measured that decreases in frequency as the cavitation number decreases. In the frequency domain there was a 30 dB increase over a broadband range surrounding the tonal frequency. This tonal sound was directly related to the tip-vortex cavity-diameter oscillations downstream of the wake. The model described in chapter 2, based on a resonance frequency of a tip vortex cavity, accurately describes the dominant sound frequencies.

The basis for the model are the dispersion relations of three deformation modes. The relations were found experimentally in the frequency and wave number domain of cavity-diameter fluctuations obtained from high-speed video on a fixed wing. Resonance of the tip vortex cavity occurs at zero group velocity of the volume variation mode ($n = 0^-$). This resonance frequency was obtained experimentally while a significant sound source was absent. The quantitative model input for the cavity angular velocity was the single fitted parameter and required validation.

Validation was performed by measurement of the flow field of a tip vortex in presence as well as in absence of cavitation. This was achieved by stereo particle image velocimetry in combination with a correlation averaging method. It provided sufficient spatial resolution and accuracy, to show the effect of a tip vortex cavity on the flow field. The tip vortex cavity is surrounded by a region of retarded azimuthal velocity, similar to the viscous core of a vortex without cavitation. The tip-vortex cavity-resonance frequency is underestimated when the measured cavity angular velocity is used. This showed the limits of the dispersion relation model that is based on a potential flow vortex.

An empirical closure was proposed to serve as input for the cavity angular velocity. A Proctor vortex model was used to describe the flow field of the tip vortex without cavitation. This model required the vortex circulation, the propeller diameter and an empirical roll-up parameter β. This model was able to provide the cavity diameter as function of cavitation number. The angular velocity without cavitation at a radius equal to the cavity radius, was used as model input for the cavity angular velocity. This closure of the dispersion relation model was able to describe the dominant sound frequencies as found in the model propeller experiment in a wake inflow.

REFERENCES

BOSSCHERS, JOHAN 2009 Investigation of Hull Pressure Fluctuations Generated by Cavitating Vortices. In *Proceedings of the First Symposium on Marine Propulsors*. Trondheim, Norway.

SAMENVATTING

Dit proefschrift beschrijft de mechanismen waarmee tipwervelcavitatie verantwoordelijk is voor breedbandige drukfluctuaties op scheepsschroeven. Hypotheses hiervoor zijn gedetailleerd beschreven door Bosschers (2009). Deze zijn gevalideerd door een drietal proeven in een cavitatietunnel, één met een modelschroef en twee met een stationaire vleugel. Deze hebben geresulteerd in een kwantitatief model dat de resonantiefrequentie van een tipwervelcaviteit kan beschrijven, gebaseerd op een beperkt aantal schroefgerelateerde parameters.

Gelijktijdige meting van het geluid en opname van hogesnelheidsvideo van een tipwervelcaviteit van een schroef, zijn uitgevoerd in de aanwezigheid en afwezigheid van een stroomopwaartse instroom met kunstmatig zog. Onder uniforme instroom is er geen significante geluidsproductie van de tipwervelcaviteit geobserveerd. Onder de instroom met zog is een sterk tonaal geluid gemeten dat in frequentie afneemt met het verlagen van het cavitatiegetal. In het frequentiedomein vindt dan een breedbandige amplitudetoename plaats van 30 dB rond de tonale frequentie. Dit tonale geluid is direct gerelateerd aan de oscillaties van de diameter van de tipwervelcaviteit stroomafwaarts van het zog. Het model dat in hoofstuk 2 is beschreven, dat is gebaseerd op de resonantiefrequentie van een tipwervelcaviteit, kan dit dominante geluid nauwkeurig beschrijven.

De basis voor het model zijn de dispersierelaties van drie vervormingsmodi. Deze relaties zijn experimenteel gevonden in het frequentie-golfgetaldomein van de diameterfluctuaties op de tipwervelcaviteit door middel van hogesnelheidsvideo aan een stationaire vleugel. Resonantie van de tipwervelcaviteit vindt plaats op het criterium van nul groepssnelheid van de volumevariatiemodus ($n = 0^-$). Deze resonantiefrequentie is experimenteel geobserveerd onder de afwezigheid van significante geluidsproductie. De kwantitatieve modelinvoer voor de azimutale snelheid op de rand van de tipwervelcaviteit is de enige parameter die is gefit en gevalideerd dient te worden.

Validatie is uitgevoerd door meting van de snelheid rond een tipwervel in de aanwezigheid en afwezigheid van een caviteit in de kern. Dit is bereikt door middel van stereo particle image velocimetry in combinatie met een correlatiemiddelingsmethode. Het geeft voldoende ruimtelijke resolutie en nauwkeurigheid om het effect van de tipwervelcaviteit op het snelheidsveld te laten zien. De tipwervelcaviteit is omgeven met een gebied van vertraagde azimutale stroming, vergelijkbaar met de viskeuze kern van een wervel zonder cavitatie. Wanneer de gemeten azimutale snelheid wordt gebruikt om de resonantiefrequentie van een tipwervelcaviteit te bepalen, dan wordt deze onderschat. Dit laat de beperking zien van het dispersierelatiemodel dat is gebaseerd op potentiaalstroming.

Een alternatieve empirische oplossing is voorgesteld als invoer voor de azimutale snelheid op de rand van de tipwervelcaviteit. Een Proctor wervelmodel is gebruikt om het snelheidsveld te beschrijven van een tipwervel zonder cavitatie. Dit model heeft de

wervelcirculatie, de schroefdiameter en een empirische oprolparameter β nodig. Het model is geschikt om de caviteitdiameter te geven als functie van het cavitatiegetal. De azimutale snelheid zonder cavitatie, op de straal gelijk aan de caviteitstraal, is gebruikt als modelinvoer voor de azimutale snelheid op de tipwervelcaviteit. Deze oplossing voor het dispersierelatiemodel kan de dominante geluidsfrequenties geven die zijn gevonden in de proef met de schroef in een instroom met een zog.

REFERENCES

BOSSCHERS, JOHAN 2009 Investigation of Hull Pressure Fluctuations Generated by Cavitating Vortices. In *Proceedings of the First Symposium on Marine Propulsors*. Trondheim, Norway.

1

INTRODUCTION

A general introduction is given on cavitation. The harmful effects of cavitation result in a specific problem statement for this thesis. To tackle these problems experimentally, upgrades of the facilities were designed and realised. Finally the goals are defined that result in the coherence between three separate experiments.

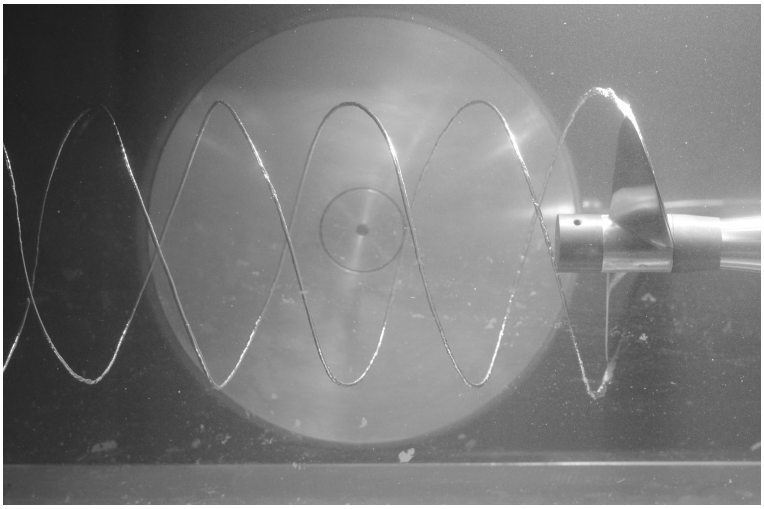

Figure 1.1: Example of propeller tip vortex cavitation. Flow is from right to left. Obtained from experiment in chapter 2.

1.1. CAVITATION

Cavitation is the change in phase from liquid to vapour caused by a reduction in pressure. This process of vapour formation is rapid and leaves the liquid instantly filled with cavities, and the reason the process is called cavitation. This remarkable phenomenon is described by the pioneering experiments of Berthelot (1850).

Cavitation is normally initiated at the site of a cavitation nucleus. This nucleus can be a gas bubble, a solid particle, or an imperfection at a wall. Without these nuclei, water can sustain high tension, as demonstrated in some fundamental experiments by Briggs (1950). The first formation of a cavity at a nucleus is referred to as inception.

In practice liquids contain plenty of nuclei. The combination of nuclei and roughness provides the necessary conditions for cavitation to occur, as visualised by van Rijsbergen & van Terwisga (2011). This is why cavitation usually starts when the pressure locally is reduced to the vapour pressure, the highest pressure at which the vapour phase can be at equilibrium with the liquid phase. Vapour pressure can be reached anywhere where there is a high velocity and thus a low static pressure.

The rotational motion of the fluid in a vortex creates a region of low pressure in the core of the vortex. Vortices can be found in large scale flow with swirling motion, but also in the smaller eddies found in turbulence. This is why inception could take place, at a different location and at a higher pressure than is first estimated based on the mean flow and the vapour pressure (Oweis & Ceccio, 2005). An example of cavitation inside the tip vortices of a propeller is presented in figure 1.1.

Cavitation depends on a large number of parameters and the specific details of the flow. This is why it still receives intensive research effort and plays an important role in challenging engineering applications. A short description of the consequences of cavitation and the various fields in which this is important are described next. For a thor-

ough description of cavitation the reader is referred to Brennen (1995) or Franc & Michel (2004).

Rapid volumetric expansion of a vapour pocket is efficient in producing pressure fluctuations in the surrounding liquid (Chang & Ceccio, 2011). These pressure fluctuations could be a harmonic reaction of the vapour pocket to find an equilibrium size to match the surrounding pressure (Brennen, 1995). Various shapes and sizes of vapour volumes are possible in cavitating flow. The resulting response to unsteady flow or changing conditions gives rise to a very complex emission of pressure fluctuations. These could be in the audible range as harmful noise or excite resonance frequencies of the surrounding structures resulting in vibration (van Wijngaarden *et al.*, 2005; Bosschers, 2007).

The generation and growth of vapour pockets can be a gentle process. When this vapour pocket reaches a region of higher pressure a sudden and violent collapse can occur (Plesset & Prosperetti, 1977). This is often accompanied by large pressure pulses traveling through the surrounding medium influencing other parts of the flow up and downstream of the vapour pocket.

Violent collapse of vapour structures near a surface can eventually lead to cavitation erosion. A detailed phenomenological hypothesis of the transfer of energy from large scale vapour structures to implosion on the surface is given by van Terwisga *et al.* (2009). In this hypothesis vortices of all sizes play an important role in concentrating vapour. The damage from cavitation erosion could cause an increase in frictional drag and eventual propeller or rudder failure.

The classic origin of the interest in cavitation is in engineering, specifically in maritime engineering. In the late eighteen hundreds Sir Charles Parsons encountered major cavitation and thrust breakdown problems when driving the propellers of the steam-turbine-powered ship the Turbinia. The historic context and the engineering problems encountered by Sir Charles Parsons are nicely described in the preface of the work by Foeth (2008) and in more detail by Burrill (1951). Besides cavitation on the propeller, full-scale observations have shown a wide variety of complex flow patterns of cavitation (Fitzsimmons, 2011) and related erosion on rudders and other appendages (Friesch, 2006).

A substantial part of cavitation research is funded by military naval programs (Souders & Platzer, 1981; Sponagle, 1990). Detection of surface vessels at sea by sonar is dependent on the acoustic emissions. When care is taken to reduce other noise sources, detection may be determined by the first occurrence of cavitation. This is usually the vapour formation in the core of the vortices formed at the tip of the propeller, often referred to as vortex cavitation. It is therefore important to be able to accurately predict inception, or to scale inception from model test to full scale.

Propellers with a sharp leading edge produce a strong low-pressure peak. Starting at the leading edge a continuous sheet of vapour could be formed (Foeth, 2008). Depending on the stability of the sheet and the inflow, the sheet could break up into clouds of vapour under the action of shock waves released by a bubble cloud collapse. An example of sheet cavitation breaking up in small patches of cloud cavitation is presented in figure 1.2. If these clouds implode on or near the surface of the propeller risk of erosion is high.

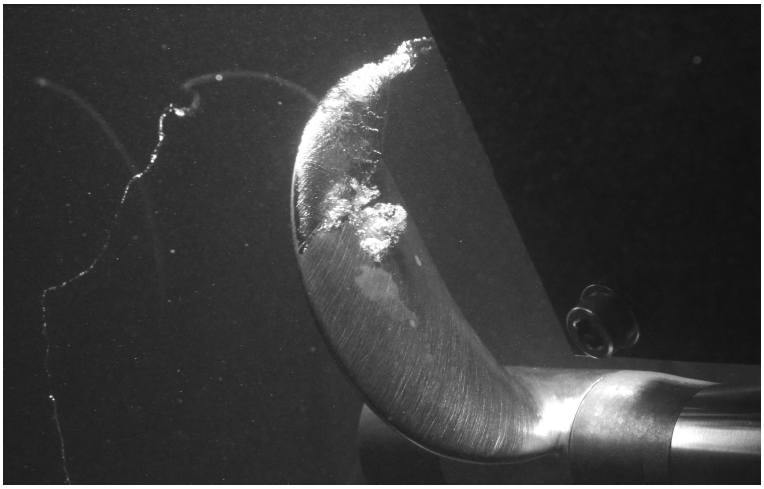

Figure 1.2: Example of typical propeller sheet and tip vortex cavitation behind a wake inflow. Flow from right to left and the propeller rotates counter-clockwise. The leading edge sheet is transported into the tip vortex. Parts that detach from the sheet are referred to as cloud cavitation. In this image the cloudy structure below the sheet could also be travelling bubble cavitation, and is typical for a model propeller without leading edge roughness. Obtained from experiment in chapter 2.

Sheet and cloud cavitation are important in the reliability and longevity of propellers and are therefore main design factors of propellers. Some options to prevent these is to reduce the adverse pressure gradient towards the trailing edge, or to skew the leading edge of the propeller so the sheet is directed towards the tip and feeds into the tip vortex (Kuiper, 2001).

The working principle of a propeller is the pressure difference over the blades. For an unshrouded propeller this means that the formation of a tip vortex created by flow from the high to the low pressure side of the blade is inevitable. Due to the high azimuthal velocity, the tip vortex usually contains the lowest pressure in the flow field. The result is that at higher propeller loading almost all propeller flows contain vortex cavitation.

Vortex cavitation is not as well understood as bubble and sheet cavitation. In some cases vortex cavitation is not harmful. In other cases it is expected to be a source of broadband pressure fluctuations and it can intensify cavitation erosion (Kawanami *et al.*, 1997; van Wijngaarden *et al.*, 2005; Bosschers, 2007). For this reason vortex cavitation is the main focus of the present work.

1.2. PROBLEM STATEMENT

Cavitation nuisance contains three main elements. These are (I) thrust breakdown, (II) the emission of pressure fluctuations resulting in noise and vibrations (III) and the concentrated collapse of vapour near a surface which is potentially erosive. The pressure amplitude and erosive potential due to unsteady sheet and cloud cavitation are the most important characteristics. This has fueled intensive research into understanding the mechanisms of sheet cavity break up and the distinction between dangerous and harm-

less forms of cavitation. The ultimate energy conservation that may lead to cavitation erosion takes place at very short time scales, that pose great challenges to experimental and computational methods. Due to the industrial relevance of cavitation-induced pressure fluctuations and the typically lower frequencies, cavitation erosion was not studied further in the present study.

The formation of sheet cavitation and shedding of vapour clouds is mainly affected by the passing of the propeller blades through the wake of the ship. Another important effect is the intrinsic dynamics of the three dimensional structure of sheet cavitation (Foeth, 2008). The dominant frequencies are often directly related to the blade passing frequency. In the dynamics of ship hull design these frequencies can be taken into account in order to prevent the resonance frequencies of the structure to match the blade passing frequency. The thesis of van Wijngaarden (2011) contains a detailed analysis of hull pressure-fluctuations induced by sheet cavitation. The scope of that study specifically excluded the contribution of vortex cavitation to the pressure fluctuations at multiples of the blade passing frequency. This is the starting point of the current study.

Modern propellers often have a skewed leading edge, resulting in the convection of the leading edge vortex into the tip vortex. The emitted power of pressure fluctuations by a cavitating vortex is usually less than that due to sheet cavitation, but it is not directly, or at least not only, related to the blade passing frequency. The developed cavitating vortex is expected to be responsible for a broadband contribution to the spectrum (van Wijngaarden *et al.*, 2005). Cavitation inception in vortices has different mechanisms of sound production and the interest in cavitation inception is mainly limited to military applications. Inception falls outside the scope of the current study. Understanding of the contribution of vortex cavitation to broadband pressure fluctuations is the main research objective of this study. This required upgrades of the available experimental facility. The process of upgrading of the experimental facility is described in the next section.

1.3. UPGRADES EXPERIMENTAL FACILITY

The first objective was to obtain measurements of sufficient quality of waves on the cavity of a tip vortex in order to validate the model for tip-vortex cavity-resonance. This requires optical access of a sufficient streamwise length of the steady tip vortex cavity.

The cavitation tunnel that was used throughout this study is described in detail by Foeth (2008) and Zverkhovskyi (2014). An image of the tunnel containing the original test section is presented in figure 1.3. The window downstream of the contraction does not provide the required optical access. The shortened diffuser, realised in the study by Zverkhovskyi (2014), allowed for a larger test section. In the scope of the current project the present author designed and realised a new test section for cavitation experiments as presented in figure 1.4.

The results of the experiments in the new test section were utilized to qualitatively validate the model for a tip-vortex cavity-resonance frequency. To quantitatively assess the model, flow field measurements needed to be performed in the region around the steady tip-vortex cavity. The requirement for high spatial resolution in a time averaged method assumed steady conditions. The free stream velocity was known to show a non-periodic decrease of typically 10% of the mean. An example of this phenomenon with a 4% decrease in velocity is shown in figure 1.5. This did not allow for time averaging of

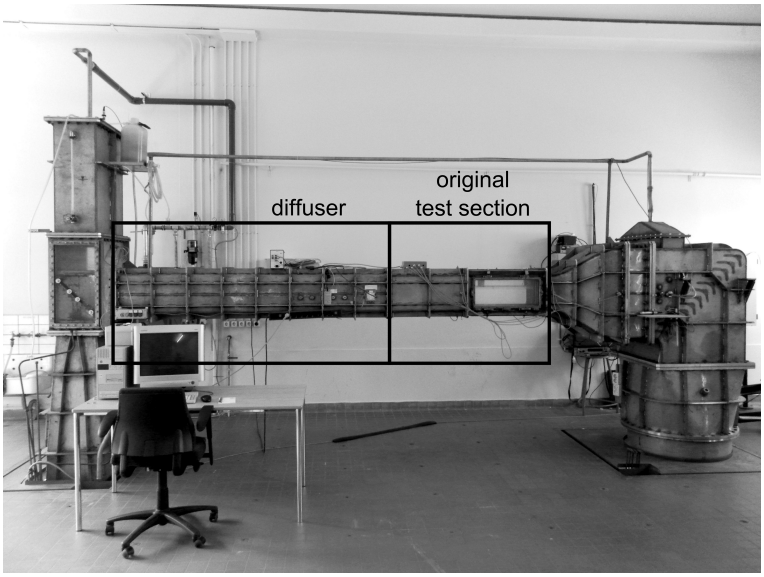

Figure 1.3: Original test section cavitation tunnel. The flow direction is from right to left.

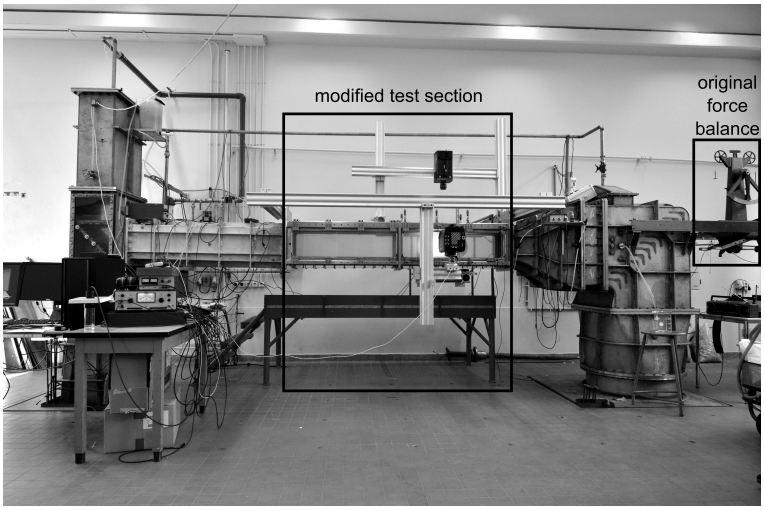

Figure 1.4: Modified test section cavitation tunnel. The flow direction is from right to left.

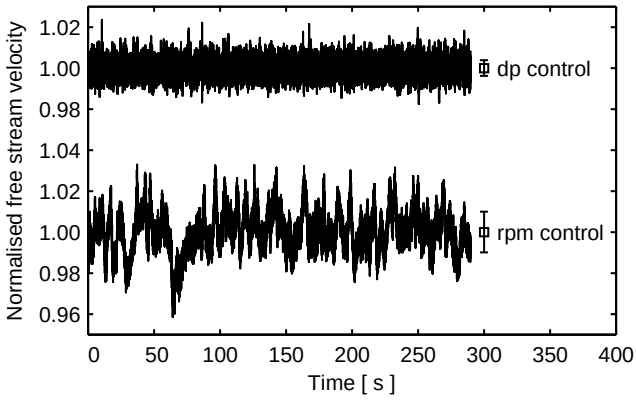

Figure 1.5: Variation in free stream velocity for rotation rate control (rpm control) at 600 revolutions per minute (bottom) and contraction pressure drop control (dp control) (top) at 6 m/s. Both signals are normalised with the mean, that was 6 m/s in both cases.

the data of the flow field measurements.

The origin of the velocity fluctuations was intensively investigated, but it could not be found. Therefore an alternative approach was used, by changing the control system that drives the tunnel impeller. Originally the motor was configured to run at a constant shaft revolution rate. Replacing the motor and motor controller made an analog input available. This analog input was connected to the differential pressure sensor over the contraction of the cavitation tunnel. A closed loop control system was configured to maintain a set pressure drop over the contraction. The difference in the variation of the free stream velocity between the two control systems, i.e. rotation rate and free stream velocity control, is presented in figure 1.5.

The result eliminated the large-amplitude free-stream velocity-fluctuations and reduced the standard deviation to below 0.5% of the mean, that is three times lower in comparison to the value for the original situation. Velocity measurements could then be performed for steady flow conditions. The model for the frequency of tip-vortex cavity-resonance was found not to be quantitatively valid. This is due to the physical limitations in a model that is based on a potential flow vortex. An empirical closure was found by instead using the vortex properties without cavitation rather than the values in the presence of cavitation.

The link between broadband pressure fluctuations and tip-vortex cavity-dynamics was determined in a test employing a model propeller. The model for the frequency of a tip-vortex cavity-resonance requires knowledge of the propeller forces. The cavitation tunnel was previously outfitted with two balance arms. The one that is used for thrust measurements can be seen in figure 1.4 on the right edge of the image on top of the tunnel. A counterweight is placed below one of the wheels of the balance to counteract the propeller thrust. By motion of the arm the thrust can be read from a scale. This system is very well suited for student demonstrations, but suffers from hysteresis and insufficient accuracy. The balance arms were replaced by single-point load-cells. The

resulting electronic signal can be registered by a computer and the load cells require only small shaft displacement, avoiding the hysteresis problem.

1.4. RESEARCH STRUCTURE

The starting point of this study is the modeling effort of Bosschers (2009*a*). Physical mechanisms for vortex cavitation to be responsible for broadband pressure fluctuations are described in detail. At that time of Bosschers (2009*a*) little experimental validation material was available for support. The overall goal of this study is to provide experimental evidence for the contribution of a tip vortex cavity resonance to broadband pressure fluctuations. A detailed literature review is presented in the introduction of chapter 2. The validation tasks for the elements from Bosschers (2009*a*) model are structured as follows:

1. Show the role of propeller tip vortex cavitation in the emission of broadband pressure fluctuations (chapter 2).
2. Develop a model to describe the dominant frequency of sound in broadband pressure fluctuations, based on a limited number of propeller related parameters (chapter 2).
3. Validate this model by experimentally showing the dispersion relations of waves traveling over the vapour-liquid interface of a tip vortex cavity (chapter 3).
4. Experimentally obtain a condition using these dispersion relations that corresponds to a cavity resonance frequency (chapter 3).
5. Configure a vortex velocity model that can close the relation between the description of the tip vortex cavity and the propeller properties (chapter 4).

These goals were pursued in three main experiments. The results of these experimental studies were published in three journal papers. The starting point was the study of Maines & Arndt (1997), on sound production by developed vortex cavitation. A steady tip vortex cavity trailing a stationary wing at incidence was well suited for detailed study. At specific combinations of cavitation number and dissolved oxygen concentration a high amplitude tonal sound was observed. By using simultaneous high-speed video and hydrophone measurements the sound source was identified as tip-vortex cavity-oscillations. This case was ideal for studying sound production by vortex cavitation. Due to the state of the art in high-speed video however, the spatial resolution remained limited. This prevented a detailed analysis of the waves on the vapour-liquid interface at that time.

The first experiment performed in the present study (chapter 3), was a reproduction of the experiment of Maines & Arndt (1997) with modern equipment. The results of attempting to reproduce the production of the strong tonal sound were very disappointing. No sound was observed at any of the documented conditions. To rule out any influence of the experimental facility, the experiment was repeated at CSSRC in Wuxi, China. The first tests confirmed the absence of any significant sound production. Later experiments showed a high sensitivity of the results to the dissolved oxygen concentration.

At very specific combinations of parameters production of vortex-cavity sound could be observed.

The only other approach for tackling this problem originates from the work of Thomson (1880) that describes relations for waves traveling on the interface of a vortex with a hole at its center. This was later modified to include compressibility effects described by Morozov (1974). The final modification was proposed by Bosschers (2009*b*) that included a uniform axial velocity and a correction for the effect of viscosity on the vortex core. The result is a relation between the frequency and the wave number of waves on the interface of the tip-vortex cavity. The dispersion relations were expected to result in a condition for a resonance frequency, but the dispersion relations were not yet obtained in an experiment. Although this was not validated, the implications of the existence of a resonance frequency were already used by Ræstad (1996) and Bosschers (2009*a*) to correlate the broadband hump in the spectrum on full-scale ships to the model. Detailed high-speed video provided the required resolution to study the tip vortex cavity in the frequency - wave number domain.

Validation of the model by Bosschers (2009*a*) still required two elements that the first experiment could not provide. One of the input parameters, the cavity angular velocity at the interface, was not measured. Although the dispersion relations for waves on the interface of the tip vortex cavity could be experimentally identified, the model could not be validated without this parameter. The other missing element, is a confirmation of the criterion for cavity resonance. A dominant frequency was observed in the oscillations of the cavity diameter. However, no dominant tonal sound was observed during these experiments. The quantitative validation of the model for the dispersion relation was pursued in chapter 4.

The same setup was used, but the high-speed cameras were replaced by two conventional cameras for stereo particle image velocimetry. Velocities were measured in an axial cross section of the tip vortex. In the presence of a vapour filled cavity in the vortex center, the cavity angular velocity was measured. When using these findings the dispersion relations of the first experiment were not properly represented. This showed that the model is not quantitatively correct. The limitations of the model are expected to originate from the assumption of a potential flow vortex in the derivation. An empirical correction is proposed to still allow for an estimate of the frequency of the tip-vortex cavity-resonance (chapter 4).

The contribution of vortex cavitation to the production of broadband sound by a propeller is investigated in the last experiment (chapter 2). It was found that the cavity of a steady tip vortex without sufficient excitation does not produce any sound. This was confirmed by a test with a propeller in a uniform inflow resulting in a steady tip vortex cavity. On full scale, excitation is available through the effect of the upstream hull wake. This was represented in the cavitation tunnel by an artificial wake generator. The consequent change in blade loading was sufficiently strong to cause the tip vortex cavity to collapse close to the blade. The center frequency of the dominant sound produced could directly be related to the oscillation of the cavity-diameter of the tip-vortex downstream of the collapse region.

All the mechanisms described by Bosschers (2009*a*) could be found in the time trace of the measured hydrophone signal. Modulation of the phase and amplitude strongly

affect the representation of a tonal signal in the frequency spectrum. While not enough parameters were available to definitively validate the model for the frequency of the tip-vortex cavity-resonance, this experiment demonstrates that the model has the ability to describe the dominant frequencies as function of cavitation number.

The combination of these three experiments provides validation for each of the elements described by Bosschers (2009*a*). This is a solid foundation on which to build a more inclusive understanding of the broadband pressure fluctuations emitted by ship propellers. The next step is concerned with the dynamics of the excitation that affects the frequency band and amplitude of the broadband contribution.

REFERENCES

BERTHELOT, MARCELLIN 1850 Sur Quelques Phénomènes de Dilatation Forcée des Liquides. *Annales de Chimie et de Physique* **30**, 232–237, english translation.

BOSSCHERS, JOHAN 2007 Broadband Hull Pressure Fluctuations and Cavitating Vortices. In *Proceedings of the Ship Noise and Vibration Conference*. London, United Kingdom.

BOSSCHERS, JOHAN 2009*a* Investigation of Hull Pressure Fluctuations Generated by Cavitating Vortices. In *Proceedings of the First Symposium on Marine Propulsors*. Trondheim, Norway.

BOSSCHERS, J. 2009*b* Investigation of the Resonance Frequency of a Cavitating Vortex. In *Proceedings of the NAG/DAGA International Conference on Acoustics*. Rotterdam, The Netherlands.

BRENNEN, CHRISTOPHER E. 1995 *Cavitation and Bubble Dynamics*. Oxford University Press.

BRIGGS, LYMAN J. 1950 Limiting Negative Pressure of Water. *Journal of Applied Physics* **21**, 721–722.

BURRILL, L.C. 1951 Sir Charles Parsons and Cavitation. *Transactions of the Institute of Marine Engineers* **63** (8), 149–167.

CHANG, NATASHA A. & CECCIO, STEVEN L. 2011 The Acoustic Emissions of Cavitation Bubbles in Streched Vortices. *Journal of the Acoustical Society of America* **130** (5), 3209–3219.

FITZSIMMONS, PATRICK 2011 Observations of Cavitation on Propellers. In *Proceedings of the Lloyd's Register Technology Days*, pp. 101–109.

FOETH, EVERT-JAN 2008 The Structure of Three-Dimensional Sheet Cavitation. PhD thesis, Delft University of Technology, Delft, The Netherlands.

FRANC, JEAN-PIERRE & MICHEL, JEAN-MARIE 2004 *Fundamentals of Cavitation*. Kluwer Academic Publishers.

FRIESCH, JUERGEN 2006 Rudder Erosion Damages Caused by Cavitation. In *Proceedings of the Sixth International Symposium on Cavitation*. Wageningen, The Netherlands.

KAWANAMI, Y., KATO, H., YAMAGUCHI, H., TANIMURA, M. & TAGAYA, Y. 1997 Mechanism and Control of Cloud Cavitation. *Journal of Fluids Engineering* **119**, 788–794.

KUIPER, G. 2001 New Developments around Sheet and Tip Vortex Cavitation on Ships' Propellers. In *Proceedings of the Fourth International Symposium on Cavitation*. Pasadena, California, USA.

MAINES, B. & ARNDT, R.E.A. 1997 The Case of the Singing Vortex. *Journal of Fluids Engineering* **119**, 271–276.

MOROZOV, V.P. 1974 Theorectical Analysis of the Acoustic Emission from Cavitating Line Vortices. *Soviet Physics. Acoustics* **19** (5), 468–471.

OWEIS, GRANEM F. & CECCIO, STEVEN L. 2005 Instantaneous and Time-Averaged Flow Fields of Multiple Vortices in the tip Region of a Ducted Propulsor. *Experiments in Fluids* **38**, 615–636.

PLESSET, MILTON S. & PROSPERETTI, ANDREA 1977 Bubble Dynamics and Cavitation. *Annual Review of Fluid Mechanics* **9**, 145–185.

RÆSTAD, ARNT EGIL 1996 Tip Vortex Index - An Engineering Approach to Propeller Noise Prediction. *The Naval Architect* pp. 11–14.

SOUDERS, WILLIAM G. & PLATZER, GREGORY P. 1981 Tip Vortex Cavitation Characteristics and Delay of Inception on a Three-Dimensional Hydrofoil. *Tech. Rep.* DTNSRDC-81/007. David W. Taylor Naval Ship Research and Development Center, Bethesda, Maryland, USA.

SPONAGLE, NEIL C. 1990 Noise from Tip Vortex and Bubble Cavitation. Technical Memorandum 90/202. Defence Research Establishment Atlantic, Dartmouth, Nova Scotia, Canada.

THOMSON, SIR WILLIAM 1880 Vibrations of a Columnar Vortex. *Philosophical Magazine Series 5* **10** (61), 155–168.

VAN RIJSBERGEN, M.X. & VAN TERWISGA, T.J.C. 2011 High-Speed Micro-Scale Observations of Nuclei-Induced Sheet Cavitation. In *Proceedings of the Warwick Innovative Manufacturing Research Centre (WIMRC) Third International Cavitation Forum*. Warwick University, United Kingdom.

VAN TERWISGA, TOM J.C., FITZSIMMONS, PATRICK A., ZIRU, LI & FOETH, EVERT-JAN 2009 Cavitation Erosion – A Review of Physical Mechanisms and Erosion Risk Models. In *Proceedings of the 7th International Symposium on Cavitation*. Ann Arbor, Michigan, USA.

VAN WIJNGAARDEN, ERIK, BOSSCHERS, JOHAN & KUIPER, GERT 2005 Aspects of the Cavitating Propeller Tip Vortex as a Source of Inboard Noise and Vibration. In *Proceedings of the ASME Fluids Engineering Division Summer Meeting and Exhibition*. Houston, Texas, USA.

VAN WIJNGAARDEN, H.C.J. 2011 Prediction of Propeller-Induced Hull Pressure Fluctuations. PhD thesis, Delft University of Technology, Delft, The Netherlands.

ZVERKHOVSKYI, OLEKSANDR 2014 Ship Drag Reduction by Air Cavities. PhD thesis, Delft University of Technology, Delft, The Netherlands.

2

CAVITATION TUNNEL ANALYSIS OF RADIATED SOUND FROM THE RESONANCE OF A PROPELLER TIP VORTEX CAVITY

The goal of this study is to test the hypothesis that the resonance of a tip vortex cavity is responsible for high-amplitude broadband pressure-fluctuations, typically between 40 and 70 Hz, for a full scale propeller. This is achieved with a model propeller in a cavitation tunnel. Simultaneous high-speed video shadowgraphy and sound measurements show that a stationary tip-vortex cavity behind a propeller in a uniform inflow does not produce significant sound in the relevant range of 0.5 to 1.2 kHz. The addition of an upstream wake does result in high amplitude sound. It appears that the dominant frequency of the sound is directly related to the resonance of the tip vortex cavity. A model for the frequency of the tip-vortex cavity-resonance, using the Proctor vortex model, is able to give an accurate description of the frequencies of the dominant sound.

This chapter has been published in International Journal of Multiphase Flow (accepted, in press) Pennings *et al.* (2016). Evert-Jan Foeth, employed at MARIN, designed the model propeller and performed the boundary element method calculations. Marc Timmer performed velocity measurements downstream of the wake field in absence of a propeller as part of his Master of Science research.

2.1. INTRODUCTION

Cavitation has posed limits in propeller performance ever since sufficient power was available at the shaft. It started out with severe loss of thrust, due to the formation of large pockets of water vapor, at locations the local pressure dropped below the vapor pressure. Due to extensive research and practical experience this can be avoided by careful propeller design.

The demand for efficient propulsion has led to the acceptance of moderate forms of cavitation on propellers. This requires detailed understanding of the limiting effects of cavitation nuisance. Erosion can occur when vapor volumes violently implode on the surface of a propeller or hull. This is addressed by altering the overall propeller geometry, as seen in most modern propellers. As the leading edge of the propeller is swept back in the rotation direction, the sheet cavity is convected into the tip vortex, away from the propeller surface.

Large variations in the volume of the sheet cavity are effective sources of high amplitude pressure-fluctuations related to the blade passage frequency. Although quantitative estimation of the amplitude is still a challenge, there is a clear physical understanding of the mechanisms of this sound source.

The transport of vapor from the propeller surface into the tip vortex has a significant side effect in the frequency content of the pressure fluctuations. The oscillation of the vapor volume is no longer solely related to the blade passage frequency, but is also found to occur between the fourth to seventh blade passage harmonics on full-scale ships (van Wijngaarden *et al.*, 2005). Its source is expected to be related to the tip-vortex cavity-dynamics.

Various studies have tried to model this phenomenon experimentally for the model of a fixed wing in a cavitation tunnel. These experiments involved the measurement of sound from a stationary tip vortex cavity. The scope of the present study excluded cavitation inception. Mechanisms of sound production at inception are different from oscillations of a stationary vortex cavity, and the interest in inception is mainly limited to naval applications.

A few typical sources of cavitation sound are studied by Barker (1976). He mentions that a stationary tip vortex cavity does not show the violent collapse of other types of cavitation, and therefore produces less sound. In general, the same was found in a series of other studies on cavitation of stationary trailing tip-vortices (Higuchi *et al.*, 1989; Briançon-Marjollet & Merle, 1997; Maines & Arndt, 1997; Astolfi *et al.*, 1998).

However, there is a very distinct exception, in which the tip vortex cavity oscillates in phase with the sheet cavity attached to the tip. This phenomenon is very sensitive to tunnel conditions and is therefore hard to reproduce. When it occurs the result is the production of high-amplitude tonal sound (Maines & Arndt, 1997). The fundamental study of the mechanisms behind this (Pennings *et al.*, 2015*a*) explains that it is a self excitation of a tip-vortex cavity-resonance frequency. The excitation has not been clearly identified, but it is expected to be related to a sheet cavity related instability of the boundary layer.

At full-scale, the ship Queen Elizabeth 2 provides a striking example of broadband pressure fluctuations (Brubakk & Smogeli, 1988; Ræstad, 1996). After extensive model tests, it was found that the problem was related to the tip vortex cavity. A recent review

of cavitation related problems is given by van Terwisga *et al.* (2007). The starting point of the present study is the work by Bosschers (2009). He outlines the mechanisms with which vortex cavitation can be responsible for broadband pressure fluctuations, based on the amplitude and phase modulation the frequency of a tip-vortex cavity-resonance.

The objective of the present study was pursued with a simplified setup of a modern skewed propeller in wake inflow, to show the source of broadband pressure fluctuations. Using the properties of the propeller and of the tip vortex, the sound source was related to the fundamental mechanisms found for a stationary tip-vortex cavity trailing from a fixed wing (Pennings *et al.*, 2015*a*). To determine this relation, the following three steps were defined:

1. Obtain the necessary parameters to describe the tip-vortex cavity;

2. Show that the broadband pressure fluctuations of propeller cavitation are generated by resonance of the tip vortex cavity;

3. Show that the model for the frequency of the cavity resonance (dispersion relation for the $n = 0^-$ mode at zero group velocity using a vortex model (Proctor)) is capable of describing the measured dominant sound frequencies based on a limited number of propeller-related parameters.

In section 2.2 the tip-vortex cavity-resonance frequency model is described in more detail including the underlying assumptions followed by a description of the experimental setup in section 2.3. The results in section 2.4 are ordered as follows. First, the required model parameters are obtained from measurements in combination with calculations using a boundary element method. Then, it is demonstrated that the oscillations of the tip-vortex cavity are responsible for the dominant sound production. Finally, the frequencies from the model are compared to the results of the sound measurements. This is followed by a discussion on the remaining challenges in section 2.5, and section 2.6 summarizes the conclusions.

2.2. MODEL FREQUENCY OF TIP-VORTEX CAVITY-RESONANCE

A fundamental understanding of the waves on the interface of a tip vortex cavity is required to obtain a resonance frequency. This is described in detail in the study of Pennings *et al.* (2015*a*). The basis of this study was a model for the dispersion of waves consisting of vortex-cavity deformation modes. Some underlying assumptions, which allow for an analytical treatment, are briefly mentioned here. The point of departure for the derivation was a potential flow vortex in a uniform axial flow. To first approximation, the model was shown to be valid for a viscous vortex only for the volume variation mode. The geometry of the deformation of the deformation modes is depicted in Fig. 2.1. The dispersion relations are given by:

$$\omega = W_\infty k_x + \Omega \left[n \pm \sqrt{\frac{-k_r r_c H_n^{1\prime}(k_r r_c)}{H_n^1(k_r r_c)}} \right], \tag{2.1}$$

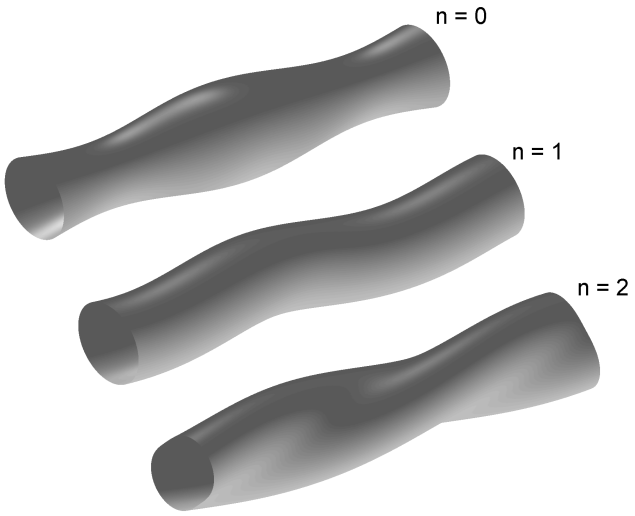

Figure 2.1: Main vortex cavity oscillation modes, reproduced from Bosschers (2008). Top, the monopole breathing mode ($n = 0$); middle, the dipole serpentine centerline displacement mode ($n = 1$) and bottom, the quadrupole helical mode ($n = 2$).

where ω is the frequency, W_∞ is the axial velocity, k_x is the axial wave number , Ω is the vortex-cavity angular-velocity, k_r is the radial wave number and r_c is the cavity radius. H_n^1 and $H_n^{1\prime}$ denote the Hankel function of the first kind and its derivative with respect to it argument r, respectively. There are two solutions for the frequency of each vibration mode as indicated by the plus and minus sign. The sign is also used to identify the mode.

This model is an accurate description of the dispersion relation found experimentally, for the cavitating tip vortex trailing from an elliptical planform wing. It follows from this experiment that a specific value in this dispersion relation consistently coincides with the resonance frequency of oscillations of the tip-vortex cavity. This occurs when the group velocity ($\delta\omega/\delta k_x$) of the $n = 0^-$ mode is equal to zero. The dispersion relations and resonance criterion are shown in Fig. 2.2. The only parameter that was not measured was the vortex-cavity angular-velocity Ω.

The azimuthal velocity at the interface of a tip vortex cavity was measured with stereo particle image velocimetry (Pennings *et al.*, 2015*b*). Using these results the frequency of tip-vortex cavity-resonance was obtained from the model. The model results in an underestimation of the dominant frequency of cavity diameter oscillations. While the model is qualitatively able to describe the physical phenomenon, it is quantitatively inaccurate. The model is derived from a potential flow vortex. In comparison with realistic vortex flow fields the azimuthal velocity near the vortex center is higher. This results in a lower vortex core pressure, and as a result a larger cavity diameter. A larger cavity diameter has a lower resonance frequency. This effect is responsible for the underestimation when compared to experiments. Based on the velocity measurements around

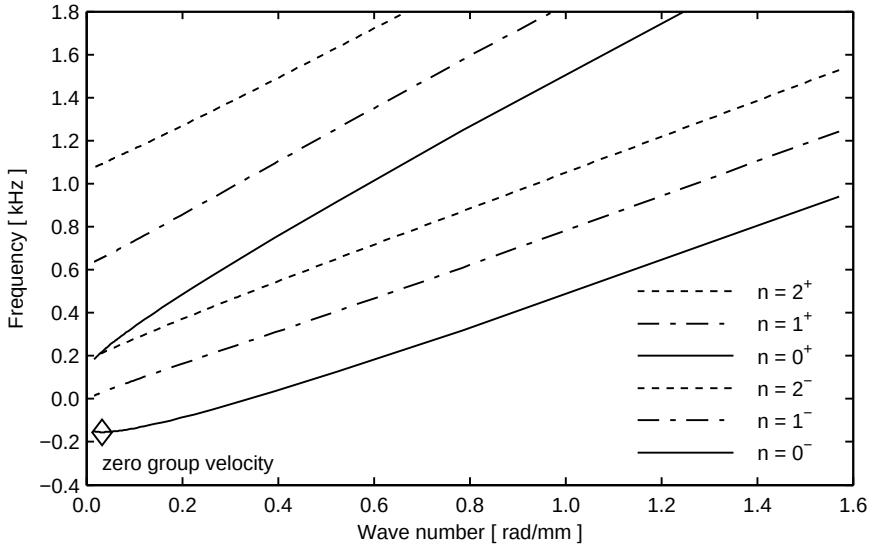

Figure 2.2: Dispersion relations for the two ± branches of the three modes shown in Fig. 2.1, reproduced from Pennings *et al.* (2015*a*). The tip-vortex cavity-resonance criterion of zero group velocity on the $n = 0^-$ mode is indicated by the diamond. Condition; $\Omega = 2.0 \times 10^3$ rad/s, $W_\infty = 6.3$ m/s and $r_c = 2.3$ mm.

vortex cavitation, an alternative correction was proposed.

The model of the resonance frequency can be closed empirically by using a Proctor vortex model. It has been able to provide a relation between the cavity radius and angular velocity, which has resulted in the correct resonance frequency. The azimuthal velocity of a Proctor vortex model is given by:

$$u_\theta(r) = \frac{\Gamma}{2\pi r}\left(1 - exp\left(-\beta\left(\frac{r}{B}\right)^{0.75}\right)\right), \tag{2.2}$$

where Γ is the vortex circulation, r is the radial position, β is the vortex roll-up parameter and B is the wing span. To limit the number of model parameters, the Proctor vortex model is only used outside the viscous core of the vortex. The wing span was taken equal to half the propeller diameter.

The cavity radius, through the pressure in the vortex core, is obtained by numerical integration of the velocity field according to the conservation of radial momentum:

$$\frac{dp}{dr} = \rho\frac{u_\theta^2}{r}, \tag{2.3}$$

where p is the local static pressure, r is the radial position with respect to the vortex center, ρ is the water density and u_θ is the azimuthal velocity. Equation 2.3 valid for axisymmetric flow and zero radial velocity. The location within the vortex core where the local pressure becomes equal to the vapor pressure p_v defines the cavity radius:

$$p(r) = p_\infty - \int_r^\infty \frac{\rho}{r} u_\theta^2(r)\,dr \quad \Rightarrow \quad p_v = p_\infty - \int_{r_c}^\infty \frac{\rho}{r} u_\theta^2(r)\,dr \quad \Rightarrow \quad r_c, \tag{2.4}$$

where p_∞ is the free stream static pressure. The angular velocity of the flow field without cavitation at this location is used as input for the cavity angular velocity.

There is no trivial choice for the value of the circulation of the tip-vortex. Especially in close proximity to the propeller tip, the tip vortex is still in the process of roll-up. The initial roll-up of a vortex sheet trailing from a wing of a large span and elliptical load distribution is described by Wu *et al.* (2006) as the Kaden problem. Most of the assumptions of this analysis do not hold for propeller flow. There is not a constant streamwise velocity for the wake vortex sheet in the propeller frame of reference, the radial load distribution is not elliptical and a propeller blade has a short span.

Due to the rotating frame of reference and the small size of the vortex core, measurements with sufficient accuracy are challenging. Therefore, experimental data is not available for validation of the model values used in the present study. The approach in the present study is to fit the tip-vortex cavity-resonance frequency model to the measured dominant sound frequencies in order to obtain the parameters for the Proctor vortex model. Then the cavity radius that follows from Eqn. 2.4, using Proctor's distribution of the azimuthal velocity, should be equal to the cavity radius obtained from high-speed video. This check is only meant to verify the consistency of the used model.

The number of free parameters in the vortex model is reduced by using the experience on obtaining the vortex circulation from an experimental measurement of the flow field of a tip vortex in close proximity to the tip. From Pennings *et al.* (2015*b*) it was found that the radial-mean of the distribution of circulation of a stationary wing at incidence gave a good description of the tip-vortex velocity field. In the present study it was proposed to obtain the radial-mean of the blade circulation distribution from a boundary element method applied to the propeller in open water.

Now the model only requires an estimate of the vortex roll-up parameter β, which should be obtained empirically. An overview of the model for the resonance frequency and the experimental track that led to broadband pressure fluctuations from vortex cavitation is presented in Fig. 2.3.

2.3. EXPERIMENTAL SETUP

The experiments were performed in the cavitation tunnel at the Delft University of Technology. The tunnel was described in detail by Foeth (2008), while recent modifications were implemented by Zverkhovskyi (2014). A new test section was used, inlet cross-section dimensions of 0.30 m × 0.30 m, the outlet cross-section dimensions are 0.32 m × 0.30 m. The increase in height was used to correct for the growth of the boundary layer on the tunnel wall to achieve a near-zero streamwise pressure-gradient.

A model of a right-handed propeller with two blades is mounted on an upstream shaft. The propeller geometry is presented in Fig. 2.4. The propeller was provided by the Maritime Research Institute Netherlands (MARIN). It was specifically designed to show tip vortex cavitation with the leading-edge sheet-cavity feeding into the tip vortex in a stable fashion.

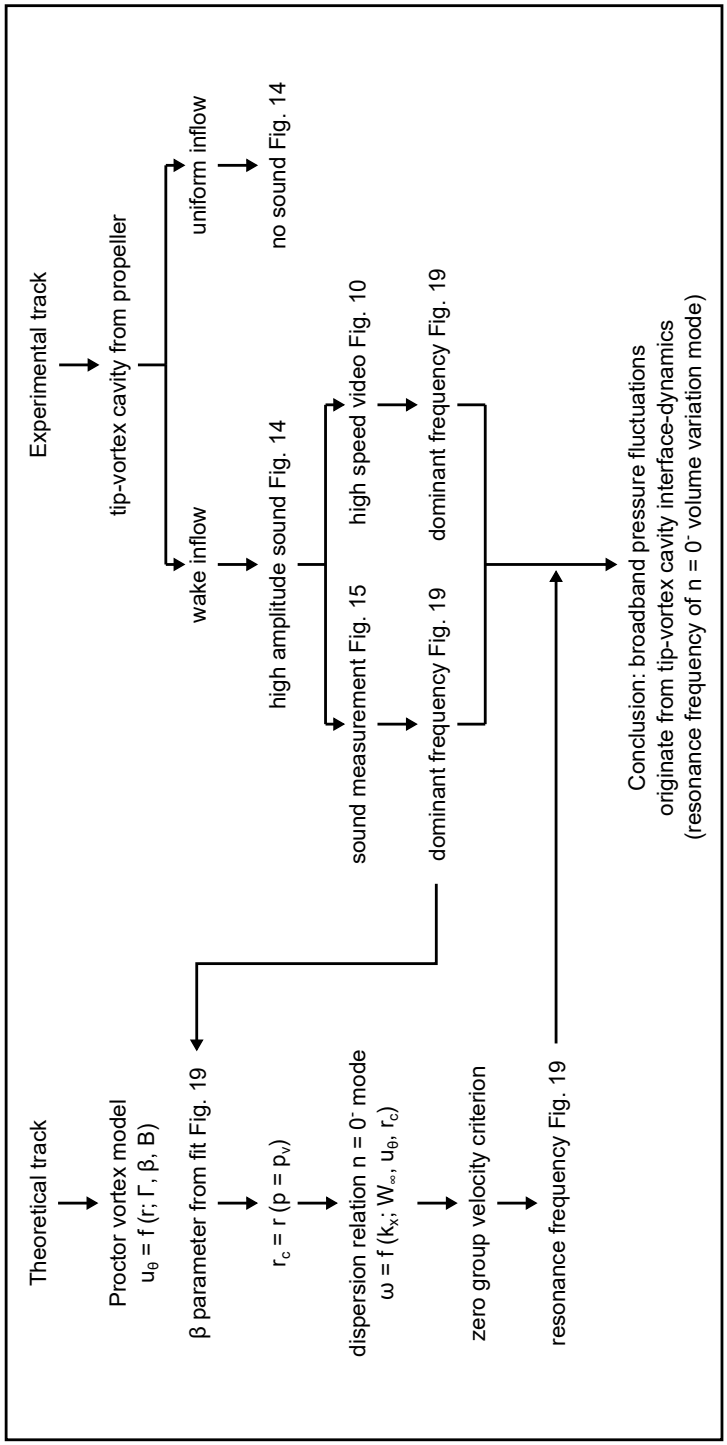

Figure 2.3: Schematic of relations and research activities.

The application of leading edge roughness is a common procedure in testing model propellers. This is to ensure a full scale compatible development of the leading edge sheet cavity despite the absence of a developed turbulent boundary layer. To minimize the contribution of sheet cavitation to the sound production, leading edge roughness was not applied in the present study.

The experimental setup is presented in Fig. 2.5. Propeller thrust and torque were measured on the shaft outside the cavitation tunnel by two single point load cells (Zemic L6D-C3). Empty shaft tests were performed to remove the contributions from the bearing and seal friction torque, and the pressure differential over the shaft seal. The model propeller force sensors were placed outside the tunnel. All tests were performed at a revolution rate of 38 Hz that was limited by the maximum motor torque.

Propeller tests were performed using three inflow conditions: uniform inflow, and two inflow conditions produced by a wake generator. In all of the following results, 5 plates were used except for Fig. 2.17 for which the wake generator consisted of 3 plates. The plates were mounted at 30 degrees before top dead center (TDC), to be able to capture the dynamics of the tip-vortex cavity aside from the propeller shaft. The trailing edge of the plates was placed only 10 mm upstream of the propeller hub, to maximize the effect of the retarded inflow. The streamwise velocity in the wake, in the absence of a propeller, was measured using a Pitot tube. The region of lowest axial velocity (wake peak), has an axial velocity of approximately 0.3 times the free stream velocity, as shown in Fig. 2.6. This region spanned the entire region downstream of the wake generator.

Essential tunnel conditions were measured using a temperature sensor (PT-100), optical Dissolved Oxygen (DO) sensor (RDO Pro), absolute pressure sensor (Keller PAA 33X) at 10 Hz and a differential pressure sensor mounted in the tunnel contraction (Validyne DP 15 with number 36 membrane). Pitot tube reference measurements with an empty shaft were performed to correct the static pressure and water velocity at the location of the propeller.

The outline of the tip vortex cavity was captured by shadowgraphy, using a continuous incandescent light source of 300 W, covered by a roughed plastic diffusing plate in combination with a high-speed video (HSV) camera (Photron APX-RS). This was run at an acquisition frequency of 15 kHz, that was the same for almost all other sensors. Using a 105 mm objective (AF Micro Nikkor 1:2.8 D) at a f-stop of $f/22$ and a focal distance of 0.68 m, resulted in an estimated focal depth of 3 cm. The pixel size of the camera is 17 μm with a cropped image format of 640 × 288 pixels. The pixel size in the object plane was approximately 8 μm.

To accurately determine the cavity diameter, a calibration plate was placed tangent to the estimated path of the tip-vortex cavity at a radius of 71 mm from the shaft. The plane normal at the origin was collinear to the rotation angle of 30 degrees from top dead center. The plate was also at the same angle with the camera, resulting in a perspective effect. The images were transformed to the plane of the calibration plate using the image processing and particle image velocity software, DaVis 8.

A hydrophone (TC4013-4) was mounted on the side window of the cavitation tunnel, in a water filled cup, 5 cm vertically upward from the centerline of the propeller shaft, at the streamwise position equal to that of the blade tip. The sound signal was conditioned with a charge amplifier (Reson EC6067 - CCA 1000) and filtered and amplified with a

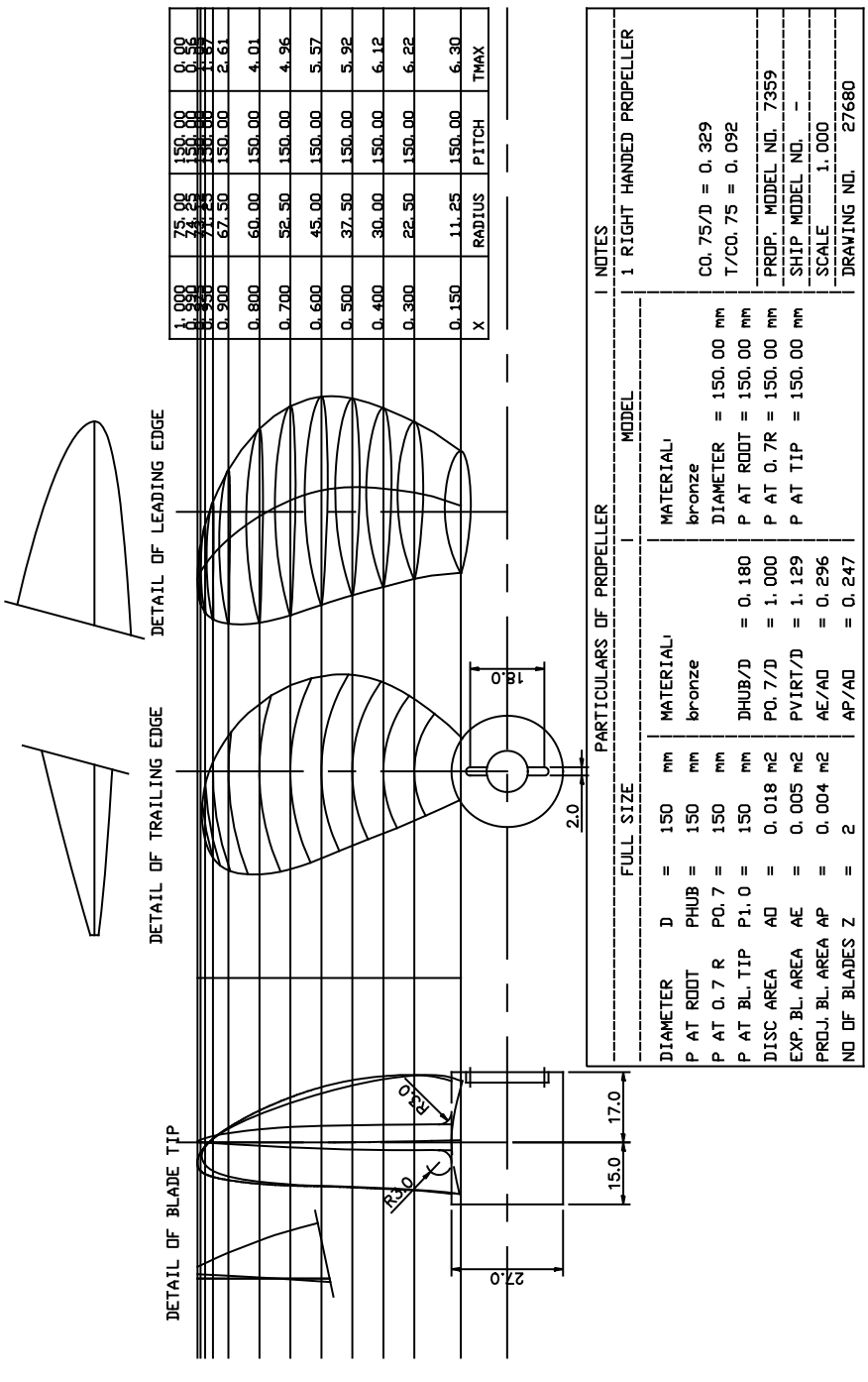

Figure 2.4: Propeller geometry left to right: projection of the rake, projection of the skew and expanded area projection with section profiles. Images of the propeller are presented with cavitation in Fig. 2.11 and Fig. 2.12.

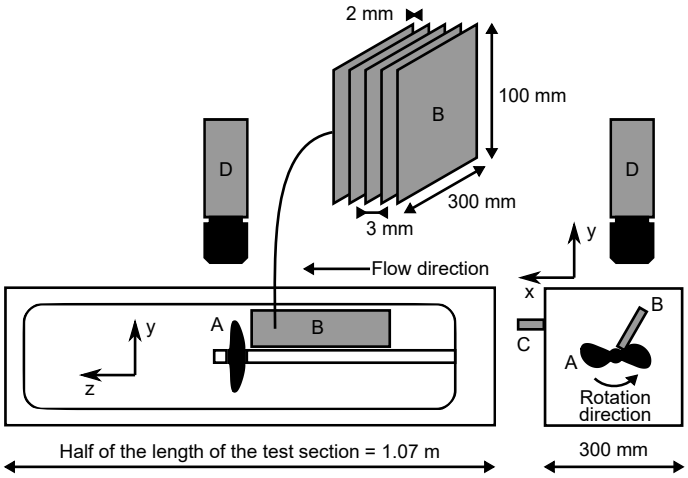

Figure 2.5: Schematic representation of experimental setup (cameras not to scale), with model propeller *A*, series of rectangular wake plates *B*, hydrophone *C* and high speed camera *D*.

Butterworth, 7.5 kHz cut-off low pass filter (Krohn-Hite model 3940).

2.4. RESULTS

The calculation of the resonance frequency, from the model presented in section 2.2, requires the blade circulation and the size of the tip-vortex cavity. The first was obtained by comparing the propeller force measurements to the results of a boundary element method. As the difference in thrust was at most 6 %, the radial-mean of the blade circulation distribution is obtained from the computation. The cavity size was obtained from edge detection in the high-speed video images, resulting in the cavity size as function of cavitation number with and without a wake inflow. With these input values known, the sound spectrum of steady tip vortex cavitation was compared to wake excited cavitation in order to isolate the resulting contribution of the excitation. The dominant sound frequency was then compared to the cavity-diameter oscillation-frequency in the wake region, and to the value obtained from the resonance frequency model.

2.4.1. PROPELLER FORCES

The global properties of the propeller were summarized using essential parameters; the advance ratio $J = W_\infty / nD$, thrust coefficient $K_T = T/(\rho n^2 D^4)$, torque coefficient $K_Q = Q/(\rho n^2 D^5)$, Reynolds number $Re = (c\sqrt{W_\infty^2 + (0.7\pi nD)^2})/\nu$ and cavitation number $\sigma_n = (p_\infty - p_v)/(\frac{1}{2}\rho(nD)^2)$. Here W_∞ is the axial water velocity into the propeller. For both uniform inflow as well as wake inflow, this is taken as the free stream velocity upstream of the wake generator. The propeller rotation rate was n in Hz and the propeller diameter is $D = 0.15\ m$. Fluid properties are density ρ, kinematic viscosity ν, free-stream static-pressure p_∞ and vapor pressure p_v. Propeller thrust is T, torque is Q and the chord c was taken at 70% radius $c = 50.6\ mm$.

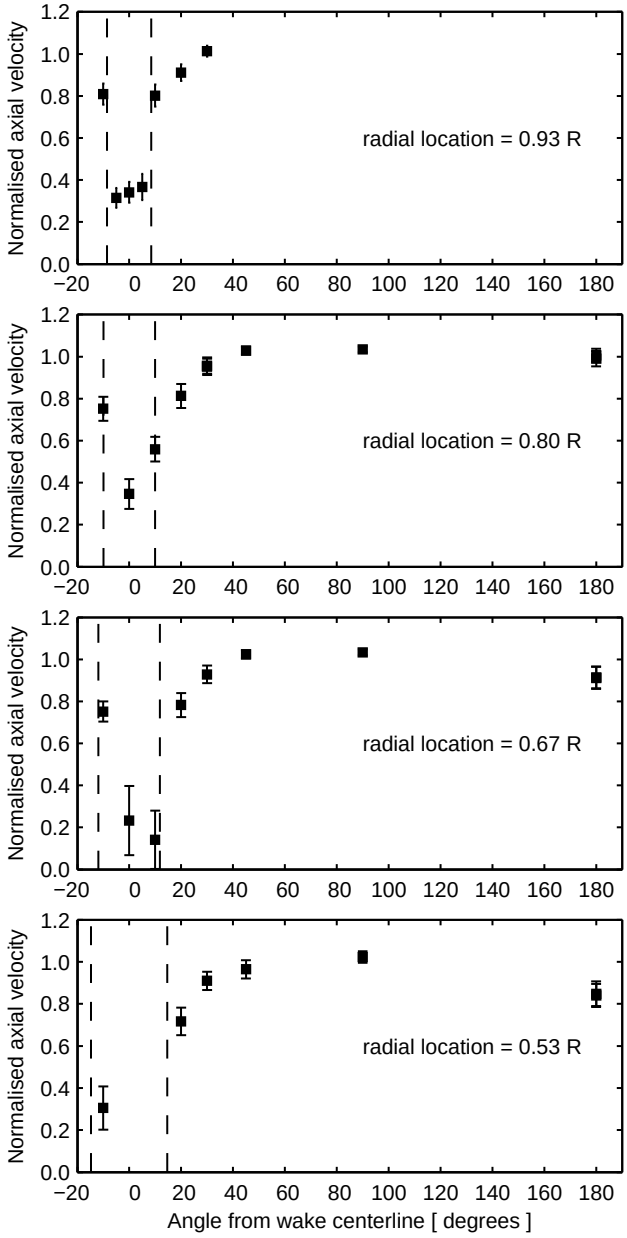

Figure 2.6: Axial velocity 10 mm downstream of the wake at four radial locations ($R = \frac{1}{2}D$), normalised with the undisturbed upstream axial velocity. The vertical dashed lines outlines the region of the wake plates. At $0.67R$ the points at 0 and 10 degrees are influenced by the mounting bolts of the wake generator, therefore these points are not considered at $0.53R$. At 180 degrees, the mounting brackets slow down the flow at these radial locations.

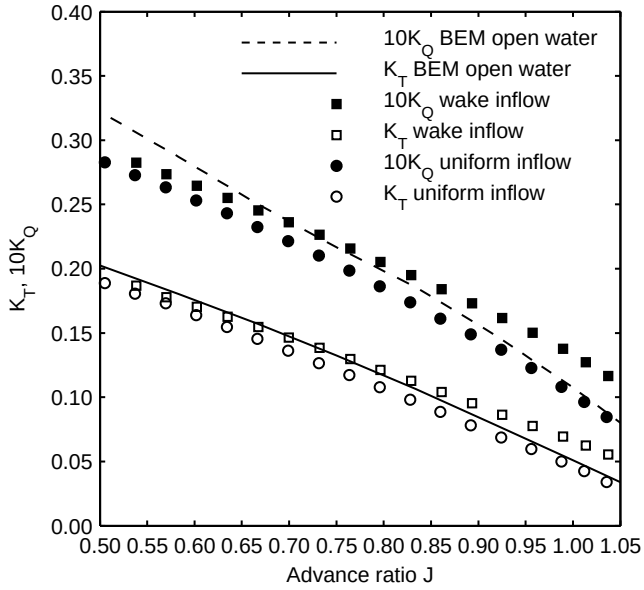

Figure 2.7: Propeller thrust K_T and torque K_Q as function of advance ratio J. Symbols are based on experiment for wake inflow and uniform inflow in the cavitation tunnel and lines are based on results of boundary element method calculations for open water (Procal). Conditions: $Re = 7 \times 10^5$ and $DO = 3\ mg/l$.

For a range of advance ratios, limited by the facility, K_T and K_Q are presented in Fig. 2.7 for uniform inflow and for wake inflow in the cavitation tunnel. Also given is the result from the boundary element method Procal for the open water condition. This method was developed by the Maritime Research Institute Netherlands (MARIN) and is also used by other institutions (Bosschers *et al.*, 2008). Validation studies and details of the mathematical model and numerical method can be found in the thesis of Vaz (2005). Procal is used as a primary design tool for propellers. The results from the boundary element method follow directly from the propeller design at MARIN.

The main difference between the results of the calculations and the results of the measurements is the influence of the tunnel walls. The walls increase the streamwise velocity which results in a reduction of thrust and torque. The blockage effect is strongest for low advance ratios. A common method to account for this difference is to compare cases with equal values of K_T. Then K_Q is within 5% of the measurements, which is the typical accuracy for the propeller used in the present study. The thrust is most relevant and is represented more accurately.

In general, the influence of the wake on the global parameters was small, as expected due to the size of the wake generator. The Taylor wake fraction is estimated to be 0.07 based on the measurements of Fig. 2.6. The effect was smaller for smaller advance ratios, due to the decrease in free stream velocity at constant revolution rate.

The boundary element method results showed a good correspondence to the mea-

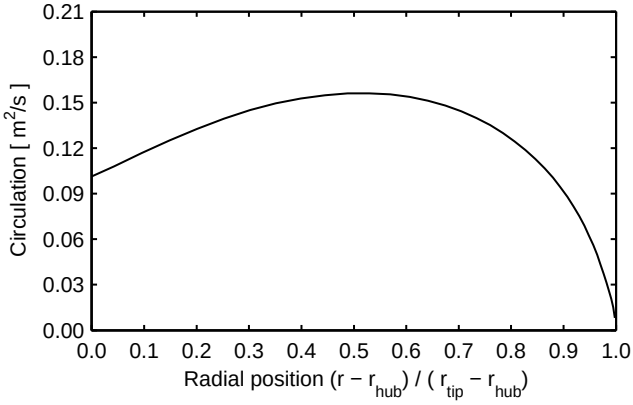

Figure 2.8: Circulation distribution of propeller blade obtained from a boundary element method for open water (Procal). Conditions: $J = 0.56$ and rotation rate is 38 Hz both equal to the values in the experiment.

sured propeller properties. Therefore, the output of the method in terms of the blade loading distribution, given in Fig. 2.8, could be used as an estimate of the circulation of the tip vortex.

There is no general formulation for the relation between the blade loading and the circulation of the tip vortex. The value used in the present study was the radial-mean blade circulation. For various J values this is presented in Fig. 2.9. The radial mean of the circulation distribution was found to be able to describe the tip vortex flow field within 5.5 chord lengths from the tip of a stationary wing at incidence (Pennings *et al.*, 2015*b*).

2.4.2. HIGH-SPEED VIDEO

High-speed video recordings of the tip vortex cavity were used for two main purposes. Firstly, as a reference for the input for the model for the cavity radius. Secondly, to compare the cavity-diameter oscillation behind the wake generator with the measured dominant frequency of the sound produced. This last part is included in subsection 2.4.3 on sound measurements. An overview of three cases with the same conditions is given in Fig. 2.10.

Detection of the edge of the tip-vortex cavity was performed using a Canny (1986) algorithm, with a threshold of 0.2 and a filter size of 4.0. This method is based on detection of intensity gradients in an image. It is well suited for the present application because shadowgraphy provides large gradients between the cavity and the background illumination. The cavity diameter was obtained in the entire field of view, next to the wake inflow and for uniform inflow. Behind the wake generator the increased loading of the blade resulted in a strong growth of the cavity, followed by a violent collapse. The development of the cavity on the leading edge of the propeller blade is presented in Fig. 2.11. The cavity on the propeller for uniform inflow is presented in Fig. 2.12. These results indicated that tip vortex cavitation is the dominant form of cavitation present on the propeller.

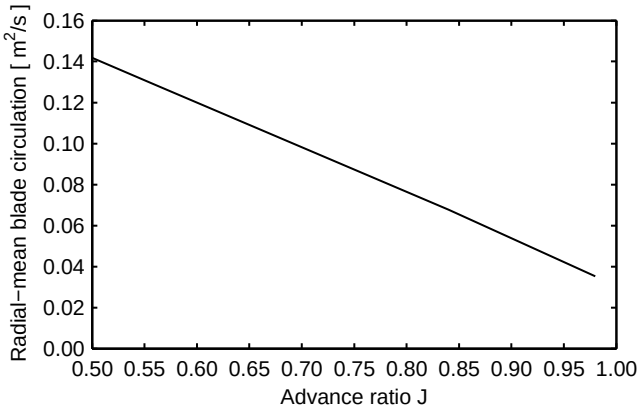

Figure 2.9: Radial-mean propeller blade circulation as function of advance ratio obtained from boundary element method for open water (Procal). The rotation rate of 38 Hz is equal to the value in the experiment.

As seen in the middle image of Fig. 2.10, redistribution of vorticity can cause an irregular edge, and also cavity implosions broke up the continuity of the edge. Therefore, only the part between the vertical lines was analysed, during the part of the blade revolution that was excited by the wake. Forty columns of image pixels were captured during 60 images, resulting in four periods of cavity oscillation.

Figure 2.13 gives the mean cavity radius and its variability. The results based on Proctor's vortex included in the figure was based on a fit of the roll-up parameter β to the sound, as presented in Fig. 2.19.

There was little difference between the size of the cavity for uniform inflow and the size obtained next to the wake. The effect of the narrow wake on the tip-vortex cavity-diameter was essentially confined to region directly downstream of the wake generator. The cavity size behind the wake shows a similar trend though with larger variation in radius. In general, the mean was larger as the result of the increased vortex strength behind the wake. The results based on Proctor's model gave a reasonable match with the cavity size for uniform inflow.

2.4.3. SOUND DUE TO TIP-VORTEX CAVITATION

In the preliminary stages of this study the parameter space of the cavitation tunnel was explored. The first criterion that had to be met was to arrive at a moderate propeller Reynolds number. Full-scale propellers operate at significantly higher Reynolds numbers. To limit the scale effects of a large chordwise laminar boundary-layer, the maximum propeller diameter and revolution rate were used. This resulted in a requirement on the minimum advance ratio due to the maximum motor torque. The second criterion was a sufficient production of cavitation sound. Only for the minimum advance ratio was sufficiently large range of cavitation numbers achievable for studying cavitation-related sound. The tunnel pressure could only be reduced, and not increased, relative to atmospheric pressure. Therefore, at the chosen condition a stationary tip-vortex cavity was always present even at the highest cavitation number. This prevented a comparison

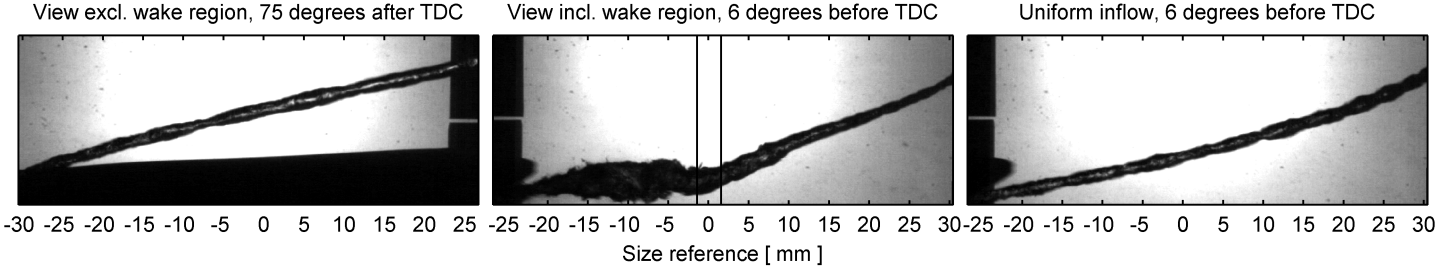

Figure 2.10: Typical high-speed video images at indicated blade tip positions with respect to top dead center (TDC). In contrast to the sketch in Fig. 2.5, in the left image the camera was positioned on the opposite side of the propeller shaft from where the wake plates were placed. Flow is from bottom to top and blade rotation is from right to left. In all images the hubcap could be identified as the black rectangle separated from the propeller by a small gap. The two vertical lines in the middle image indicate the range of cavity diameter recording behind the wake generator. In the other two views the tip vortex cavity was captured in the whole field of view. The location at 0 mm corresponds to 30 degrees from TDC. Conditions: $J = 0.56$, $K_T = 0.18$, $10K_Q = 0.27$, $Re = 6.6 \times 10^5$, $\sigma_n = 5.5$ and $DO = 2.3\ mg/l$.

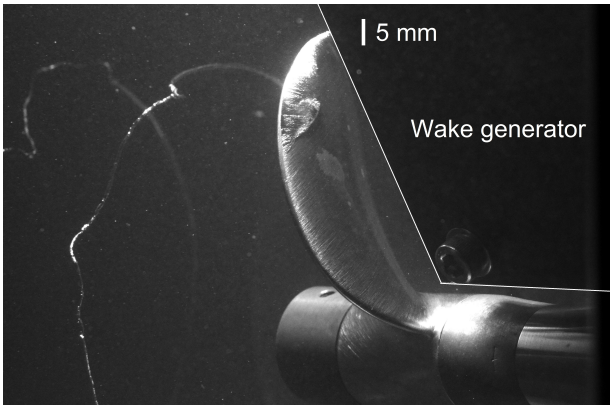

(a)

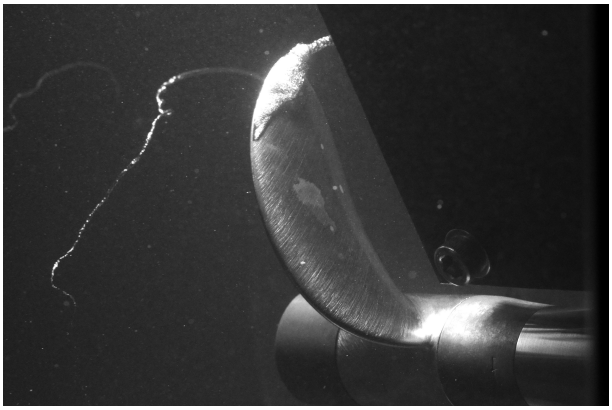

(b)

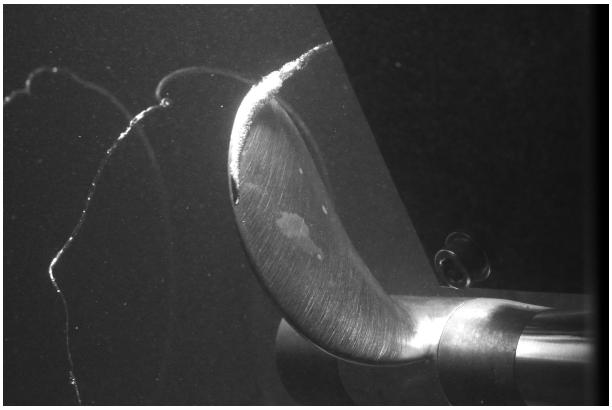

(c)

Figure 2.11: Images of cavitation on the propeller as it passes the wake of the wake generator. The black object in the top right corner is the wake generator (outlined in (a)). Each image is of a separate revolution. Rotation angle intervals are spaced by 10 degrees. Angular position of the propeller blade in Fig. 2.10 was based on the projection of the tip geometry. This was compared to a CAD projection at a known angle. For these images this procedure is not possible. Conditions: $J = 0.56$, $K_T = 0.18$, $10K_Q = 0.28$, $Re = 6.6 \times 10^5$, $\sigma_n = 5.5$ and $DO = 2.3\ mg/l$.

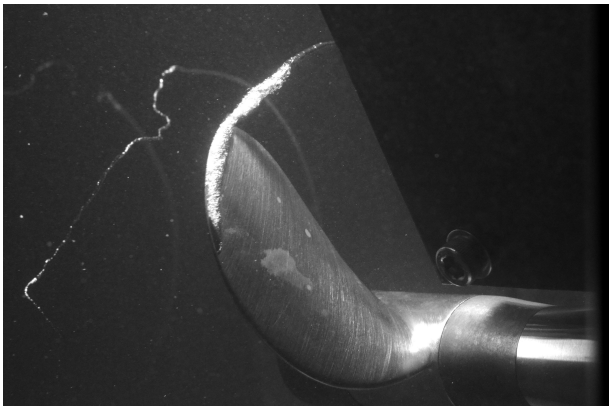

(d)

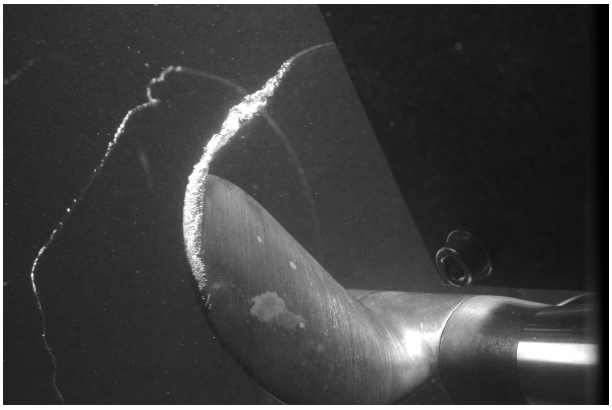

(e)

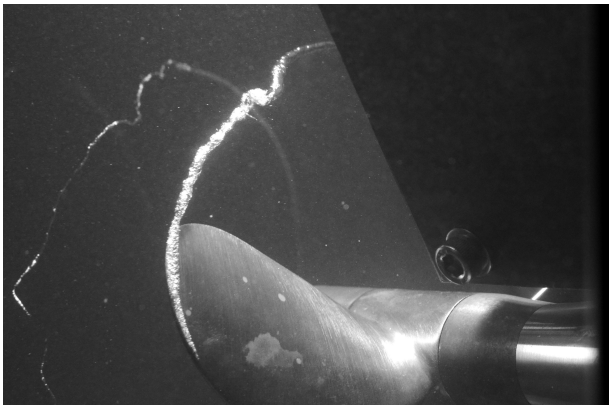

(f)

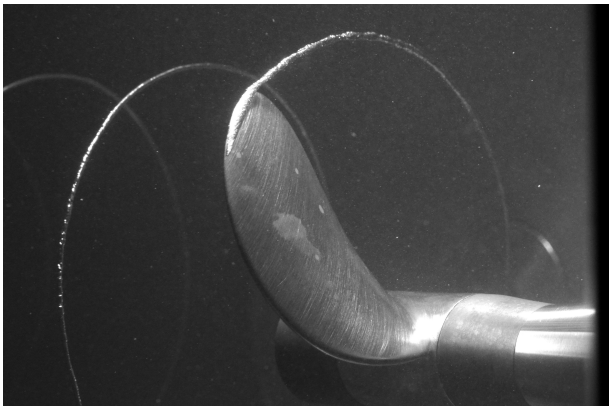

Figure 2.12: Image of cavitation on the propeller in uniform inflow. Conditions: $J = 0.56$, $K_T = 0.18$, $10K_Q = 0.27$, $Re = 6.6 \times 10^5$, $\sigma_n = 5.5$ and $DO = 2.3\ mg/l$.

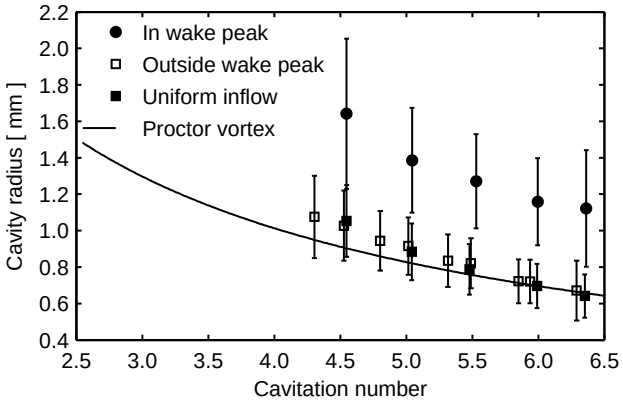

Figure 2.13: Cavity radius as function of cavitation number. Spatial and temporal mean obtained between $0.1c$ and $1.8c$ along the vortex axis downstream of the propeller tip. Values in wake peak are obtained between the vertical lines in Fig. 2.10. Conditions: $J = 0.56$, $K_T = 0.18$, $10K_Q = 0.27$, $Re = 6.5 \times 10^5$, and $DO = 2.3\ mg/l$. Proctor vortex model parameters: $\Gamma = 0.1287\ m^2/s$, $\beta = 13.9$ and $B = \frac{1}{2}D = 75\ mm$. The Proctor vortex model is not fit to the cavity radius. It is the result of a β parameter fit with the dominant sound frequencies in Fig. 2.19.

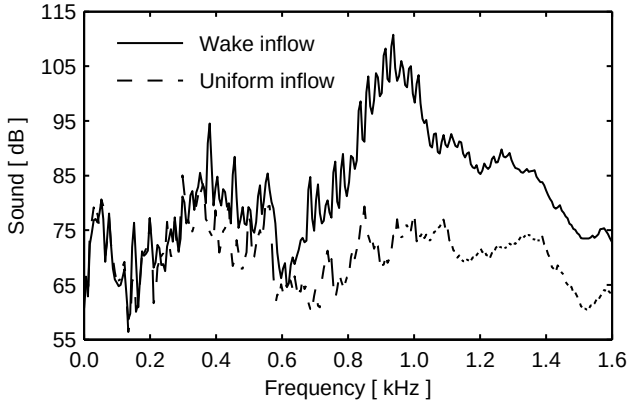

Figure 2.14: Comparison power density spectrum for wake inflow and for uniform inflow, with reference value of 10^{-12} Pa^2/Hz. The blade passage frequency is 76 Hz. Spectra belong to the cases of Fig. 2.10. Conditions: rotation rate 38 Hz, $J = 0.56$, $K_T = 0.18$, $10K_Q = 0.27$, $Re = 6.6 \times 10^5$, $\sigma_n = 5.5$ and $DO = 2.5$ mg/l.

to a sound spectrum of fully wetted flow.

For conditions with steady tip-vortex cavitation there was no significant sound production above the background noise of the tunnel. To study tip vortex cavitation related sound a strong excitation was necessary. This was realised by a non-uniform inflow into the propeller, caused by an upstream generator with a narrow wake. Various configurations of upstream wake plates were tested, including configurations with a different number of plates, different spacings between the plates and different distances to the propeller. This study was not performed as a documented parametric approach, but by casual observation, until significant sound was produced. The final configuration is the one that is described in Fig. 2.5.

The variation in inflow velocity due to the wake generator, resulted in a large and rapid variation of the loading on the propeller blade, while passing the wake of the wake generator. As seen in Fig. 2.10, once the tip vortex has passed through the wake the tip-vortex cavity grows fast. This interaction between the wake and tip vortex cavity produces a high amplitude sound. A comparison of sound production was presented in Fig. 2.14 for steady tip-vortex cavitation in a uniform flow and wake-excited tip-vortex cavitation.

There was a 30 dB broadband increase in sound level between 0.8 and 1.1 kHz that corresponds to the 10th and 14th blade passage frequency, respectively. The blade passage frequency is the propeller rotation rate multiplied with the number of blades. It was clearly audible by an observer next to the test section. The dominant frequency of this sound decreased when the tunnel pressure was reduced. Reducing the tunnel pressure results in a decrease of the cavitation number and therewith in a larger tip-vortex cavity. Once every revolution at a fixed blade angle an index pulse was recorded. This provides the opportunity to study the evolution of the amplitude of the sound as a function of blade angle. The result is given in Fig. 2.15.

The horizontal lines contain the sound amplitude as function of blade angle (time)

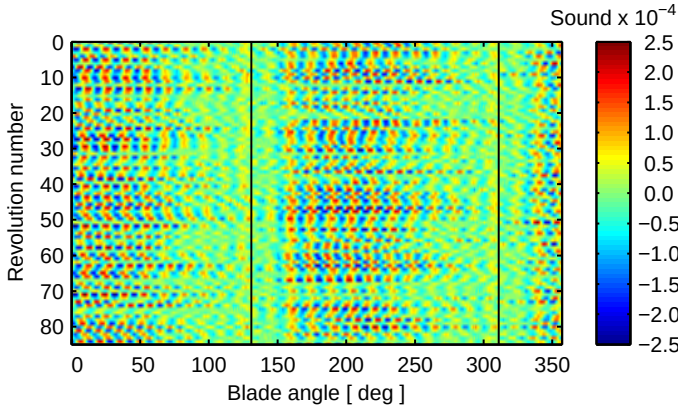

Figure 2.15: Sound pressure amplitude $K_P = p/(\rho n^2 D^2)$ in wake inflow, presented as rows of complete blade revolutions. The vertical black lines are top dead center of the two blade tips. Conditions: $J = 0.56$, $K_T = 0.18$, $10K_Q = 0.27$, $Re = 6.6 \times 10^5$, $\sigma_n = 5.5$ and $DO = 2.6\ mg/l$.

for several individual blade revolutions. Two vertical reference lines denote the location of TDC of the two blade tips. At this location the blade has passed the wake, which was at 30 degrees before TDC. The dominant source of sound manifests itself when the blade was well past the wake peak. It was also present during a significant portion of the blade revolution. For comparison, the sound amplitude for steady tip-vortex cavitation in uniform inflow is presented in Fig. 2.16.

The dominant frequency could be directly related to the frequency of the highest amplitude of 925 Hz in Fig. 2.14. Figure 2.15 is also a very clear demonstration of all the elements described by Bosschers (2009), that contribute to a broadband sound. Amplitude and phase modulation of a tonal signal results in a smearing-out of the spectral content in the frequency domain.

The dominant sound was not related to cavity growth or implosion close to the propeller tip. These are often found at a frequency an order of magnitude lower, i.e. around the blade passage frequency of 76 Hz. To rule out the potential sound production of the wake generator, a similar result as in Fig. 2.15 is given in Fig. 2.17 for a wake generated by a smaller number of plates at a higher advance ratio of the propeller.

The lighter loading of the propeller blade, and the smaller excitation due to the wake, resulted in a very intermittent behavior. There was a clear difference between the two blades. One produces significantly more sound than the other. Between revolution number 50 and 60 the sound amplitude was low for both blades. In the high-speed video these revolutions showed that there is no sign of tip-vortex cavitation. The excitation of the tip vortex cavity sometimes resulted in breaking up of the vapor volume. If in the next blade passage cavitation inception did not take place, there was no tip vortex cavity to be excited by the wake. This also shows that there is no significant sound produced by the interaction of the propeller with the wake without cavitation.

The sound source was found from a comparison of the dominant frequency of the sound with the visual observations of the tip-vortex cavity-oscillations with high-speed

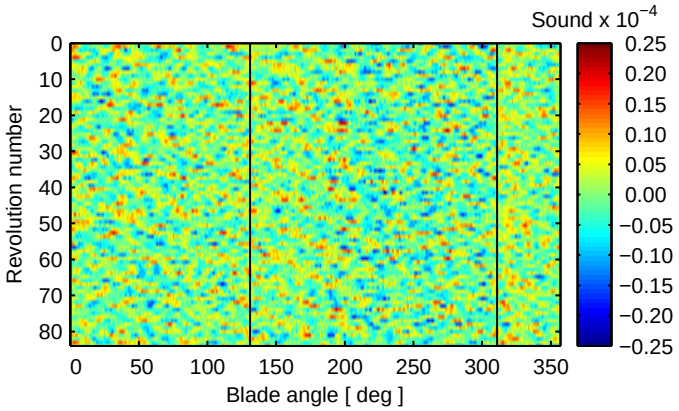

Figure 2.16: Sound pressure amplitude $K_P = p/(\rho n^2 D^2)$ in uniform inflow, presented as rows of complete blade revolutions. The vertical black lines are top dead center of the two blade tips. Note that the pressure amplitude range is an order of magnitude smaller than in Fig. 2.15. Conditions: $J = 0.56$, $K_T = 0.17$, $10K_Q = 0.27$, $Re = 6.6 \times 10^5$, $\sigma_n = 5.5$ and $DO = 2.4\ mg/l$.

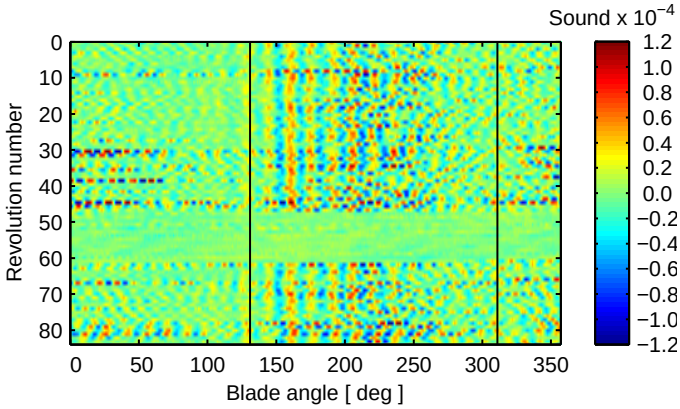

Figure 2.17: Sound pressure amplitude $K_P = p/(\rho n^2 D^2)$ in wake inflow, presented as rows of complete blade revolutions. The vertical black lines are top dead center of the two blade tips. Conditions: $J = 0.70$, $K_T = 0.14$, $10K_Q = 0.23$, $Re = 6.7 \times 10^5$, $\sigma_n = 4.0$ and $DO = 3.3\ mg/l$. Here the wake inflow is generated by 3 plates with the same spacing as with the wake generator used for Fig. 2.15, resulting in a narrower wake.

video. These oscillations are then related to the results of the model for the tip-vortex cavity-resonance frequency described in section 2.2. First, the time trace of the sound of each individual blade is analysed separately. It is assumed that under the influence of the upstream wake, the blade downstream of the wake is dominant in the measured sound. The sound amplitude produced by the steady tip-vortex cavity on the other blade is an order of magnitude lower (see Fig. 2.15 and Fig. 2.16). As the main focus was the dominant frequency, there was no need for a detailed spectrum. A very robust estimation of the dominant frequency component was obtained by using an autocorrelation of the individual sound time traces. The result was an autocorrelation function that had the highest negative correlation peak at a shift of half the dominant period. A cosine was fit through this half period to obtain the dominant sound frequency.

A similar approach was applied to the high-speed video results of the oscillation of the tip-vortex cavity-diameter following the passage of the tip vortex through the wake. In contrast to the larger number of periods available in the sound signal, the excited oscillations of the diameter were only available for four periods. The estimation of the dominant frequency was therefore less accurate. An example of this procedure is presented in Fig. 2.18. It was only applied for cavitation numbers for which the cavity did not experience break-up during the wake excitation. Both results are presented in Fig. 2.19.

The trend of the dominant sound frequency with cavitation number was also observed from the audible sound during experiments. For decreasing cavitation number the tip-vortex cavity size increases, decreasing the dominant sound frequency. At a cavitation number of 3 the signal variability increases. This was an indication that there was no longer a clear dominant component present in the sound. The cavitation pattern for $\sigma_n = 3$ is dominated by large scale shedding from the leading edge sheet on the propeller blade. There is no consistent cavity volume that can hold a resonance frequency. The frequencies found from the high-speed video observations of the oscillations of the tip-vortex cavity show the same trend as the dominant sound frequencies. The larger variability overlaps with the sound frequencies, but in general the mean was lower.

The results indicate the tip vortex cavity as the source of the dominant component in the sound. However, observations were limited in spatial extent because of the available field of view. The slightly lower mean frequency indicated that it was more likely that a part of the tip vortex cavity with smaller mean diameter was responsible for the sound production at its resonance frequency. The wake excitation was transmitted downstream to the part of the tip vortex cavity that was no longer directly affected by the wake. This was in line with the results of Fig. 2.15, showing that the tonal signal persists for more than 100 degrees, while the cavity in the wake peak is broken up.

In Fig. 2.19, the solid line represents the computed tip-vortex cavity-resonance frequency based on Proctor's vortex model. The β parameter in this model was the only unknown. This value was obtained by a least squares fit of the dominant sound frequencies. Considering the value of the radial-mean circulation Γ, the result of $\beta = 14$ was very much in line with the findings of Pennings *et al.* (2015*b*), who found values of 13 - 18 for a stationary wing with similar loading and a similar streamwise location of the tip vortex cavity.

The cavity radius used for the computation of the cavity resonance frequency was also based on Proctor's vortex model. The β value is the result of a fit of Proctor's vor-

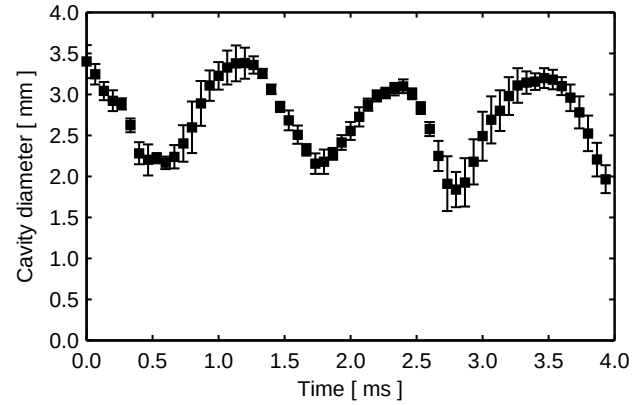

(a)

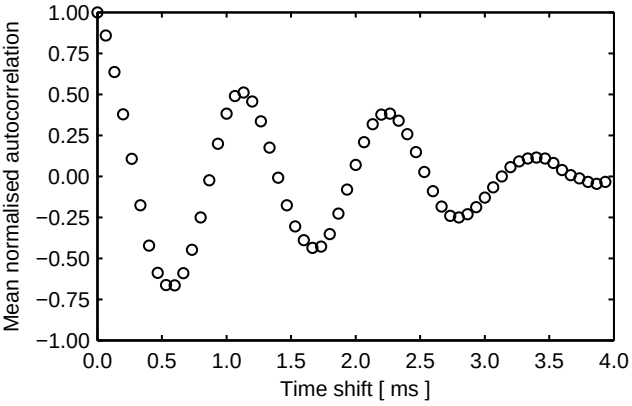

(b)

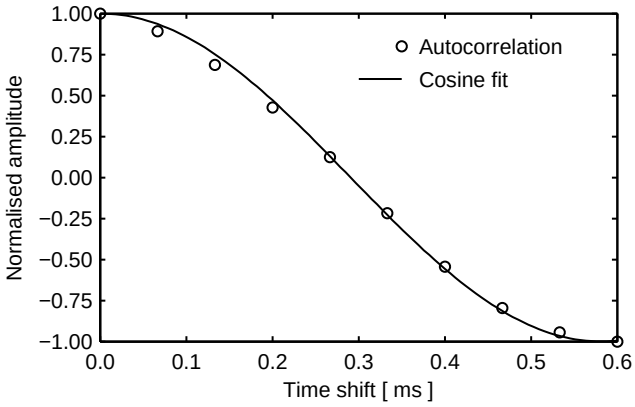

(c)

Figure 2.18: Approach for obtaining the dominant frequency of oscillations of the cavity diameter. This is an example with a very good signal to noise ratio that was typically lower. Average over forty columns of diameter variation in time (a)(columns between vertical lines in Fig. 2.10, bars represent the variation in space), normalised average autocorrelation (b)(based on diameter oscillation in individual columns) and cosine fit to the first half period of the autocorrelation (c). Conditions: $J = 0.56$, $K_T = 0.18$, $10K_Q = 0.27$, $Re = 6.6 \times 10^5$, $\sigma_n = 5.5$ and $DO = 2.4\ mg/l$.

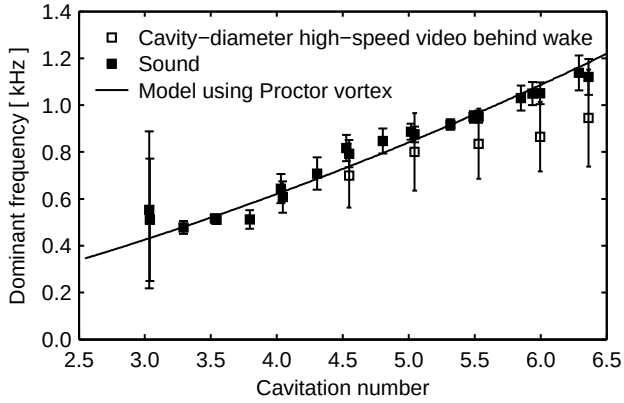

Figure 2.19: Dominant frequency of sound and high-speed video of tip-vortex cavity-diameter oscillations as function of cavitation number. Conditions: rotation rate 38 Hz, $J = 0.56$, $K_T = 0.18$, $10K_Q = 0.28$, $Re = 6.5 \times 10^5$ and $DO = 2.2\ mg/l$. Proctor's vortex model parameters: $\Gamma = 0.1287\ m^2/s$, $\beta = 13.9$ and $B = \frac{1}{2}D = 75\ mm$.

tex model to the dominant sound frequency in Fig. 2.19. Although the cavity radii were directly measured they were not used in Fig. 2.19. The result of the fit using Proctor's model in terms of cavity radius can be compared to the measured cavity radii in Fig. 2.13. This shows that the representative cavity size that results in the correct dominant sound frequency is the cavity size in uniform inflow. A similar result was found by Bosschers (2009). He found a correlation between the dominant sound frequencies and the minimum radius of the tip vortex cavity during oscillation.

2.5. DISCUSSION

This study has analysed the mechanisms behind the emission of broadband pressure fluctuations by the cavitating tip vortex from a propeller. The majority of full-scale propellers have 4 or 5 blades. The frequency range in which broadband pressure fluctuations are found is between the fourth and seventh blade passage frequency (van Wijngaarden *et al.*, 2005). A propeller with two blades is used in the present study in order to minimise the interaction between the tip vortices from subsequent blades. The frequency range of broadband pressure fluctuations is found between the 10th and 14th blade passage frequency. If the number of blades is accounted for in the comparison the frequency range is the same. When considering the tip-vortex cavity-resonance frequency as the physical mechanism for sound production, it follows that there is not a direct relation with the blade passage frequency. The specific combination of blade loading and cavity size, on full-scale propellers, only indirectly results in this common frequency range for broadband sound.

The wake field used was not a realistic representation of the flow field behind a ship hull. The wake generator was used here to serve the purpose of exciting the tip vortex cavity with disturbances of sufficient amplitude over a broad frequency range. Although not representative for the wake of a ships, it is considered to be a good conceptual repre-

sentation of the problem of broadband hull-pressure fluctuations as occur on ships. In the present setup, it was possible to separate the two stages of excitation. The increase in loading by the upstream wake generates an enlarged cavity close to the tip. The implosion of this cavity is the phenomenon that provides energy for the resonance of the tip-vortex cavity. The match between the time scale of cavity implosion, and the resonance frequency of the tip-vortex cavity right after passage through the wake, could determine the energy transfer and the resulting time the dominant sound persists. The dynamics of the tip/leading edge sheet did not dominate the sound spectrum and the tip vortex cavity can be studied in detail by high-speed video. The link between observations of cavitation and sound measurements is essential in the effort to understand the mechanisms of sound sources.

No general model for the local strength of the tip vortex and the resulting cavity size exists for any propeller in an arbitrary wake field. The Proctor vortex model for a vortex without cavitation was used successfully in this study as a first approximation. As validation data was not available, only the consistency of this empirical vortex model was confirmed. The maximum blade circulation was also evaluated as an alternative for the radial-mean blade circulation. The result in terms of fit quality to the dominant sound frequencies and cavity size was the same, for a lower value of β.

It would be useful to obtain a better model for the flow field of a tip vortex without cavitation. This could then be used as input for the detailed description of the broadband pressure fluctuations, which also has to include the amplitude and bandwidth (this is addressed by Johan Bosschers at MARIN (Bosschers, 2009)).

2.6. CONCLUSION

Good agreement was found of the measured propeller forces with the results from the boundary element method Procal. Therefore, the computed radial-mean of the distribution of blade circulation was taken as a representative value for the tip vortex circulation (Pennings *et al.*, 2015*b*).

The cavity radius as function of the cavitation number at the tip was obtained with high-speed video shadowgraphy. The part of the vortex cavity outside the wake of the wake generator had the same size as the vortex cavity in a corresponding uniform inflow. The section of the tip vortex cavity that passed through the wake was significantly larger. The Proctor vortex model, using the radial-mean of the distribution of the blade circulation, $\beta = 14$ and a wing span equal to $\frac{1}{2}D$, gave a good description of the tip-vortex cavity-size in uniform inflow.

A stationary tip vortex cavity in a uniform inflow, did not produce significant amplitude of sound. The addition of a wake generator upstream of the propeller resulted in sound in a broad band, up to 30 dB above the sound in a uniform inflow. The sound source was strongest when the propeller blade tip was at least 60 degrees past the wake generator (Fig. 2.15). This corresponds to a blade angle for which the cavity collapses and rebounds close to the blade are completed. Dependent on the cavitation number, the source of sound could persist for 100 degrees of blade rotation.

The dominant frequency obtained from the measured sound correlated strongly with that of the oscillations of the cavity diameter. The size of the tip-vortex cavity in uniform inflow or the cavity size in the region not passing through the wake of the wake generator

was related to the dominant sound source. The location of this source was expected to lie downstream of the field of view behind the wake.

The Proctor model, through the β parameter, was fitted to the dominant sound frequencies. After fitting, the resulting trend of frequency versus cavitation number agrees very well. The vortex properties used, correspond to those of a tip-vortex cavity in uniform inflow. The value that was obtained from the fit ($\beta = 14$) was in line with those found by Pennings *et al.* (2015*b*).

REFERENCES

ASTOLFI, J.-A., BILLARD, J.-Y., DORANGE, P. & FRUMAN, D.H. 1998 Pressure Fluctuations Associated with Tip Vortex and Surface Cavitation. In *Proceedings of the ASME Fluids Engineering Division Summer Meeting*. Washington D.C., USA.

BARKER, STEVEN J. 1976 Measurements of Hydrodynamic Noise from Submerged Hydrofoils. *Journal of the Acoustical Society of America* **59** (5), 1095–1103.

BOSSCHERS, JOHAN 2008 Analysis of Inertial Waves on Inviscid Cavitating Vortices in Relation to Low-Frequency Radiated Noise. In *Proceedings of the Warwick Innovative Manufacturing Research Centre (WIMRC) Cavitation: Turbo-machinery and Medical Applications Forum*. Warwick University, United Kingdom.

BOSSCHERS, JOHAN 2009 Investigation of Hull Pressure Fluctuations Generated by Cavitating Vortices. In *Proceedings of the First Symposium on Marine Propulsors*. Trondheim, Norway.

BOSSCHERS, J., VAZ, G., A.R. & VAN WIJNGAARDEN, E. 2008 Computational Analysis of Propeller Sheet Cavitation and Propeller-Ship Interaction. In *Proceedings of the RINA conference MARINE CFD2008*. Southampton, UK.

BRIANÇON-MARJOLLET, L. & MERLE, L. 1997 Inception, Development and Noise of a Tip Vortex Cavitation. In *Proceedings of the Twenty-First Symposium on Naval Hydrodynamics*.

BRUBAKK, E. & SMOGELI, H. 1988 QE2 from Turbine to Diesel - Consequences for Noise and Vibration. In *Proceedings of the International Marine and Shipping Conference*.

CANNY, JOHN 1986 A Computational Approach to Edge Detection. *IEEE Transactions on Pattern Analysis and Machine Intelligence* **PAMI-8** (6), 679–698.

FOETH, EVERT-JAN 2008 The Structure of Three-Dimensional Sheet Cavitation. PhD thesis, Delft University of Technology, Delft, The Netherlands.

HIGUCHI, H., ARNDT, R.E.A. & ROGERS, M.F. 1989 Characteristics of Tip Vortex Cavitation Noise. *Journal of Fluids Engineering* **111**, 495–501.

MAINES, B. & ARNDT, R.E.A. 1997 The Case of the Singing Vortex. *Journal of Fluids Engineering* **119**, 271–276.

PENNINGS, P.C., BOSSCHERS, J., WESTERWEEL, J. & VAN TERWISGA, T.J.C. 2015*a* Dynamics of isolated vortex cavitation. *Journal of Fluid Mechanics* **778**, 288–313.

PENNINGS, P.C., WESTERWEEL, J. & VAN TERWISGA, T.J.C. 2015*b* Flow field measurement around vortex cavitation. *Experiments in Fluids* **56**.

PENNINGS, P.C., WESTERWEEL, J. & VAN TERWISGA, T.J.C. 2016 Cavitation tunnel analysis of radiated sound from the resonance of a propeller tip vortex cavity. *International Journal of Multiphase Flow* (accepted, in press).

RÆSTAD, ARNT EGIL 1996 Tip Vortex Index - An Engineering Approach to Propeller Noise Prediction. *The Naval Architect* pp. 11–14.

VAN TERWISGA, TOM, VAN WIJNGAARDEN, ERIK, BOSSCHERS, JOHAN & KUIPER, GERT 2007 Achievements and Challenges in Cavitation Research on Ship Propellers. *International Shipbuiling Progress* **54**, 165–187.

VAN WIJNGAARDEN, ERIK, BOSSCHERS, JOHAN & KUIPER, GERT 2005 Aspects of the Cavitating Propeller Tip Vortex as a Source of Inboard Noise and Vibration. In *Proceedings of the ASME Fluids Engineering Division Summer Meeting and Exhibition*. Houston, Texas, USA.

VAZ, G. 2005 Modelling of Sheet Cavitation on Hydrofoils and Marine Propellers using Boundary Element Methods. PhD thesis, University of Lisbon, IST, Lisbon, Portugal.

WU, J.-Z., MA, H.-Y. & ZHOU, M.-D. 2006 *Vorticity and Vortex Dynamics*. Springer.

ZVERKHOVSKYI, OLEKSANDR 2014 Ship Drag Reduction by Air Cavities. PhD thesis, Delft University of Technology, Delft, The Netherlands.

3

DYNAMICS OF ISOLATED VORTEX CAVITATION

The dynamic behaviour of vortex cavitation on marine propellers may cause onboard noise and vibration, but is not well understood. The main goal of the present study is to experimentally analyse the dynamics of an isolated tip vortex cavity generated at the tip of a wing of elliptical planform. Detailed high-speed video shadowgraphy was used to determine the cavity deformations in combination with force and sound measurements. The cavity deformations can be divided in different modes, each of which show a distinct dispersion relation between frequency and wave number. The dispersion relations show good agreement with an analytical formulation. Finally, experimental support is given to the hypothesis that the resonance frequency of the variation of the cavity volume is related to a zero group velocity.

This chapter has been published in Journal of Fluid Mechanics **778**, *pp.* 288-313, Pennings *et al.* (2015). Section 3.2, on the theoretical dispersion relation of waves on a vortex cavity, was written by Johan Bosschers.

3.1. INTRODUCTION

Tip vortex cavitation is among the first forms of cavitation to appear on ship propellers. It is an important design consideration for ships that require low noise and vibration levels. The vortex strength and thus the cavity thickness can be reduced by unloading the blade tip at the cost of reduced propeller efficiency. Vortex cavitation may cause broadband hull-pressure fluctuations that can lead to onboard noise and vibrations.

The broadband character can be explained by the variability of the hull pressure fluctuations between blade passages. The centre frequency of the so-called broadband hump is expected to be due to a tip vortex cavity resonance (Ræstad, 1996; Bosschers, 2007), but this resonance behaviour is not understood. An example of a wing with a tip vortex cavity is shown in figure 3.6. As early as 1880 a theoretical dispersion relation was derived by Thomson (1880) that describes the dynamics of waves travelling on an isolated tip vortex cavity. This was extended to include the effects of compressibility and surface tension by Morozov (1974). A modification to the theory was proposed by Bosschers (2008, 2009) to account for a free-stream axial-velocity and as well as viscous effects. As the model for waves on a vortex cavity is neutrally stable, there is no obvious criterion at which frequency resonance can be expected.

Experiments involving sound measurements of cavitating tip vortices of wings have shown distinct tonal frequencies (Higuchi *et al.*, 1989; Astolfi *et al.*, 1998). Briançon-Marjollet & Merle (1997) measured the velocity distribution, the cavity diameter and sound of a tip vortex cavity trailing from a wing. A correlation of the sound measurements was made to the frequency of the vortex centreline displacement mode and the elliptic deformation mode in the limit of small wave numbers as given by Morozov (1974). However, as no high-speed video recordings were available at that time, the sound could not directly be related to the deformations of the vortex cavity.

The most detailed study to date is by Maines & Arndt (1997) who used high-speed video recordings to investigate the relation between deformations of a tip vortex cavity and a distinct frequency component in the measured sound spectrum. The resonance frequencies obtained from sound measurements were related to a criterion with zero phase velocity but the high-speed video data for this study was also not sufficient to validate the analytic model used to explain the resonance frequency of the tip-vortex cavity. An alternative explanation was provided by Bosschers (2009) who related the experimental data to the criterion of zero group velocity of the mode involving cavity volume variations. A group-speed criterion was used by Keller & Escudier (1980) to explain the occurrence and wave lengths of standing waves on a cavitating vortex in a vortex tube.

This shows that there is a disagreement in the deformation mode which is thought to be responsible for the vortex cavity resonance. The underlying theoretical dispersion relation which is used to describe this criterion varies slightly between authors but has never been validated. The main goal of the present study is to provide an understanding of the dynamics of waves on a tip vortex cavity by computing a frequency - wave number diagram for different cavity deformation modes using detailed high-speed video recordings. In this diagram distinct features can be distinguished with varying phase velocity and group velocity. Most of these features can be related to the theoretical dispersion relation.

The high-speed video observations are made of a tip vortex cavity generated by a

stationary wing of elliptical planform placed in the Delft cavitation tunnel. To also be able to study the criterion of cavity resonance, tests are performed on a wing similar in geometry to the one used by Maines & Arndt (1997).

In the next section the analytical model for vortex cavity deformations is described. Then, the details of the experimental setup are given. The results are discussed to gain an understanding of the dynamics of the vortex cavity. Based on the results the validity of the analytical model is assessed and used to define the criterion for a cavity resonance frequency. Finally the differences in findings compared to the previous studies (Higuchi *et al.*, 1989; Maines & Arndt, 1997; Astolfi *et al.*, 1998) are discussed.

3.2. THEORETICAL DISPERSION RELATION

The starting point for the derivation of the dispersion relation is the convected Helmholtz equation for a disturbance velocity potential $\tilde{\varphi}$ (Howe, 2003):

$$\nabla^2\tilde{\varphi} - \frac{1}{c^2}\left(\frac{\partial}{\partial t} + \mathbf{U}\cdot\nabla\right)^2\tilde{\varphi} = 0, \tag{3.1}$$

in which c corresponds to the speed of sound and $\mathbf{U}$ to the free stream velocity vector. The free stream flow needs to be irrotational with a velocity magnitude much smaller than the speed of sound. A cylindrical coordinate system (r,θ,x) will be adopted with a harmonic variation of the disturbance potential given by:

$$\tilde{\varphi}(r,\theta,x,t) = \phi(r)\, e^{i(k_x x + n\theta - \omega t)}, \tag{3.2}$$

in which $\phi(r)$ corresponds to a potential that is only a function of radius, k_x corresponds to the axial wave number, n is the azimuthal wave number (which must be an integer) and ω the angular frequency. Using only the axial free stream velocity component W in $\mathbf{U}$ leads to the equation for $\phi(r)$

$$\phi'' + \frac{\phi'}{r} + \left[-k_x^2 - \frac{n^2}{r^2} + \frac{1}{c^2}(\omega - W k_x)^2\right]\phi = 0, \tag{3.3}$$

where a prime denotes the derivative with respect to the radius. When introducing the projected acoustic wave number in the radial direction k_r defined as

$$k_r^2 = \frac{1}{c^2}(\omega - W k_x)^2 - k_x^2 \quad , \tag{3.4}$$

and considering that the vortex is radiating sound away from the core of the vortex, the solution for the disturbance potential is given by the Hankel function of the first kind:

$$\tilde{\varphi}(r,\theta,x,t) = \hat{\phi}\, H_n^1(k_r r)\, e^{i(k_x x + n\theta - \omega t)}, \tag{3.5}$$

in which $\hat{\phi}$ is the amplitude of the disturbance potential.

The velocity components in $\mathbf{U}$ should include both the axial free stream velocity W and the azimuthal velocity due to the vortex, but the addition of an azimuthal velocity leads to a Matthieu equation for which no analytical solution is available. For low frequencies and the typical vortex strengths considered here, the additional terms are small for modes $n = 1$ and $n = 2$ as the velocity is divided by the speed of sound and are

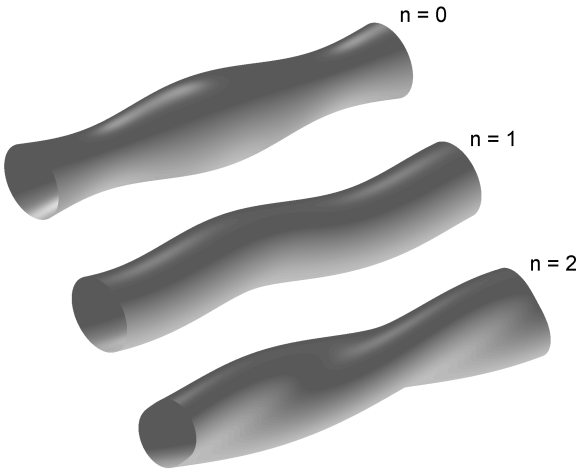

Figure 3.1: Modes of main vortex cavity oscillation reproduced from Bosschers (2008). With on top the monopole breathing $n = 0$ mode, in the middle the dipole serpentine $n = 1$ centreline displacement mode and at the bottom the quadrupole helical $n = 2$ mode.

here neglected. For the mode $n = 0$ no additional terms arise. The introduction of the azimuthal velocity then gives an equation identical to (3.3).

The distortion of the cavitating vortex with average radius r_c is described by a number of modes characterised by k_x, n, ω and amplitude $\hat{r}$. For small amplitudes, the local cavity radius η is given by

$$\eta = r_c + \tilde{r} = r_c + \hat{r}\mathrm{e}^{i(k_x x + n\theta - \omega t)}. \tag{3.6}$$

The mode $n = 0$ corresponds to a breathing mode and involves volume variations. Mode $n = 1$ corresponds to a serpentine mode, also called bending mode, helical mode or displacement mode, as it is the only mode that leads to a displacement of the vortex centreline. The mode $n = 2$ is the bell mode or double helix or fluted mode, and leads to an elliptical shape of the cross section of the vortex core. A visualisation of the modes is presented in figure 3.1. The distortions are transversely propagating inertial waves and are often referred to as Kelvin waves (Saffman, 1995).

In reality these modes are superposed on the vapour-liquid interface of tip vortex cavitation. It was very challenging to identify these modes in the time and space based on high-speed video images. Alternatively they can be identified based on their individual dispersion relations, that are distinctly different in frequency and wave number. It was the eventual goal to identify mode $n = 0$ in an experiment to show that this monopole can be responsible for high amplitude sound production.

The equations to find the dispersion relation are obtained by using a small perturbation analysis for the kinematic and dynamic boundary conditions. The small perturbation in cavity radius with amplitude $\tilde{r}$ will result in a perturbation velocity given by the spatial derivative of the potential $\tilde{\varphi}(x, r, \theta, t)$. The derivations by Thomson (1880) and Morozov (1974) use a formulation for the azimuthal velocity V valid for potential flow,

but it is shown here that, at least for $n = 0$, the dispersion relation can also be derived for an azimuthal velocity distribution representing a viscous vortex. In both formulations a zero mean radial velocity U and a constant mean axial velocity component W are used. The mean velocities for potential flow in which a vortex with circulation Γ is present are then given by

$$\mathbf{U} = (U, V, W) = \left(0, \frac{\Gamma}{2\pi r}, W\right). \tag{3.7}$$

For viscous flow, the situation is more complicated. Neglecting the flow inside the cavity, the azimuthal velocity in a viscous fluid has to satisfy a zero shear stress boundary condition at the cavity interface which leads to a different behaviour of the velocity in the liquid near the cavity interface, when compared to the non-cavitating vortex as shown in Bosschers (2015). However, this change in velocity leads to a small change only in pressure at the cavity radius from which it is concluded that a formulation for the azimuthal velocity of a non-cavitating vortex can also be used to find the relation between cavity size and pressure. The Burnham-Hallock model (Burnham & Hallock, 1982) is used here due its simple formulation for the pressure variation. The azimuthal velocity at radius r for a non-cavitating vortex with viscous core radius r_v is given by

$$V(r) = \frac{\Gamma}{2\pi} \frac{r}{r_v^2 + r^2}. \tag{3.8}$$

The kinematic boundary condition for $f = r - \eta$ is given by

$$\frac{Df}{Dt} = \frac{\partial f}{\partial t} + \left(\mathbf{U} + \nabla\tilde{\varphi}\right) \cdot \nabla f = 0. \tag{3.9}$$

Only the linear terms of the perturbations in potential and cavity radius will be retained, which implies that the equation contains only the perturbation velocity in the radial direction and the derivative of the η perturbation in time, axial direction and azimuthal direction:

$$\hat{\phi}\, k_r H_n^{1'}(k_r r_c) - \left(-i\omega + W i k_x + V_c \frac{in}{r_c}\right) \hat{r} = 0, \tag{3.10}$$

where the prime again denotes the derivative with respect to r and V_c is the mean azimuthal velocity at the cavity interface $r = r_c$.

The dynamic boundary condition states that the pressure at the cavity interface has to be equal to the vapour pressure. For potential flow, the Bernoulli equation can be used, as in Thomson (1880) and Morozov (1974). Here, the start is made from the radial momentum equation to investigate if a viscous vortex solution can be applied. The radial component of the momentum equation is given by

$$-\frac{1}{\rho}\frac{\partial p}{\partial r} = \frac{\partial}{\partial t}\frac{\partial \tilde{\varphi}}{\partial r} + \left(\mathbf{U} + \nabla\tilde{\varphi}\right).\nabla\frac{\partial \tilde{\varphi}}{\partial r} - \frac{\left(V + \frac{\partial \tilde{\varphi}}{r\partial\theta}\right)^2}{r}. \tag{3.11}$$

If only the linear terms are taken into account, the equation reads:

$$-\frac{1}{\rho}\frac{\partial p}{\partial r} = \frac{\partial}{\partial t}\frac{\partial \tilde{\varphi}}{\partial r} + W\frac{\partial}{\partial x}\frac{\partial \tilde{\varphi}}{\partial r} + V\frac{\partial}{r\partial\theta}\frac{\partial \tilde{\varphi}}{\partial r} - \frac{V^2}{r} - \frac{2V}{r}\frac{\partial \tilde{\varphi}}{r\partial\theta}. \tag{3.12}$$

The first two terms on the right hand side can be integrated directly. The third and fifth terms on the right hand side can only be integrated if a potential flow solution is assumed for V, but these terms vanish for the mode $n = 0$ as the azimuthal disturbance velocity equals zero for this mode. The fourth term can be integrated using either (3.7) or (3.8) for the azimuthal velocity. The integration for this fourth term using (3.8) gives for the pressure in the liquid at the cavity interface $r = \eta$:

$$p_v - p_T + \frac{1}{2}\rho\left(\frac{\Gamma}{2\pi}\right)^2 \frac{1}{\left(r_v^2 + \eta^2\right)} = p_\infty, \tag{3.13}$$

where p_v corresponds to the vapour pressure, p_T to the contribution of surface tension and p_∞ to the free stream pressure in absence of the vortex. Assuming a small amplitude $\tilde{r}$ with respect to r_c, the equation can be written as

$$p_v - p_T + \frac{1}{2}\rho\left(\frac{\Gamma}{2\pi}\right)^2 \frac{1}{\left(r_v^2 + r_c^2\right)} - \rho\left(\frac{\Gamma}{2\pi}\right)^2 \frac{\tilde{r}\, r_c}{\left(r_v^2 + r_c^2\right)^2} = p_\infty. \tag{3.14}$$

The contribution due to surface tension T at $r = \eta$ is given by:

$$\begin{aligned} p_T &= T\left(\tfrac{\partial^2}{\partial x^2} + \tfrac{\partial^2}{\partial r^2} + \tfrac{1}{r}\tfrac{\partial}{\partial r} + \tfrac{1}{r^2}\tfrac{\partial^2}{\partial\theta^2}\right)(r - [r_c + \tilde{r}]) \\ &= T\left(k_x^2 + \tfrac{1}{\eta^2}n^2\right)\tilde{r} + T\tfrac{1}{\eta} \\ &= \tfrac{T}{r_c}\left[1 + \left(n^2 + k_x^2 r_c^2 - 1\right)\tfrac{\tilde{r}}{r_c}\right], \end{aligned} \tag{3.15}$$

where again a linearisation has been applied for the perturbation of the cavity radius. For the situation of zero perturbation, the difference in pressure between the free stream and that at the mean cavity radius due to the mean azimuthal velocity is

$$p_\infty - p_c = \frac{1}{2}\rho\left(\frac{\Gamma}{2\pi}\right)^2 \frac{1}{\left(r_v^2 + r_c^2\right)}, \tag{3.16}$$

with the pressure at the cavity interface given by

$$p_v - \frac{T}{r_c} - p_c = 0. \tag{3.17}$$

The contribution of the term containing $\tilde{r}$ in (3.14), referred to as $\tilde{p}_{c,4}$, with subscript 4 referring to the fourth term in (3.14), can be written as:

$$\tilde{p}_{c,4} = \rho\left(\frac{\Gamma}{2\pi}\right)^2 \frac{\tilde{r}\, r_c}{\left(r_v^2 + r_c^2\right)^2} = \rho V_c^2 \frac{\tilde{r}}{r_c}. \tag{3.18}$$

This relation between $\tilde{p}_{c,4}$ and V_c derived for the Burnham-Hallock vortex model is identical to that for a vortex in potential flow given by (3.7), and it will be assumed in the following that this relation is generally valid and can also be used for formulations for a viscous vortex different from the Burnham-Hallock model.

The sum of all terms in (3.12) containing perturbations to the pressure should be equal to zero, which gives

$$\frac{T}{r_c}\left(n^2+k_x^2r_c^2-1\right)\frac{\tilde{r}}{r_c}-\rho V_c^2\frac{\tilde{r}}{r_c}+i\rho\left(k_xW+\frac{V_cn}{r_c}-\omega\right)\tilde{\varphi}=0. \tag{3.19}$$

Combining the kinematic boundary condition (3.10) and the dynamic boundary condition (3.19) leads to the dispersion relation:

$$\omega_{1,2}=Wk_x+\Omega\left[n\pm\sqrt{\frac{-k_rr_cH_n^{1\,\prime}(k_rr_c)}{H_n^1(k_rr_c)}}\,T_\omega\right], \tag{3.20}$$

in which $\Omega=V_c/r_c$ and T_ω includes the contribution of the surface tension:

$$T_\omega=\sqrt{1+\frac{T}{\rho r_cV_c^2}\left(n^2+k_x^2r_c^2-1\right)}. \tag{3.21}$$

Each vibration mode contains two frequencies corresponding to the plus and minus sign on the right hand side of (3.20). This sign is also used in the following for the identification of the mode. The contribution of the surface tension will not be discussed further as its influence is very small for the case considered. As both frequencies are real numbers the perturbations are neutrally stable. If the axial velocity W is small with respect to the speed of sound, the criterion for a sound wave to occur is that the radial wave number squared, defined by (3.4), is larger than zero. This results in the condition

$$\left|\frac{c_{p,x}}{c}\right|=\left|\frac{k}{k_x}\right|>1, \tag{3.22}$$

where $c_{p,x}=\omega/k_x$ corresponds to the axial phase velocity and k corresponds to the acoustic wave number in the fluid, $k=\omega/c$.

For small axial phase velocities or low frequencies the radial wave number becomes imaginary and the Hankel function reduces to a modified Bessel function of the second kind K. The wave in the radial direction now becomes an evanescent wave as $k_r^2\cong-k_x^2$. The dispersion relation for low frequencies is then given by

$$\omega_{1,2}=Wk_x+\Omega\left[n\pm\sqrt{\frac{-k_xr_cK_n^{1\,\prime}(k_xr_c)}{K_n^1(k_xr_c)}}\right], \tag{3.23}$$

with the non-dimensional form given by

$$\bar{\omega}_{1,2}=\frac{\omega_{1,2}r_c}{W}=\kappa+\frac{V_c}{W}\left[n\pm\sqrt{\frac{-\kappa K_n{}'(\kappa)}{K_n(\kappa)}}\right], \tag{3.24}$$

in which a non-dimensional wave number $\kappa=k_xr_c\cong i\,k_rr_c$ has been introduced. For low frequencies and small axial velocities, the value of the radial wave number becomes approximately equal to the axial wave number. An example of the dispersion relation of (3.20) is given in figure 3.2.

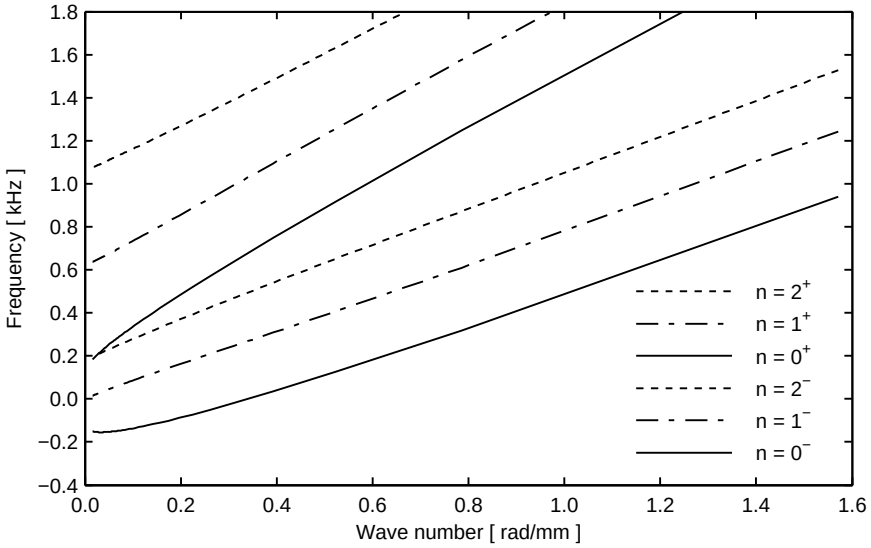

Figure 3.2: Dispersion relation for the two ± branches of the three modes described by (3.20). Condition; $\Omega = 2.0 \times 10^3\ rad/s$, $W = 6.3\ m/s$ and $r_c = 2.3\ mm$.

In the present formulation only outgoing waves are considered while reflections from, for instance, the wall of the test-section of the cavitation tunnel may also be present. The potential at the tunnel walls can be computed from (3.5) while assuming an evanescent wave. A typical value of the smallest relevant wave number on the surface of the the tip vortex cavity from figure 3.2 and as found in the experiment is $k_x = ik_r = 0.04\ rad/mm$. The walls of the tunnel used for the experiment are at a distance $r = 0.15\ m$ from the tip vortex cavity. This results in a value of $k_r r = 6$ which shows that the influence of the tunnel walls on the dispersion relation can be neglected.

The azimuthal velocity at the cavity interface can be derived from the pressure difference. Neglecting surface tension, the formulation for the potential flow vortex gives:

$$\frac{V_c}{W} = \sqrt{\frac{p_\infty - p_v}{\frac{1}{2}\rho W^2}} = \sqrt{\sigma}. \tag{3.25}$$

For a viscous flow vortex, the analytical formulation for the azimuthal velocity distribution of a 2-D cavitating vortex is given in Bosschers (2015). The formulation can be interpreted as a cavitating Lamb-Oseen vortex and reads:

$$V = \frac{\Gamma}{2\pi r}\left\{1 - \beta \exp\left[-\zeta\frac{\left(r^2 - r_c^2\right)}{r_v^2}\right]\right\}, \tag{3.26}$$

with β defined by

$$\beta = \frac{r_v^2}{r_v^2 + \zeta r_c^2}, \tag{3.27}$$

and where ζ is a constant ($\zeta = 1.2564$) defined such that the maximum azimuthal velocity for a non-cavitating vortex occurs at the radius of the viscous core of the non-cavitating vortex r_v.

The formulation was derived using the appropriate jump relations for the stresses at the cavity interface which gives a shear stress in the liquid at the cavity interface that is approximately equal to zero. The condition of zero shear stress results in a small region of solid-body type of velocity distribution near the cavity. The present formulation is different from the Gaussian vortex formulations proposed by (Choi & Ceccio, 2007) and (Choi *et al.*, 2009) who introduce an additional parameter that describes the azimuthal velocity at the cavity interface. The formulation for the azimuthal velocity of the cavitating vortex still needs to be validated by detailed flow field measurements.

Equation 3.26 can be used to derive an analytical expression for the pressure, which is a function of the same parameters. This formulation for the pressure at the cavity radius replaces (3.25) and reads

$$\sigma = \frac{p_\infty - p_v}{\frac{1}{2}\rho W^2} = \frac{\Gamma^2}{2(\pi W r_c)^2} \left\{ \begin{array}{l} \frac{1}{2} - \beta e^{-\zeta r_c^2/r_v^2} + \frac{\beta^2}{2} e^{-2\zeta r_c^2/r_v^2} \\ + \frac{\beta\zeta r_c^2}{r_v^2} E_1\left(\zeta r_c^2/r_v^2\right) \\ - \frac{\beta^2\zeta r_c^2}{r_v^2} E_1\left(2\zeta r_c^2/r_v^2\right) \end{array} \right\}. \tag{3.28}$$

with E_1 the exponential integral. The azimuthal velocity at the cavity radius now corresponds to

$$V_c = \frac{\Gamma}{2\pi r_c} \left\{ \frac{\zeta r_c^2}{r_v^2 + \zeta r_c^2} \right\}. \tag{3.29}$$

This azimuthal velocity can be used in (3.20) and (3.23). It is recognised that the disturbance in the flow due to the cavity deformations is given by a potential flow solution, which is not consistent with the use of a viscous mean flow solution in the kinematic and dynamic boundary conditions. However, the contribution of the azimuthal velocity component to the free stream velocity **U** is expected to lead to small changes to the disturbance potential, which suggests that the use of a viscous vortex solution instead of a potential flow vortex solution will also lead to small changes to the disturbance potential. The use of a viscous flow solution for V_c in the kinematic and dynamic boundary condition leading to (3.20) and (3.23) is only allowed for $n = 0$ and when the Burnham-Hallock vortex is used. Nevertheless, here it is assumed that a generic viscous flow solution can be used for all values of n.

The azimuthal velocity of a non-cavitating and for a cavitating vortex is given in figure 3.3. The potential flow formulation corresponds to (3.7) and the viscous flow formulation corresponds to (3.26). The velocities are obtained using a single value of Γ and r_v for both cases.

3.3. EXPERIMENTAL SETUP

The experimental facility is the cavitation tunnel in the Laboratory for Ship Hydrodynamics at Delft University of Technology. A detailed description of the tunnel is given by Foeth (2008), while the recent modifications are described by Zverkhovskyi (2014).

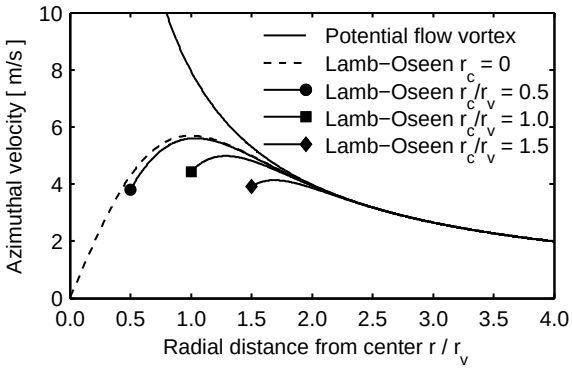

Figure 3.3: Velocity distribution of a potential flow vortex, Lamb-Oseen vortex and three cavitating Lamb-Oseen vortices for $\Gamma = 0.1\ m^2/s$ and $r_v = 2\ mm$.

The maximum free stream tunnel velocity U_∞ is 7 m/s, which is approximately the velocity used in the results presented here. The cross section is 0.30 × 0.30 m^2 at the inlet, but changes downstream in vertical direction to 0.30 × 0.32 m^2 at the outlet. This diffusion compensates for boundary layer growth along the tunnel walls, so that there is no streamwise pressure gradient in the test section. A sketch of the setup is given in figure 3.4. The coordinate system, with the wing tip at the origin, is defined with x pointing in the streamwise direction. The top view (xz) includes the elliptic wing planform with z in the spanwise direction, positive from root to tip. Illumination in the side plane (xy) is partly blocked by the wing mounted on a rotatable disk in the tunnel. The lift direction y is vertically downward.

Tip vortex cavitation is generated by a half-model wing of elliptic planform with an aspect ratio of 3 and a *NACA* $66_2 - 415$ cross section with $a = 0.8$ mean line. The trailing edge was truncated at a thickness of 0.3 mm due to manufacturing limitations. The root chord length after truncation is $c_0 = 0.1256\ m$. The wing has a half span of 0.150 m, so that the tip is positioned in the centre of the test section. The wing is mounted with its spanwise direction horizontally, with the suction side pointing downward, on the side window of the test section on a disk containing a six-component force/torque sensor (ATI SI-330-30).

The water temperature is measured with a PT-100 sensor placed in a quiescent corner outside the main flow downstream of the test section. A digital pressure transmitter (Keller PAA 33X), mounted in the throat of the contraction upstream of the test section, gives the absolute pressure near the wing at a data acquisition rate of 10 Hz. The free stream tunnel velocity is determined from the pressure drop over the contraction measured with a differential pressure sensor (Validyne DP 15) with a number 36 membrane. Both the values of the absolute pressure sensor and the velocity based on the pressure drop are corrected with a reference measurement using a Pitot tube, in an empty test section at the location of the wing.

The dissolved oxygen concentration (DO) was used as a measure of the amount of dissolved gas in the water. A fluorescence-based optical sensor (RDO Pro) was placed

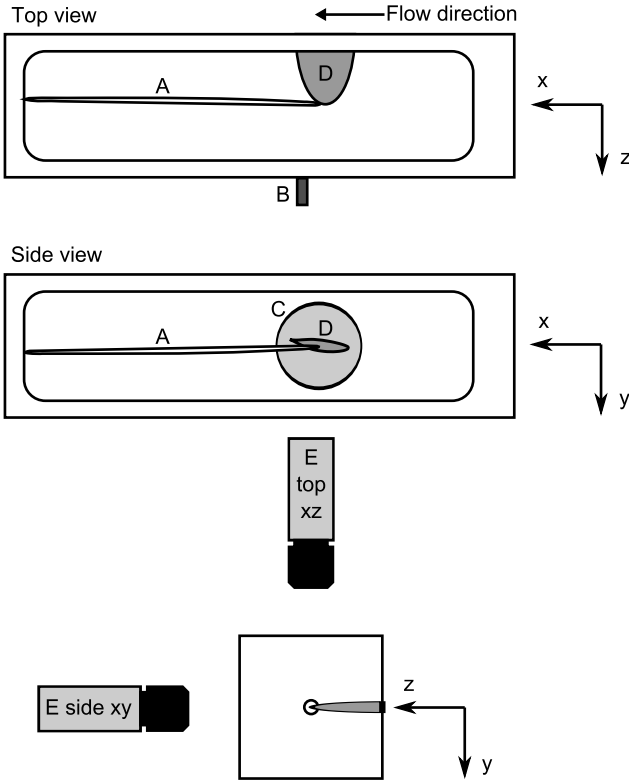

Figure 3.4: Experimental configuration (not to scale) in the cavitation tunnel with tip vortex cavity *A*, hydrophone *B*, disk *C* holding elliptic planform wing *D* and high-speed cameras *E*.

in a sample of water taken from the tunnel at the start and end of each day. The typical accuracy of the sensor is 0.1 mg/l, but due to fluctuations in concentration in the tunnel, 0.5 mg/l is the smallest practical division. As only dissolved oxygen is measured this is taken as a representative indicator for the total amount of dissolved gas.

A hydrophone (Brüel & Kjær type 8103) and a measurement amplifier (Brüel & Kjær type 2606) were used to measure the radiated sound. The hydrophone was inside a water-filled cup mounted on the window opposite to the wing at the vertical position of the tip and the streamwise position of the trailing edge. All sensors were sampled at a rate of 40 kHz which is well above the 1.5 kHz upper limit of the relevant frequency range.

Two high-speed cameras (LaVision Imager Pro HS) in combination with two backlight LED panels gave a shadowgraphy image of the tip vortex cavity at 5×10^3 frames per second. The total recording time, limited by the camera memory, was six seconds. The top view (xz-plane) camera is equipped with a Nikon AF Nikkor 35 mm objective at a f-stop value of 2 with an approximate object focal-plane distance of 0.50 m. The disk holding the wing blocks part of the field of view of the side view (xy-plane) camera. Consequently a 55 mm Micro-Nikkor set to f-stop of 2.8 is used at an object focal-plane distance of 0.57 m.

Edge detection of the tip vortex cavity is based on gradients in light intensity in the image. A Canny (1986) edge detection method was used with a relative gray value intensity threshold of 0.1 and a filter size of 1.0. Units and detailed description of these parameters can be found in Canny (1986). In the xz-plane the tip of the wing is in the field of view and is used to define the origin. As contrast is needed to detect the cavity edge the detected range is between $x/c_0 = 0.19$ to $x/c_0 = 2.48$ downstream of the tip resulting in an equivalent pixel size of 0.16 mm in the object domain. The edge of the disk holding the wing in the xy-plane is taken as $y = 0$. The cavity extent is between $x/c_0 = 1.12$ to $x/c_0 = 2.60$ downstream of the tip with an equivalent pixel size of 0.10 mm in the object domain. The overlap area between both views for which 3-D diameter and location information is available spans $1.35\,c_0$.

The pixelization of the diameter and location data are removed by using a fourth order Chebyshev type II low-pass filter. The cut-off frequency was set to half the Nyquist frequency in both cases. The spatial Nyquist frequency is 20 rad/mm in the xz-plane and 32 rad/mm in the xy-plane. The low-pass filters were applied in forward and reverse direction to prevent phase shift and to double the effective filter order.

3.4. RESULTS

The results are presented as follows. First the sensitivity of the mean cavity diameter to dissolved gas and fluctuations in free stream velocity is discussed. Second, an overview is given of diameter oscillations in the time domain combined with a description of the geometry of the stationary cavity. Third, a frequency-wave number diagram is generated to validate the analytical model for the dispersion relation. Fourth, sound, wing forces and cavity oscillations are correlated. Finally, the frequency of the peak in the cavity diameter spectrum is compared to the frequency of the zero group velocity criterion that can be derived from the analytical dispersion relation and a comparison is made to the data of the 'singing' vortex as given in Maines & Arndt (1997).

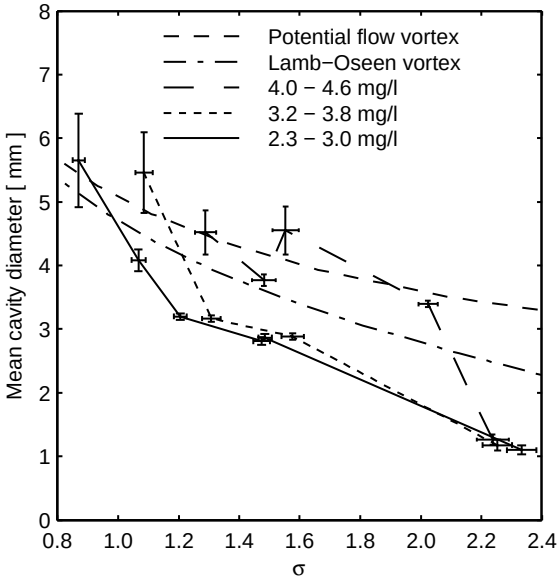

Figure 3.5: Mean cavity diameter in the xz-plane as function of cavitation number for a lift coefficient of C_L = 0.58 and a Reynolds number based on the wing-root chord of $Re = 9 \times 10^5$. Data points are grouped according to dissolved oxygen concentration. The vertical error bars are the streamwise variation of the time-averaged cavity diameter, which is an indication of the size of the stationary wave amplitude as seen in figure 3.6. The horizontal error bars denote the variation in cavitation number. The model vortex lines represent the result of (3.25) for a potential flow vortex and (3.28) for a cavitating Lamb-Oseen vortex using $\Gamma = 0.10\ m^2/s$ and $r_v = 1.7\ mm$.

3.4.1. DISSOLVED OXYGEN CONCENTRATION

In the dispersion relation for the vortex cavity the pressure inside the cavity is assumed to be equal to the vapour pressure. Preparations for the test conditions for which a stationary tip vortex cavity is present can take typically 5 minutes or more during which the tunnel is in operation. Therefore there is sufficient opportunity for dissolved non-condensable gas to diffuse into the cavity. Figure 3.5 is the result of a sensitivity study to show the importance of a low dissolved gas concentration in order to obtain reproducible results. For concentrations below 3.8 mg/l the results show acceptably similar values for cavitation numbers above 1.3.

For a cavitation number of 1.1 the standard deviation in core diameter for concentrations of 3.2 to 3.8 mg/l is larger than for lower concentrations. The general increase in standard deviation is due to the change of the cavity from a cylindrical shape into a twisted ribbon-like cavity shape as shown in figure 3.6. For concentrations above 4.0 mg/l an increase in standard deviation is found for cavitation numbers below 2.2.

The results based on a potential flow vortex give an upper limit to the cavity size as this vortex provides an overestimation of the azimuthal velocity, resulting in a lower pressure and thus a larger cavity. The cavitating Lamb-Oseen vortex takes the viscous core into account, which reduces the azimuthal velocity and gives a smaller estimate for

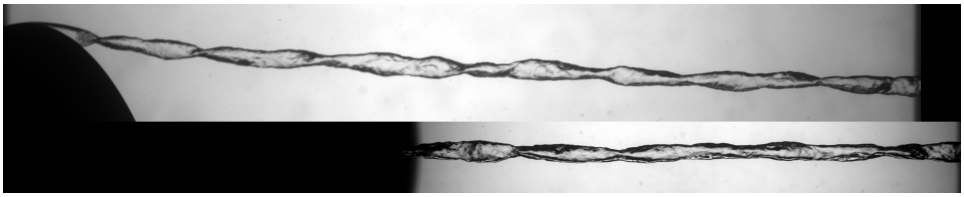

(a) Conditions; $C_L = 0.58$, $\sigma = 0.87$, $Re = 9.1 \times 10^5$ and $DO = 2.7\ mg/l$

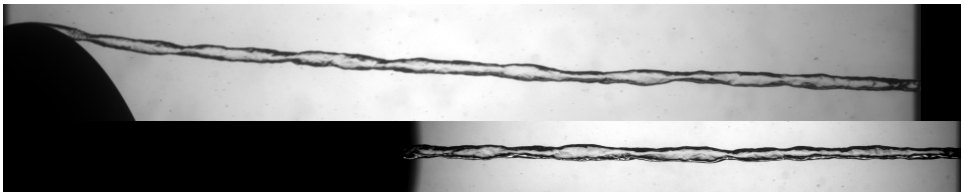

(b) Conditions; $C_L = 0.58$, $\sigma = 1.55$, $Re = 9.1 \times 10^5$ and $DO = 4.4\ mg/l$

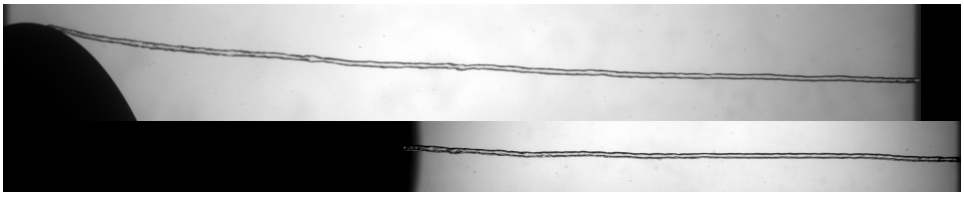

(c) Conditions; $C_L = 0.46$, $\sigma = 1.07$, $Re = 8.9 \times 10^5$ and $DO = 2.7\ mg/l$

Figure 3.6: Combination of vortex cavity images in xz-plane (top) and xy-plane (bottom) of each image. Flow is from left to right with the elliptical black object the pressure side of the wing.

the diameter, which compares reasonably with the spread in the experimental data.

In the current experiment, the drive system of the cavitation tunnel was run at a constant rotation rate of 700 revolutions per minute. Because of an unidentified flow instability in the tunnel, there are large-scale non-periodic velocity excursions as high as 10% of the mean. Within the six-second measurement time used, the standard deviation of the velocity in each measurement remained below 5% with a typical value of 2.5%. As the fluctuations are not periodic, the time for the flow to meet this condition can vary between measurements. A period with low standard deviation was selected by monitoring the tunnel velocity in real time. The consequence of this approach is a difference between measurements in the time for which the cavity is exposed to over-saturated water.

Long exposure times of the tip vortex cavity to over-saturated water and excursions to lower pressures due to higher free stream velocities promote diffusion of gas into the cavity. This increases the mean cavity diameter and promotes the appearance of a stationary wave for higher cavitation numbers. This is expected to be the cause for the decrease in cavity diameter between $\sigma = 1.6$ and $\sigma = 1.4$ for dissolved oxygen concentrations above 4.0 mg/l as seen in figure 3.5.

3.4.2. CAVITY DYNAMICS IN TIME AND FREQUENCY DOMAIN

For the detailed evaluation of the cavity dynamics a single condition is selected corresponding to figure 3.6(b). Out of seven cases with significant volume variations, this case shows the largest indication for the existence of a cavity-resonance frequency. In this case the dissolved gas in the water is highly over-saturated. For later comparison, the condition of figure 3.6(c) is used. This condition corresponds to the condition with the minimum dissolved gas concentration possible in the cavitation tunnel.

The temporal oscillations of the cavity diameter are expected to be a combination of the $n = 0^{\pm}$ and $n = 2^{\pm}$ modes as presented in figure 3.1. As two separate views are available, the identification has to be made by combining both views. Figure 3.7 shows a colour coded tip vortex cavity diameter for the xz-plane, (top view) in the top figure and xy-plane, (side view) in the bottom figure over a time span of 0.2 seconds.

As is already evident from figure 3.6(b), both views in figure 3.7 show stationary wave patterns for the two cameras with 180 degrees phase difference. This could be interpreted as a cavity with an elliptical shape with the axes rotating in the downstream direction. From a single view this shape is similar to a standing wave, but as the frequency of oscillation is zero it is actually a stationary wave. To guide the eye a black line is drawn with a slope corresponding to a velocity 19% higher than the free stream velocity U_∞. This value results from the analysis of figure 3.10(a). The peak values of diameter appear to be convected with a velocity close to this value. The increase in axial velocity with respect to the free stream velocity near the core is due to the favorable streamwise pressure gradient generated by the roll-up of the wing vorticity increasing tip vortex circulation. High C_L and small r_c values give increased axial velocities.

The graphs on the right of figure 3.7 are averages over the whole spatial domain and present the variation of the spatial mean diameter in time. The general trend over 0.2 seconds shows that there are low-frequency changes in mean diameter that might be due to changes in free stream velocity, which are of the same time scale. The phase angle

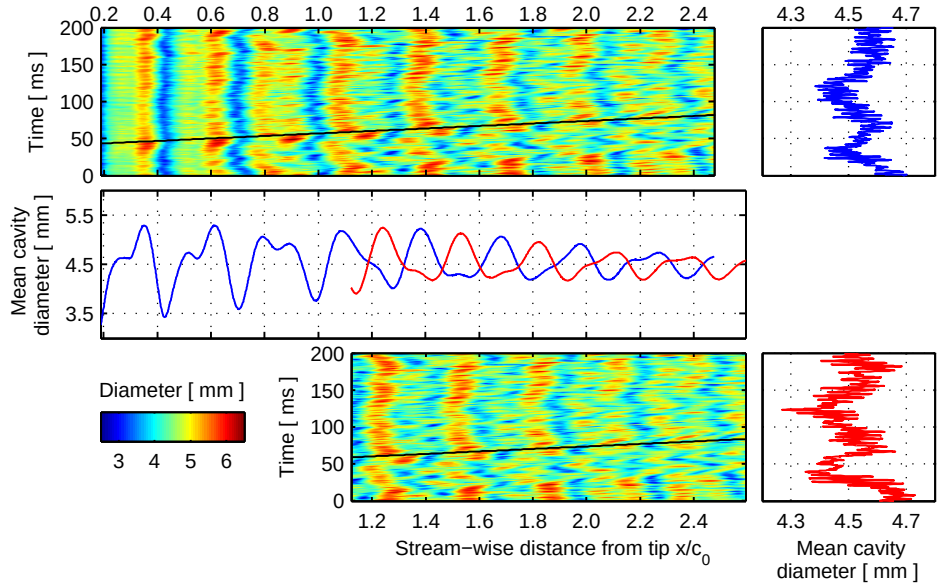

Figure 3.7: Variation of cavity diameter in time and space. Top: in the xz-plane (top view) and bottom: xy-plane (side view), black line indicates convection at $1.19\,U_\infty$. The graph in the middle is the time averaged diameter with the blue line corresponding to the xz-plane and the red line to the xy-plane. The graphs on the right are the spatial averages. Conditions of figure 3.6(b).

between the two planes of the averaged cavity diameter in space is approximately zero.

The dominant stationary wave pattern present on the surface of the cavity has a direct relation with the diameter. The values for the maximum cavity diameter and the stationary wave length are compared in figure 3.8 with data of Maines & Arndt (1997). In this figure the filled symbols are the current results using the maximum of the time averaged cavity diameter. The general trend is the same for both studies.

A frequency analysis of the diameter variations in time as seen in the xz-plane (top view) was performed and the results are presented in figure 3.9 as a function of streamwise distance. This case was specifically selected due to the presence of a tonal frequency component at 170 Hz, which can clearly be detected in the graph.

The variation of the diameter amplitude in streamwise direction is smallest close to the tip. Further downstream, the amplitude of the fluctuations increases over a broad frequency range between 0 and 200 Hz. At very low frequencies the contribution of the stationary cavity shape is very large as indicated by the red patches.

3.4.3. CAVITY DYNAMICS IN WAVE NUMBER - FREQUENCY DOMAIN

Information about the three wave modes comes from the relation between the wave number and the frequency of the oscillation, which can be obtained from a 2-D Fast Fourier Transform (FFT) of the high-speed video observations. The $n = 0$ and $n = 2$ modes are related to diameter variations while the $n = 1$ mode is based on motion of the centreline. The $n = 0$ and $n = 2$ modes can be distinguished by the phase difference of

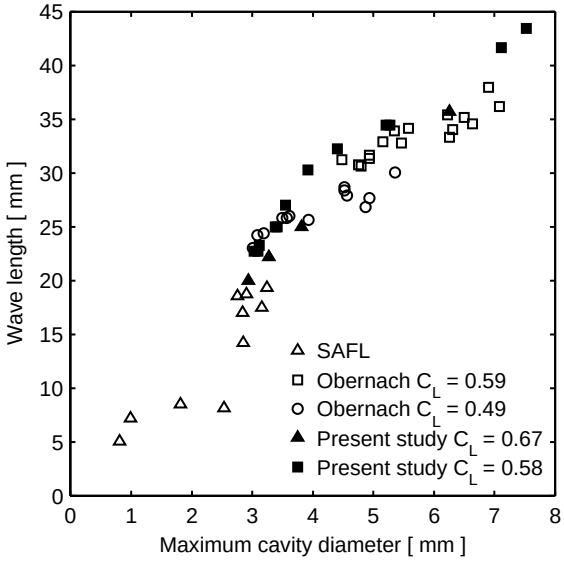

Figure 3.8: Comparison of the wave length of the stationary cavity shape as function of maximum cavity diameter, data from Maines & Arndt (1997) at SAFL and Obernach is presented by open symbols and of the present study by filled symbols.

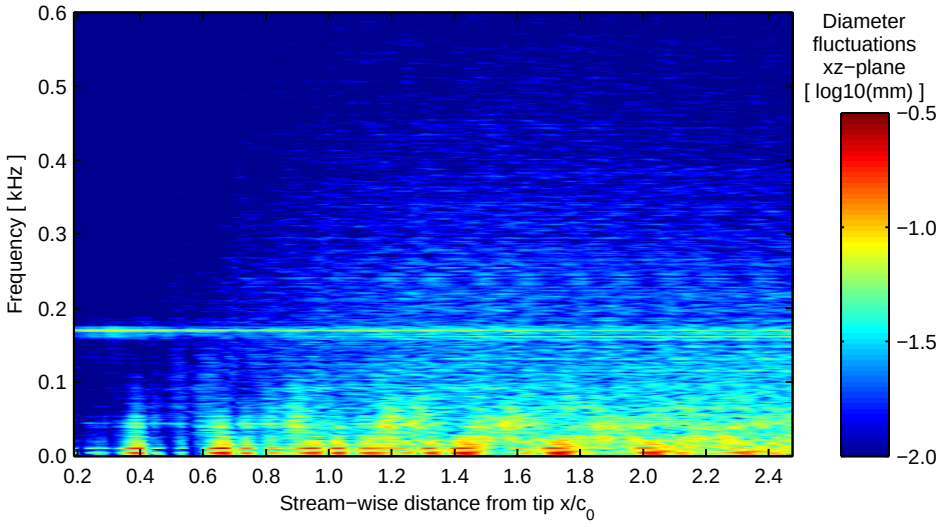

Figure 3.9: Amplitude spectrum of variations of cavity diameter. Conditions of figure 3.6(b). The bright horizontal line corresponds to a high amplitude narrow band frequency component at 170 Hz.

the observations in the xz-plane and the observations in the xy-plane, corresponding to 0 degrees and 180 degrees, respectively. The diameter data from the xz-plane is analysed as it captures the largest streamwise variation, hence it provides the highest resolution in wave number. The result is given in figure 3.10(a).

Features in the amplitude spectrum and phase spectrum of figure 3.10 can be understood using the observations of the previous figures. The amplitude of the background disturbance is around 10^{-5} mm while the significant features have an amplitude of 10^{-2} mm. The main feature can be represented by a straight line indicated by the dashed line and cannot directly be related to the dispersion relation of (3.20). The slope of the line is the group velocity $\partial\omega/\partial k_x$. In this case the group velocity is constant and is 19% faster than the free stream velocity as also observed in figure 3.7. This can be interpreted as small perturbations present on the surface of the cavity which are directly related to disturbances in the free stream. These disturbances are not included in the theoretical model. The faint lines with equal slope are harmonics of this contribution and are the result of the FFT of a signal that is not perfectly sinusoidal. Another notable feature of the line is the location where it crosses the zero frequency axis, at approximately 0.2 rad/mm. This corresponds to the dominant stationary wave pattern seen in figure 3.7 and is used for figure 3.8.

Two other features in Fig. 3.10 that are high in amplitude do not correspond to free stream convection. To understand these contributions the lines of the $n = 0^-$ and the $n = 2^-$ modes of the dispersion relation of (3.20) are matched to these features to obtain the core angular velocity Ω using the mean value for r_c. The positive counterparts of these modes, which can be seen in figure 3.2, are only shown when present inside the wave number - frequency range of the experimental results. The $n = 2^+$ mode is therefore not considered at all. From the values of Ω at different cavitation numbers, the local circulation and viscous core size of the tip vortex can be obtained using a least-squares fit using (3.29). The results are given in the captions and the validity of these numbers will be discussed later.

The $n = 0^-$ mode follows the feature that crosses the zero-frequency line at the wave number of 0.4 rad/mm. The dash-dotted line is the $n = 2^-$ mode, which is the second to top feature. These modes can be distinguished by the phase difference in diameter between the xz-plane and the xy-plane. The data on the xz-plane is interpolated onto the xy-plane in the area of overlap. The phase difference in the frequency domain between these planes is presented in figure 3.10(b).

Here the same features as in figure 3.10(a) can be identified. The contribution of the convection has a clear 180 degrees phase difference that can be related to the geometry of the stationary wave of figure 3.7. Any other waves superimposed on this do not have high enough amplitude to offset this basis. The harmonics in figure 3.10(a) of this line are present at zero phase difference. These features, with a slope equal to the convection line, are thus clearly disturbances related to the free stream flow.

The feature below this line has a clear zero degree phase difference, which supports that this is the $n = 0^-$ volume variation mode. The other feature, which has a 180 degree phase difference, was matched to the $n = 2^-$ mode confirming the effect of the rotation of an ellipsoidal cross section. The $n = 0^+$ mode cannot be identified in either figure 3.10(a) or figure 3.10(b). This could be due to a group velocity that is higher than

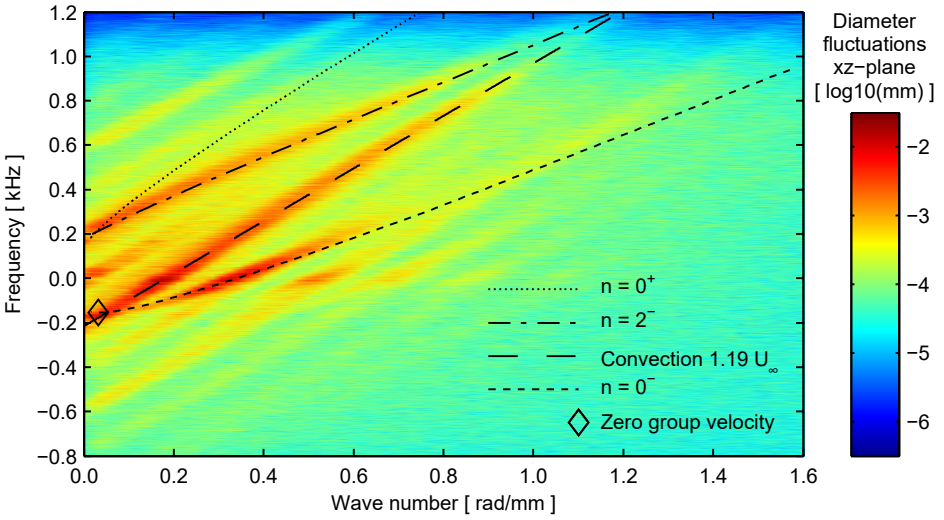

(a)

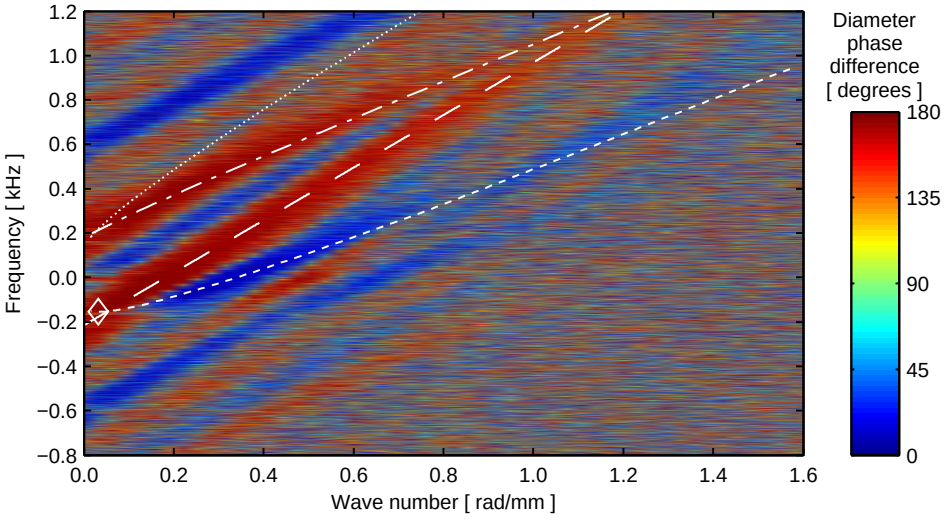

(b)

Figure 3.10: Wave number - frequency amplitude (a) and phase spectrum (b) at the condition of figure 3.6(b). Included are the lines for the breathing $n = 0^{\pm}$ and helical $n = 2^{-}$ modes and a line for constant group velocity that is 19% higher than the tunnel free stream velocity. Derived quantities; $\Omega = 2.0 \times 10^3$ rad/s, $r_c = 2.3$ mm, $r_v = 1.9$ mm and $\Gamma = 0.10$ m^2/s.

all other modes and little energy transfer takes place with other modes.

The displacement mode $n = 1$ is evaluated by analysis of the fluctuations of the cavity centreline. The result is presented in figure 3.11(a). Here the contributions of convection and its harmonics are dominant. The dashed line has a 14% larger velocity than the free stream velocity. The uncertainty of estimation of the slope of the convection line is typically ±1%. The high amplitudes near the origin are mainly due to the curved trajectory of the mean centreline in the xz-plane. The line originating from here with a smaller slope than the convection line is matched to the $n = 1^-$ line with the same value for Ω as figure 3.10(a). The $n = 1^+$ mode is not observed in the fluctuations of the position of the centreline.

To determine whether the theoretical dispersion relation is able to predict differences in experimental conditions a comparison to a case at the conditions of figure 3.6(c) is made. This results in a smaller cavity diameter and different cavity dynamics. The identification of the data and the plotted lines in figure 3.12 is similar to figure 3.10.

The difference in the value for the convection velocity is related to the local streamwise velocity near the vortex cavity. For a case without cavitation the axial flow in the centre of a vortex core is higher than the free stream (Arndt & Keller, 1992). The axial velocity decreases away from the vortex core to the undisturbed free stream value. This results in a higher local axial velocity for a smaller diameter vortex cavity in comparison to a larger diameter vortex cavity and thus a higher convection velocity.

As the stationary wave pattern has a higher wave number due to a smaller cavity diameter and thus a higher azimuthal velocity, the zero frequency crossing of the dashed line is now around 0.30 rad/mm. The slope in this case is 12% higher than the free stream velocity. The theoretical dispersion relation is well able to account for the differences in experimental conditions as seen from the match between the lines and features in the spectrum. The $n = 0^+$ mode is only observed in the phase difference of figure 3.12(b).

The convection of the centreline disturbances with the free stream velocity is faint in figure 3.11(b) and slower than the convection in figure 3.12(a). The amplitude around the origin is more pronounced than in figure 3.11(a). The amplitude of these centreline waves is small and thus difficult to distinguish in the time domain. The fluctuations of the free stream tunnel velocity occurs typically with a 5 second period which is far beyond the time scale used in the present analysis.

The cavity angular velocity that was obtained from the fit of the dispersion relation of (3.20) to the experimental data depends on the value for the axial velocity. The dispersion relations shown in figure 3.10(a) and 3.12(a) are obtained by using the undisturbed free stream velocity but the effect of other choices has also been investigated. Main conclusions from this sensitivity study are that the best fit for the $n = 2^-$ mode is obtained using the undisturbed free stream velocity, while the best fit for the $n = 0^-$ mode is obtained using the fitted value for the convection velocity. This results in a lower and upper estimate for the cavity angular velocity shown in figure 3.13, which differ by approximately 10%. Both fits give a better agreement than the fits shown in figure 3.10(a) and 3.12(a).

This procedure was followed for 12 and 4 measurements at $C_L = 0.58$ and $C_L = 0.67$ respectively, while varying the cavitation number, resulting in a range of cavity radii. The cavitating Lamb-Oseen vortex of (3.29) was then used to find the values for the vortex cir-

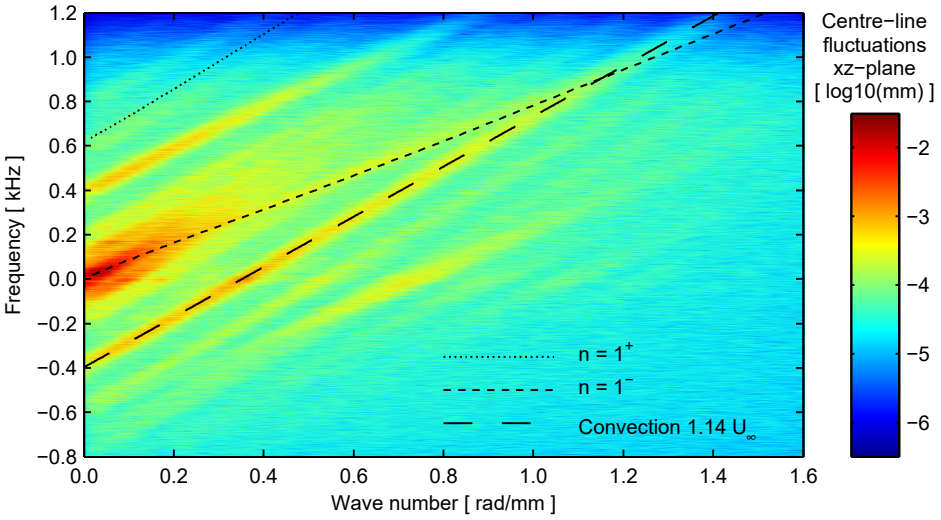

(a)

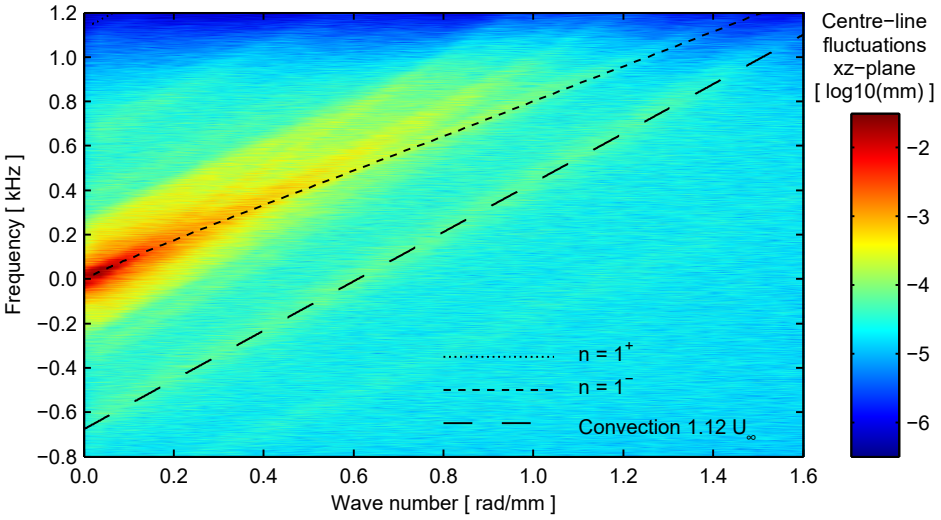

(b)

Figure 3.11: Wave number - frequency amplitude of centreline fluctuations at (a) the condition of figure 3.6(b) on the top and (b) at the condition of figure 3.6(c) on the bottom. Included are the lines for the serpentine $n = 1^{\pm}$ and a line for constant group velocity that is 14% and 12% larger than the tunnel free stream velocity.

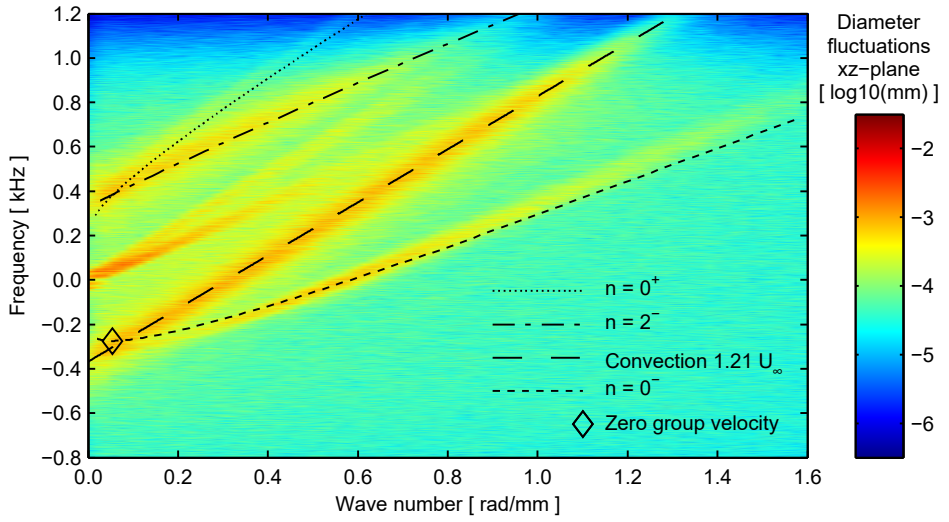

(a)

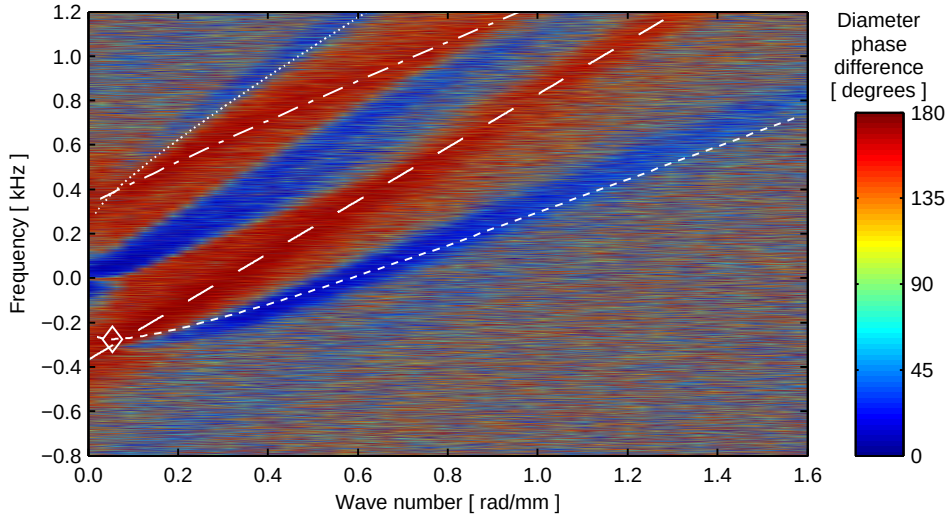

(b)

Figure 3.12: (a) Wave number - frequency amplitude (b) phase spectrum at the condition of figure 3.6(c). Included are the lines for the breathing $n = 0^{\pm}$ and helical $n = 2^{-}$ modes and a line for constant group velocity that is 21% larger than the tunnel free stream velocity. Derived quantities: $\Omega = 3.6 \times 10^3\ rad/s$, $r_c = 1.1\ mm$.

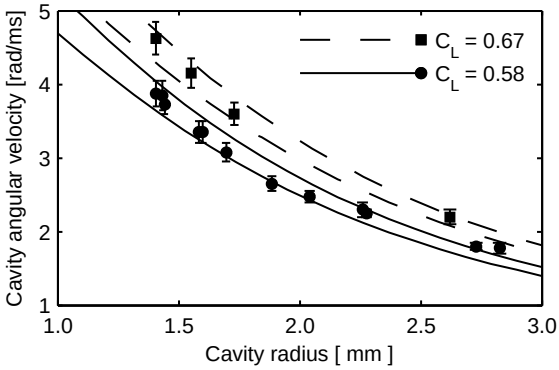

Figure 3.13: Comparison between values of Ω obtained from matching the dispersion relation of (3.20) to the experimental data and the model value lines using (3.29). Bars represent the range between the lower and upper estimate of Ω .Conditions; $C_L = 0.67$, $r_v = 1.7-1.8\ mm$, $\Gamma = 0.12-0.13\ m^2/s$ and $C_L = 0.58$, $r_v = 1.7\ mm$, $\Gamma = 0.10-0.11\ m^2/s$.

C_L	0.58	0.67
Γ/Γ_0	0.44 - 0.47	0.47 - 0.49
r_v/δ	0.58 - 0.56	0.61 - 0.58

Table 3.1: Derived characteristics of tip vortex based on matching of dispersion relation of (3.20) to experimental data in figures 3.10(a)-3.12(b). The left and right value correspond to the lower and upper estimate of Ω, respectively.

culation and viscous core size. The local circulation of the tip vortex can be related to the wing circulation at the root $\Gamma_0 = \frac{1}{2} c_0 C_L U_\infty$ that can be analytically obtained for a wing with elliptic loading distribution. The wing lift coefficient is defined as $C_L = L/(\frac{1}{2}\rho U_\infty^2 S)$, where L is the lift force, with wing surface area $S = 1.465 \times 10^{-2}\ m^2$ for the present wing. The viscous core size can be related to an equivalent turbulent boundary layer thickness δ on a flat plate with a length equal to the chord c_0 of the wing root. Here, $\delta = 0.37 c_0 Re^{-0.2}$ is used, similar to Astolfi *et al.* (1999). The Reynolds number $Re = U_\infty c_0/\nu$ is based on the wing root chord c_0 and kinematic viscosity ν. The values for Γ/Γ_0 and r_v/δ for each C_L are given in table 3.1. The final comparison of the experimental data and the data of the model using the values of table 3.1 is shown in figure 3.13. For the determination of these two parameters the azimuthal velocity of the Lamb-Oseen vortex has been considered. No assumption is made based on the pressure inside the cavity.

Astolfi *et al.* (1999) found values of $\Gamma/\Gamma_0 = 0.5$ to 0.6 and $r_v/\delta = 0.8$ to 1.0 at one chord length downstream of the tip on comparable elliptic planform wings with *NACA* 16020 and *NACA* 0020 airfoil sections. The values for Γ/Γ_0 are very close to the expected range and those for r_v/δ are slightly lower. The latter could be due to the smaller ratio of the airfoil thickness to chord and the large extent of the laminar boundary layer for which the presently used *NACA* $66_2 - 415$ airfoil section was designed.

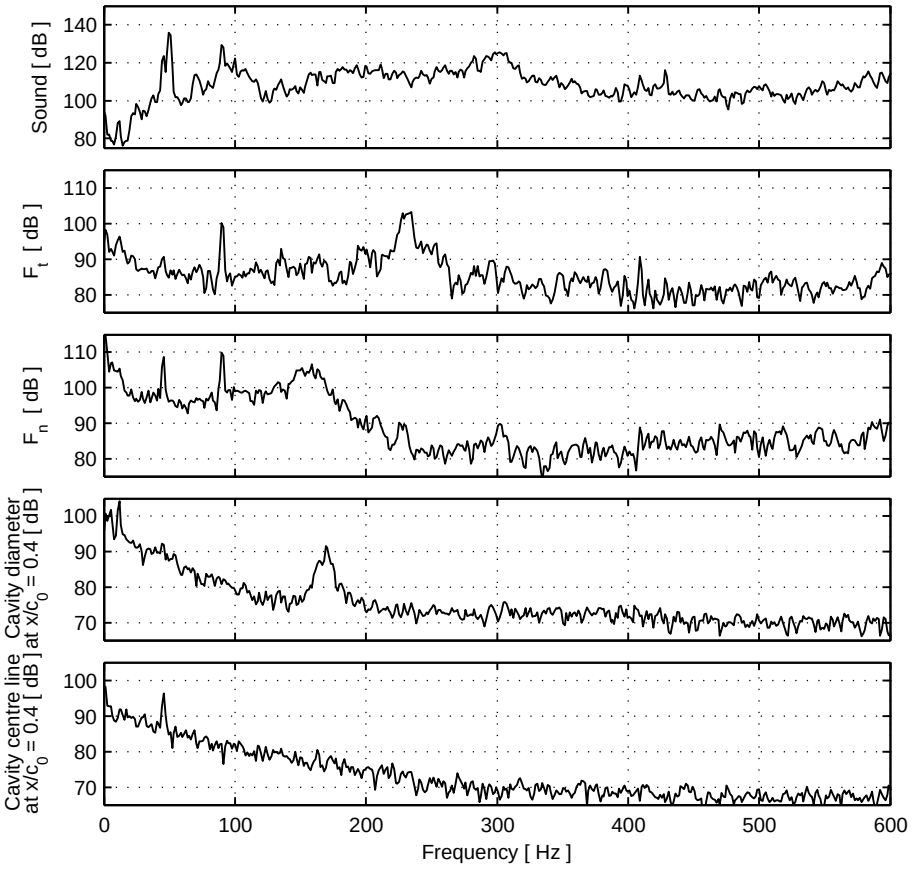

Figure 3.14: From top to bottom a comparison between power density spectra of the sound signal, the force tangential to the wing chord, the force normal to the wing chord, fluctuations cavity diameter and fluctuations cavity centreline position. Reference value is $10^{-12}\ Pa^2/Hz$, $10^{-12}\ N^2/Hz$ and $10^{-12}\ mm^2/Hz$, respectively. Condition of figure 3.6(b).

3.4.4. SOUND MEASUREMENTS

Ten of the cases considered showed an indication of the presence of an resonance frequency in the variations of the cavity diameter. During the experiments no 'singing' vortex could be heard, in contrast to experiments by others (Higuchi *et al.* (1989); Briançon-Marjollet & Merle (1997); Maines & Arndt (1997); Astolfi *et al.* (1998)). The sound spectrum measured is presented in figure 3.14. It shows a comparison of the sound spectrum with the spectrum of the tangential and normal components of the forces, the cavity diameter and fluctuations of the location of the centreline.

The peak at 170 Hz in the cavity-diameter spectrum does not correspond to any peaks in the spectrum of the sound or force signals. From the bottom graph in figure 3.14 it is clear that the 170 Hz frequency component is not present in the fluctuations of the position of the centreline.

The peaks in the spectrum at 220 Hz for the tangential force and at 150 Hz for the normal force are the first two wing resonance frequencies as determined by applying an impulse load to the wing (submerged at rest). This was done approximately 25 times in order to obtain a reliable estimate of the resonance frequencies.

Several other peaks in the spectra are attributed to the experimental setup. At 47 Hz the first blade rate harmonic of the four bladed impeller of the tunnel drive arises with a second harmonic at 94 Hz that are picked up in the sound spectrum, the force on the wing and in the spectrum of the cavity centreline position. At 50 Hz electronic noise from the power supply is picked up. At 300 Hz a more broadband response caused by cavitation of the impeller of the tunnel drive is observed. The sound measured in the tunnel without the hydrofoil increases by approximately 30 dB around 300 Hz when increasing the tunnel drive rotation rate from 400 to 700 revolutions per minute. The sound can be identified as cavitation noise by listening at a position close to the tunnel impeller.

The high-amplitude narrow-band frequency component of the fluctuations of the cavity diameter at 170 Hz could not be related to any part of the experimental setup. It also changes in frequency with cavity size and vortex strength. It is thus likely that it is the cavity resonance frequency for volume variations that is however, not sufficiently excited within the present tunnel background noise to produce sound of significant amplitude.

3.4.5. CAVITY RESONANCE FREQUENCY

Maines & Arndt (1997) described that the frequency of a 'singing' vortex correlated well with the fluctuations in the length of a small sheet cavity but only when the vortex cavity was connected to the tip of the wing. In the current study, the tip vortex cavity was always connected to the wing but was very stable and showed no periodic oscillation to a casual observer. Although no tip instability and no 'singing' vortex sound was observed, figure 3.14 does show a strong narrow-band component in the variations of the cavity diameter.

The current hypothesis is that a tip vortex cavity has a certain resonance frequency. It can be excited by forcing of deformations with a matching frequency and wavelength resulting in emission of audible sound. For the forcing to have a matching characteristic frequency some feedback mechanism should be present. The oscillations of the sheet cavity on the wing close to the tip generates waves on the cavity of the vortex that in turn impose the frequency of oscillation on the sheet. This condition requires waves to travel upstream, thus having a negative phase velocity ω/k.

For a strong amplification of cavity waves to occur, wave energy should be contained in space. In the dispersion relation of the $n = 0^-$ mode there exists a criterion at which the velocity of wave energy is zero. This criterion can be identified best in figure 3.12(a) as the frequency at which the slope of this line becomes zero. At this criterion the frequency is negative, thus resulting in a negative phase velocity. The convection line intersects the $n = 0^-$ line at this criterion. The convection velocity is always positive and is thus a potential source for wave energy to be transferred to the $n = 0^-$ mode.

The spectrum of the cavity diameter of figure 3.14 shows that a narrow-band peak is present with a centre frequency of approximately 170 Hz that coincides precisely with the zero group velocity criterion in figure 3.10(a). The centre frequency of the peak in

the spectrum of the variations in diameter is determined for 10 conditions varying in cavitation number and lift coefficient. The result for $C_L = 0.58$ is plotted in figure 3.15 together with the data on the 'singing' vortex from Maines & Arndt (1997), which were obtained using sound measurements. The lines are based on the dispersion relation model of (3.20) using a potential-flow vortex and the Lamb-Oseen vortex to relate the cavity radius to the cavitation number, similar to (Bosschers, 2009). The effect of these two models on the relation between the cavitation number and cavity radius was also shown in figure 3.5.

The model based on the potential flow vortex is acceptable for large cavities, but for small cavities it is essential to include the effect of viscosity in order to obtain a representative description of the cavity-resonance frequency. This is the main reason why in Fig. 3.15 the solid data points do not overlap with the results for the 'singing' vortex cases represented by the open symbols. The Reynolds number *Re* is lower in the present study than in the case for the Obernach cases. For an equal *Re* the wing root chord in the present study is larger than the SAFL cases. Both result in a lower cavity rotational frequency Ω giving a lower cavity-resonance frequency. The lines for the model in the present study are based on the values in Table 3.1. For the Obernach cases an estimate of Γ was made using the same ratio for Γ/Γ_0 as found in the present study. The viscous core size was estimated based on the best description of the 'singing' vortex frequencies.

Although the description of Ω by the cavitating Lamb-Oseen model is reasonable, as shown in figure 3.13, there is still an overestimation of the cavity radius with respect to cavitation number as seen in figure 3.5. The correct modelling of the velocity field in a cavitating tip vortex and estimation of the cavity size require improvement which is outside the scope of this experiment.

3.5. DISCUSSION

The wing geometry used in the study by Maines & Arndt (1997) was used here to study tonal sound emission. However, a 'singing' vortex was not observed. Four differences were identified between the experiments that may have caused this; dissolved gas, viscous effects in the vortex, geometry of the wing trailing edge and the state of the boundary layer.

As mentioned in subsection 3.4.1 the dissolved gas concentration can affect the mean cavity diameter, which in turn changes the parameters for the dynamics of the cavity deformation. Unfortunately for some of the experiments a sufficiently low dissolved gas concentration was not possible, which implies that a certain cavitation number may give different mean cavity diameters as seen in figure 3.5. The in-gassing only results in an altered pressure difference over the interface thus a larger cavity and lower angular velocity. This effect is similar to decreasing the free stream pressure or cavitation number. Because the only relevant vortex parameters in the dispersion relation are the cavity diameter and the cavity angular velocity, the dissolved gas content is not considered as a plausible cause for the absence of 'singing'.

The experiments in the present study were conducted in a facility comparable in size to the Obernach tunnel and at similar Reynolds numbers as the experiments in the SAFL tunnel (Maines & Arndt, 1997). The consequence of the lower maximum free stream velocity at the Delft facility is that the tunnel free stream pressure needs to be lowered in

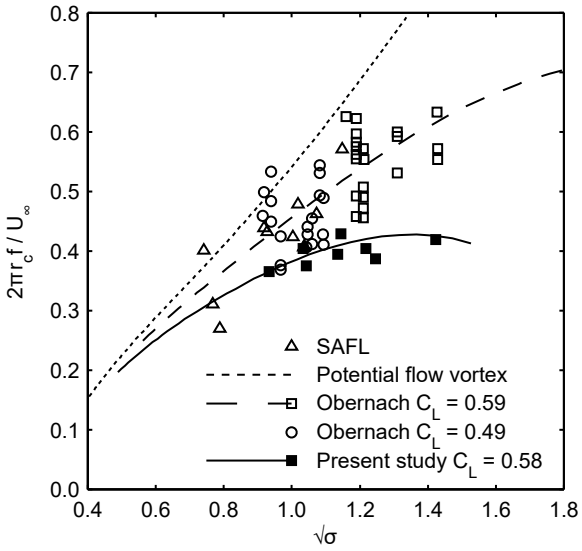

Figure 3.15: Comparison of dimensionless frequency as function of $\sqrt{\sigma}$ between the data from Maines & Arndt (1997) at SAFL and Obernach (open symbols) and the current results (solid symbols). The lines are based on the zero group velocity criterion of the $n = 0^-$ mode of (3.20) using either the potential flow vortex or the cavitating Lamb-Oseen vortex. Model values for Obernach data; $r_v = 1.2\ mm$ and $\Gamma = 0.20\ m^2/s$. Model values for present study; $r_v = 1.7\ mm$ and $\Gamma = 0.10\ m^2/s$. For consistency with the dimensionless frequency the results of the lower estimate of Ω in table 3.1 are used for the lines for the models.

order to obtain an equal cavitation number. Without a dedicated degassing system the gas saturation in the water is higher in the present study. A comparison at equal Reynolds number can only be made between cases with different wing size. The larger wing chord and lower velocity in the present study both contribute to a lower cavity angular velocity, thereby lowering the cavity resonance frequency.

Both the effect of a larger cavity due to gas diffusion into the cavity and the increase of the size of the core of the viscous vortex can influence the characteristic frequency of the vortex cavity as well as the sheet cavity at the tip. A repeat test was performed in a different facility to investigate potential discrepancies. The wing shape is identical to the one used here but scaled-down from a 0.15 m span to a 0.1125 m span. The test was performed at China Ship Scientific Research Center in Wuxi. Sound measurements and high-speed video observations were performed to identify a 'singing' vortex. After a thorough tunnel degassing procedure though without accurate measurement of the dissolved gases, for $C_L = 0.4$ to 0.6, $Re = 0.6\times10^6$ to 1.5×10^6 and $\sigma = 0.40$ to 2.60 no sound originating from a 'singing' vortex was observed. So both the mismatch in dissolved gas concentration and that in Reynolds number are not considered as the cause for the absence of a 'singing' vortex.

In an early stage of the current experiment a choice was made for the truncation of the trailing edge, this based on all available information. Unfortunately, the original wing could not be retrieved from the facility in Obernach where part of the experiments of Arndt & Keller (1992) and Maines & Arndt (1997) were performed. The blunt trailing edge with square corners of the current wing is expected to eliminate any flow instability near the tip and is thus considered responsible for the absence of a 'singing' vortex in the present experiments. Another potential cause for elimination of the flow instability is the boundary layer state close to the tip. This could be due to the absence of a laminar separation bubble possibly due to early surface-roughness induced transition to turbulence.

3.6. CONCLUSIONS

Study of a tip vortex cavity generated by a wing of elliptic planform has provided a fundamental understanding of the dynamics of the cavity interface in a cavitating vortex. High-speed video recordings from two points of view have been used to compute wave number - frequency spectra that clearly show different modes of the variations in cavity diameter and deformations of the centreline. An analytical model for the dispersion relation of disturbances on an infinite cavitating vortex (Thomson, 1880; Bosschers, 2008) is matched to the experimental data using values for vortex parameters that are similar to the values found by Astolfi *et al.* (1999). The model describes the relation between wave number and frequency over the entire range of experimental data very well. However, not all features in the experimental data are part of the theoretical model such as the stationary ellipsoidal shape of the cross section of the cavity and the convection of disturbances at constant group velocity just above the tunnel free stream velocity.

In all cases with sufficient cavity size, 10 cases were found with a dominant oscillation frequency of the cavity diameter. These frequencies coincide with the location in the dispersion diagram at which the group velocity of the $n = 0^-$ mode is zero. This group velocity criterion also gives a good estimate for the 'singing' vortex frequencies found by

Maines & Arndt (1997) for a wing of identical planform and cross section. Despite the presence of a dominant oscillation frequency in the diameter spectra, sound production by the vortex cavity was not measured at any of the conditions of the present experiment. It is concluded that a 'singing' vortex does not occur when there is no strong excitation by a flow instability on the wing tip interacting with the cavitating vortex.

REFERENCES

ARNDT, R.E.A. & KELLER, A.P. 1992 Water Quality Effects on Cavitation Inception in a Trailing Vortex. *Journal of Fluids Engineering* **114**, 430–438.

ASTOLFI, J.-A., BILLARD, J.-Y., DORANGE, P. & FRUMAN, D.H. 1998 Pressure Fluctuations Associated with Tip Vortex and Surface Cavitation. In *Proceedings of the ASME Fluids Engineering Division Summer Meeting*. Washington D.C., USA.

ASTOLFI, J.-A., FRUMAN, D.H. & BILLARD, J.-Y. 1999 A Model for Tip Vortex Roll-up in the Near Field Region of Three-Dimensional Foils and the Prediction of Cavitation Onset. *European Journal of Mechanics - B/Fluids* **18** (4), 757–775.

BOSSCHERS, JOHAN 2007 Broadband Hull Pressure Fluctuations and Cavitating Vortices. In *Proceedings of the Ship Noise and Vibration Conference*. London, United Kingdom.

BOSSCHERS, JOHAN 2008 Analysis of Inertial Waves on Inviscid Cavitating Vortices in Relation to Low-Frequency Radiated Noise. In *Proceedings of the Warwick Innovative Manufacturing Research Centre (WIMRC) Cavitation: Turbo-machinery and Medical Applications Forum*. Warwick University, United Kingdom.

BOSSCHERS, J. 2009 Investigation of the Resonance Frequency of a Cavitating Vortex. In *Proceedings of the NAG/DAGA International Conference on Acoustics*. Rotterdam, The Netherlands.

BOSSCHERS, J. 2015 An Analytical Solution for the Viscous Flow around a 2-D Cavitating Vortex. *Submitted to Journal of Fluids Engineering* .

BRIANÇON-MARJOLLET, L. & MERLE, L. 1997 Inception, Development and Noise of a Tip Vortex Cavitation. In *Proceedings of the Twenty-First Symposium on Naval Hydrodynamics*.

BURNHAM, D.C. & HALLOCK, J.N. 1982 Chicago Monostatic Acoustic Vortex Sensing System. *Tech. Rep.* DOT-TSC-FAA-79-18, IV. U.S. Department of Transportation.

CANNY, JOHN 1986 A Computational Approach to Edge Detection. *IEEE Transactions on Pattern Analysis and Machine Intelligence* **PAMI-8** (6), 679–698.

CHOI, JAEHYUG & CECCIO, STEVEN L. 2007 Dynamics and Noise Emission of Vortex Cavitation Bubbles. *Journal of Fluid Mechanics* **575**, 1–26.

CHOI, JAEHYUG, HSIAO, CHAO-TSUNG, CHAHINE, GEORGES & CECCIO, STEVEN 2009 Growth, Oscillation and Collapse of Vortex Cavitation Bubbles. *Journal of Fluid Mechanics* **624**, 255–279.

FOETH, EVERT-JAN 2008 The Structure of Three-Dimensional Sheet Cavitation. PhD thesis, Delft University of Technology, Delft, The Netherlands.

HIGUCHI, H., ARNDT, R.E.A. & ROGERS, M.F. 1989 Characteristics of Tip Vortex Cavitation Noise. *Journal of Fluids Engineering* **111**, 495–501.

HOWE, M.S. 2003 *Theory of Vortex Sound*. Cambridge University Press.

KELLER, JAKOB J. & ESCUDIER, M.P. 1980 Theory and Observations of Waves on Hollow-Core Vortices. *Journal of Fluid Mechanics* **99** (3), 495–511.

MAINES, B. & ARNDT, R.E.A. 1997 The Case of the Singing Vortex. *Journal of Fluids Engineering* **119**, 271–276.

MOROZOV, V.P. 1974 Theorectical Analysis of the Acoustic Emission from Cavitating Line Vortices. *Soviet Physics. Acoustics* **19** (5), 468–471.

PENNINGS, P.C., BOSSCHERS, J., WESTERWEEL, J. & VAN TERWISGA, T.J.C. 2015 Dynamics of isolated vortex cavitation. *Journal of Fluid Mechanics* **778**, 288–313.

RÆSTAD, ARNT EGIL 1996 Tip Vortex Index - An Engineering Approach to Propeller Noise Prediction. *The Naval Architect* pp. 11–14.

SAFFMAN, P.G. 1995 *Vortex Dynamics*. Cambridge University Press.

THOMSON, SIR WILLIAM 1880 Vibrations of a Columnar Vortex. *Philosophical Magazine Series 5* **10** (61), 155–168.

ZVERKHOVSKYI, OLEKSANDR 2014 Ship Drag Reduction by Air Cavities. PhD thesis, Delft University of Technology, Delft, The Netherlands.

4

FLOW FIELD MEASUREMENT AROUND VORTEX CAVITATION

Models for the center frequency induced by pressure fluctuations of vortex cavitation, in a flow around propellers, require knowledge of the vortex strength and size of the vapor cavity. For this purpose, stereoscopic particle image velocimetry (PIV) measurements were taken downstream of a stationary half wing model. A high spatial resolution is required and was obtained via correlation averaging. This reduces the size of the interrogation area by a factor of 2–8, with respect to the interrogation area in conventional PIV measurements. Vortex wandering was accounted for by selecting PIV images for a given vortex position, yielding sufficient data to obtain statistically converged and accurate results, both with and without a vapor-filled vortex core. Based on these results, the low-order Proctor vortex model was applied to describe the tip vortex velocity field outside the viscous core, and the cavity size as a function of cavitation number. The flow field around the vortex cavity shows, in comparison to a flow field without cavitation, a region of retarded flow. This layer around the cavity interface is similar to the viscous core of a vortex without cavitation.

This chapter has been published in Experiments in Fluids **56** (Pennings *et al.* (2015*b*)). The suggestions of Jerke Eisma and Sedat Tokgöz, at the Laboratory of Aero & Hydrodynamics, related to the sum of correlation reprocessing, have been instrumental in the improvement of the experimental data quality. The proof reading efforts of Arati Gurung were greatly appreciated.

4.1. INTRODUCTION

The design of a propeller for high efficiency is often constrained by cavitation. As the effects of sheet cavitation are relatively well understood, counter measures against harmful effects of sheet cavitation are taken in the design stage. These involve the smooth transport of vapor into the tip vortex, diverting harmful implosions from the propeller surface. The dynamics of the tip vortex cavity are not directly related to the propeller rotation rate. The excitation of this cavity often leads to high amplitude broadband pressure fluctuations with frequencies between the fourth and seventh blade passing frequency (van Wijngaarden *et al.*, 2005).

To better understand the sound production from vortex cavitation, a model for the waves on a tip vortex cavity was developed, and was shown to be able to describe the interface dynamics in detail (Pennings *et al.*, 2015*a*). As a result, a condition could be predicted for which a cavity resonance frequency might be amplified to produce high amplitude sound, as reported by Maines & Arndt (1997).

The part that remains to be validated is a vortex model for the cavity size and cavity angular velocity. It has been shown that a Lamb-Oseen vortex model poorly represents the cavity size as a function of cavitation number (Pennings *et al.*, 2015*a*). It is possible that overestimation of the peak azimuthal velocity inside the vortex could have lead to an overestimation of the cavity size. The main goal of the present study was to configure a simple low-order vortex model, to serve as an input into a model for the dynamics of vortex cavity waves, to describe the resonance frequency. It is based on the following steps.

1. Model the tip vortex velocity field without cavitation (further referred to as wetted vortex)

2. Model the cavity size as function of cavitation number based on wetted vortex properties

3. Show the difference in velocity field around a wetted and that around a cavitating vortex

4. Obtain the cavity angular velocity that gives the best correlation of the resonance frequency of the tip vortex cavity

To achieve these goals, the velocity field was measured in a tip vortex in direction of the region close to the viscous core, in the presence as well as in absence of cavitation. High-resolution measurements in the wing tip vortices have been performed in numerous other studies. Point-wise Laser Doppler Velocimetry was used in a stationary wing tip vortex, in a chronological order (Higuchi *et al.*, 1987; Arndt *et al.*, 1991; Arndt & Keller, 1992; Fruman *et al.*, 1995; Boulon *et al.*, 1999). Later the same method was used to measure the flow field including the tip vortices trailing a rotating propeller (Felli *et al.*, 2009; Felli & Falchi, 2011; Felli *et al.*, 2011).

Planar Particle Image Velocimetry (PIV) was used for a wing at low Reynolds numbers by Zhang *et al.* (2006) and Lee (2011). At higher (model aircraft) Reynolds numbers, velocity fields in wing tip vortices were measured by Scarano *et al.* (2002). Typical

problems encountered in PIV measurements inside tip vortices were shown at the First International PIV Challenge (Stanislas *et al.*, 2003).

Stereo PIV (SPIV) was applied at low Reynolds numbers of 10^4 by del Pino *et al.* (2011). SPIV measurements of Chang *et al.* (2011) and Dreyer *et al.* (2014), similar to the measurements performed in the present study, focused on the effect of the velocity field on vortex cavitation, but velocities were not measured in the presence of cavitation.

In the present study using SPIV, the size of the interrogation area was limited by the particle seeding density, due to the small field of view around the tip vortex. To accurately determine the velocity field around the viscous core of a tip vortex, a high spatial resolution and a high accuracy with respect to spatial gradients are necessary. This requires much smaller interrogation areas than the typical 32 × 32 pixels arrangement.

A method is proposed for the high resolution measurement of the time-averaged velocity fields around vortex cavitation. First, large interrogation areas were used to identify the vortex center in the instantaneous vector fields. This was necessary due to vortex center wandering. Similar vortex center identification was used by Graftieaux *et al.* (2001); del Pino *et al.* (2011); Bhagwat & Ramasamy (2012) and Dreyer *et al.* (2014). Second, the original PIV images were grouped according to their vortex center position. Third, the images with the same vortex center position were evaluated together, according to the correlation averaging method introduced by Meinhart *et al.* (2000). This increases the correlation quality based on the number of images used, while allowing a smaller size of the interrogation area.

Section 4.2 describes the SPIV setup. This is followed by the details on the SPIV analysis, including the high-resolution time-averaging method. The estimation of the cavity diameter, section 4.3. The four principal parts of the study are evaluated in section 4.4. Finally, the limitations of the models and the conclusions are presented in sections 4.5 and 4.6, respectively.

4.2. EXPERIMENTAL SETUP

The experiments were performed in the cavitation tunnel at the Delft University of Technology. The details of the tunnel can be found in (Foeth, 2008) with the recent modifications described in (Zverkhovskyi, 2014). All measurements in the present study were performed at 6.8 m/s with typical fluctuations of ±0.5%. The cross section of the test section was 0.30 × 0.30 m^2 at the inlet and 0.30 × 0.32 m^2 at the outlet. The vertical direction was extended gradually from inlet to outlet, to compensate for the growth of the boundary layer along the tunnel walls, in order to facilitate a nearly zero-pressure gradient in streamwise direction. A sketch of the setup is given in Fig. 4.1.

A tip vortex is generated by a wing with elliptic planform, with a $NACA\,66_2-415$ cross section, and $a = 0.8$ mean line. The method for modifying the mean line is described in detail by Abbott & von Doenhoff (1959). Due to the manufacturing limitations, the trailing edge was truncated at a thickness of 0.3 mm. This resulted in a chord at the root of the wing of $c_0 = 0.1256\,m$. The half span of 0.150 m positions the tip of the horizontally mounted wing approximately in the center of the test section. The wing was mounted in a six-component force/torque sensor (ATI SI-330-30), in the side window of the test section. At a positive angle of attack, lift points in vertically downward direction.

Primary tunnel parameters were measured during each experiment. A temperature

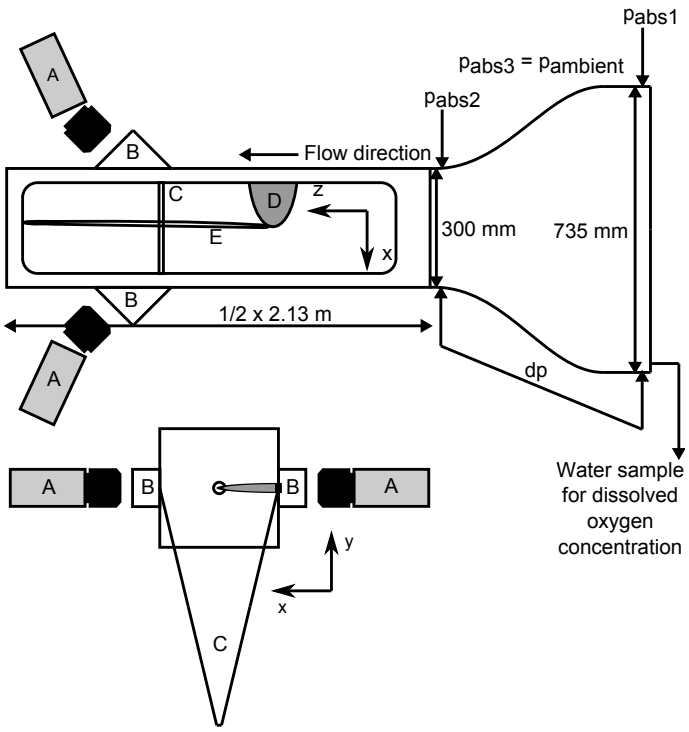

Figure 4.1: Experimental setup in the cavitation tunnel with cameras A, prisms B, laser light sheet C, elliptic planform wing D and tip vortex cavity E. Location of the absolute and differential pressure sensors are given by p_{abs} and dp respectively. For the location of the temperature sensor and further tunnel details see (Foeth, 2008; Zverkhovskyi, 2014). The origin of the coordinate system is at the wing tip. An example of an image of a tip vortex cavity is given in Fig. 4.2.

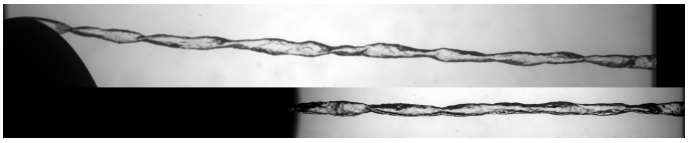

Figure 4.2: Example of high-speed video images reproduced from Pennings *et al.* (2015*a*). Flow is from left to right. In the present study the top and bottom images correspond to the xz-plane and the yz-plane, respectively. The pixel size in the object domain was 16 μm in the xz-plane, and 10 μm in the yx-plane. Black object on the top is the pressure side of the wing. Conditions: lift coefficient $C_L = 0.58$, Reynolds number $Re = 9.1 \times 10^5$ and dissolved oxygen concentration $DO = 2.7\ mg/l$.

sensor (PT-100) was placed submerged in the tunnel water but outside of the main flow at a location downstream of the test section. Static pressure was measured at 10 Hz with a digital sensor measuring the absolute pressure (Keller PAA 33X), at the outlet of the contraction, upstream of the inlet of the test section, at the vertical position of the wing. The typical accuracy is 0.05% of full-scale pressure (3×10^5 Pa), which is 150 Pa. The tunnel free stream velocity, that was also used for the motor control, was based on the pressure drop over the contraction. This is measured with a pressure differential sensor (Validyne DP 15) with a number 36 membrane. The typical accuracy is 0.25% of full-scale pressure (35 kPa), which is 90 Pa. Both pressure sensor values were corrected with a reference measurement, using a Pitot tube at the same location as the wing. All sensors were recorded at a frequency of 10 kHz.

In the case of cavitation, the dissolved gas concentration partly determines the size of the cavity. Dissolved Oxygen (DO) was used here as an representative parameter, determined by using an optical sensor (RDO Pro). Reference measurements were performed with a total dissolved gas sensor. This shows a constant ratio of dissolved oxygen to total dissolved gas. Prior to the experiments, a two-point calibration was performed, using water saturated air (100% saturation), and a fresh sodium sulfite solution (0% saturation). The sensor was placed in a beaker of tunnel water, which was taken at the start and at the end of each series of measurements. The mean of these was used, revealing a small variation of 0.1 mg/l between the start and the end value, after approximately 3 hours of running the tunnel.

Two cameras (LaVision Imager Pro LX 16M) were used, with a 90 degree spread angle, placed in a horizontal plane near the side windows both viewing upstream. The pixel size of the cameras is 7.4 μm, at an image format of 3248 × 4872 pixels. The cameras with 200 mm objectives (1:4 D Nikon ED AF Nikkor) were mounted on a Scheimpflug adapter set at an angle of 20 degrees. There are optical aberrations resulting from the stereo viewing through the acrylic test section windows. To partly compensate for this, a f-stop of $f/32$ was used, for a large depth of focus. Due to limitations in the Scheimpflug angle, the placement of the cameras resulted in a magnification of $M_0 = 0.54$. The pixel size in the object plane was 13.8 μm.

A laser (Spectra-Physics Quanta-Ray PIV-400), at 532 nm and 350 mJ per pulse, was used to generate a light sheet. The estimated thickness is below 1 mm. An exposure-time delay between 14 μs and 6 μs was used, based on the free stream velocity and the proximity to the wing tip. At a repetition rate of 1 Hz, 500 image pairs were taken as the basis for each measurement.

Stereo calibration was performed by placing a glass plate, with a regular dot pattern, perpendicular to the flow in the test section. A micro-traverse was used to displace the grid in streamwise direction resulting in two calibration planes. The test section was accessed by opening the top window, also allowing the target to be submerged during calibration. A calibration was performed after each streamwise plane relocation, and at the start and the end of each day. After calibration, the light sheet was placed at the mid-plane between the calibration planes. This resulted in a very small stereo self-calibration correction.

The flow was seeded with 10 μm hollow glass particles (Sphericells). The density of the particles was close to that of water. Even when considering the maximum rotational

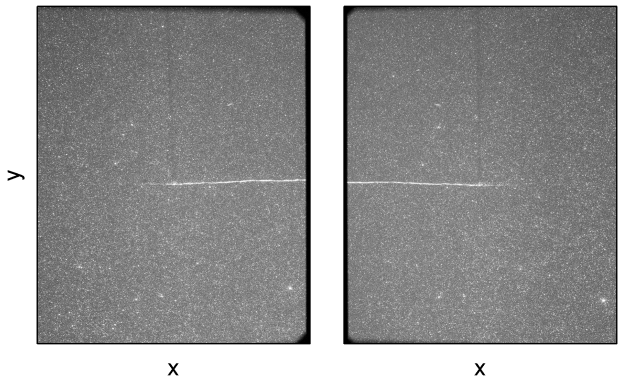

Figure 4.3: Particle images of both cameras. Conditions: $z/c_0 = 1.14$, $C_L = 0.65$, $Re = 8.9 \times 10^5$, $\sigma = 4.2$ and $DO = 2.5\ mg/l$.

frequency of the strongest tip vortex, with a typical azimuthal velocity of 7 m/s at 1 mm from the vortex center, the particles still remained high-fidelity flow tracers (Mei, 1996). This corresponds to 5×10^3 times the gravitational acceleration, which is challenging for a PIV experiment. The particle images were typically more than 4 pixels in size, thereby circumventing the peak-locking problem (Prasad *et al.*, 1992). The vapor core of vortex cavitation was not seeded, and therefore the velocity was measured only outside the tip vortex cavity.

4.3. PARTICLE IMAGES, VECTOR PROCESSING AND HIGH-RESOLUTION TIME-AVERAGING METHOD

An example of particle images, from both the root-side camera (left) and the tip-side camera (right), is given in Fig. 4.3. The lift coefficient C_L is defined as $C_L = F_L/(\frac{1}{2}\rho W_\infty^2 S)$ using the lift force F_L, water density ρ, free stream velocity W_∞ and wing surface area $S = 1.465 \times 10^{-2}\ m^2$. The Reynolds number $Re = W_\infty c_0/\nu$ is based on the free stream velocity W_∞, wing root chord c_0 and kinematic viscosity ν. The cavitation number $\sigma = (p_\infty - p_v)/(\frac{1}{2}\rho W_\infty^2)$ uses the static pressure p_∞ at the test section inlet minus the vapor pressure p_v. At the conditions of Fig. 4.3 with $\sigma = 4.2$, cavitation is normally not expected. However, a clear white line and faint shadow were observed in the top half of the image. The seeding particles act as nucleation sites and promote cavitation inception. The intermittent streak of cavitation in the vortex core was visible as a white line. This was absent at the same conditions without seeding. Since the diameter of the cavity was very small, it is not expected to strongly influence the flow field. However, it does deteriorate the quality of the vectors along this bright white line.

In the case of a large tip vortex cavity, the PIV images look similar to those in Fig. 4.4. The cavity can be distinguished by a bright underside and a distinct vertical shadow. It is clear from these images that no meaningful velocity information can be obtained from the region blocked by the image of the cavity. The particles in the shadow might still be

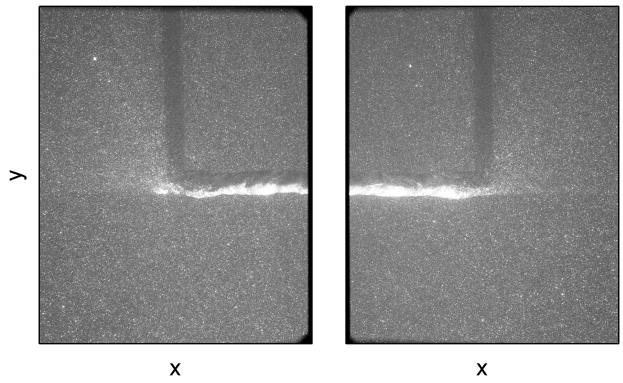

Figure 4.4: Particle images of both cameras. Conditions: $z/c_0 = 1.14$, $C_L = 0.67$, $Re = 9.0 \times 10^5$, $\sigma = 1.1$ and $DO = 2.5\ mg/l$.

useful, though the lower intensity will affect the vector quality at the edges of the shadow.

The light sheet was refracted and reflected on the cavity interface. The reflections were of low enough brightness not to pose a significant risk of damaging the cameras. However, these effects create shadows and local bright regions in the particle images. An alternative would be to use fluorescent tracer particles. This requires a significant increase in the light required to illuminate a moderately sized field of view. The regular tracer particles used in the present study already required the maximum laser pulse energy. The compromise then was to take a 90 degree wedge (shown in Fig. 4.5). Vectors inside the cavity interface were excluded from analysis.

The seeding density is limited by the distance, which is half the tunnel height, that the light sheet has to travel before it illuminates the field of view. Also, particle image pairs are lost due to a large out of plane velocity. These parameters result in instantaneous vector fields of insufficient quality. Since the conditions during the typical 10 minute measurement were stable, the vector fields could be averaged. The result of a simple average is shown in Fig. 4.5. Even under stable conditions, a tip vortex center position in the proximity of the tunnel walls showed displacement or wandering. Fig. 4.5 also shows the result of two stages of improvement. The first stage involved conditional averaging of the position of the vortex center. The vortex center was obtained by summing the absolute values of the vertical and horizontal velocity components, and fitting a parabola through the highest values, to obtain the coordinates of the maximum. In the next stage, these vortex centers were used to reprocess the particle images using sum of correlation (SOC), on images with similar vortex center positions. The details of these approaches are described at the end of this section.

Vector fields were obtained using DaVis 8. The images were preprocessed with a 96 pixel × 96 pixel sliding background filter. A geometric mask was applied to exclude the image edges from vector calculation. Stereo cross correlation was applied using a multi-pass approach with 3 passes on 64 pixel × 64 pixel areas with 50% overlap, and 2 passes on 48 pixel × 48 pixel areas with 50% overlap. This resulted in a vector spacing of 0.3

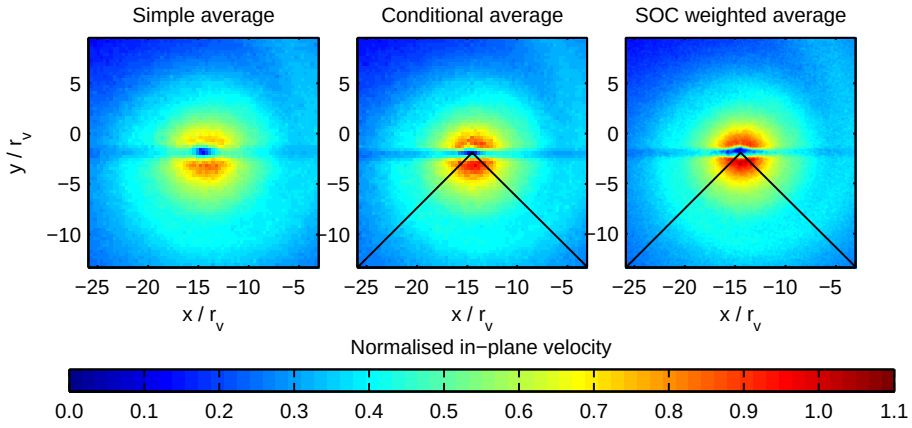

Figure 4.5: Normal time average, conditional vortex centered average and sum of correlation (SOC) conditional weighted average of the in-plane velocity normalised with the free stream velocity $W_\infty = 6.8\ m/s$ and viscous core radius $r_v = 1.1\ mm$. Black lines indicate the 90-degree section of the velocity field, that is later used for the contour average. Conditions: $z/c_0 = 1.14$, $C_L = 0.65$, $Re = 8.9 \times 10^5$, $\sigma = 4.2$ and $DO = 2.6\ mg/l$.

mm. During post-processing, a minimum peak ratio of 1.5 was imposed, and a median test was applied for outlier detection.

The global vortex detection method by Graftieaux *et al.* (2001) and used in Dreyer *et al.* (2014) was also considered. This method is much more robust due to lower susceptibility to noise in the instantaneous vector fields. However, the bright line in the particle images as seen in Fig. 4.3 and Fig. 4.4, resulted in low vector quality. Therefore the method could not determine the horizontal position with sufficient accuracy. Therefore the global vortex detection method could not be used to estimate the horizontal position of the vortex center.

The instantaneous particle images of Fig. 4.4 were therefore used. First, the bright underside of the cavity was detected. This was used as a reference for the vertical position of the center. From this location downward, the horizontal velocity was used. In a similar manner as for non-cavitating cases the horizontal position of the center was thus obtained. The original particle images were shifted to the vortex center and summed. In this summation the vertical shadow was used to obtain the cavity diameter. The result is shown in Fig. 4.6. The condition for the cavity edge was taken to be the location at which the derivative of the intensity is maximum.

In the results section, results of this method are compared to those of the shadowgraphy high-speed video of Pennings *et al.* (2015*a*). An example image of two views is given in Fig. 4.2. The largest variability on the mean cavity diameter corresponds to the amplitude of the stationary wave. This mainly affects cavities with a diameter of several times the wetted viscous core radius.

The vortex center was reliably detected in the instantaneous vector fields. However, a residual vortex motion equal to the vector spacing of 0.3 mm remains. This vector spacing is reasonable for global properties but is insufficient to capture the detailed dynamics near the edge of the viscous vortex core, or in the case of cavitation close to the

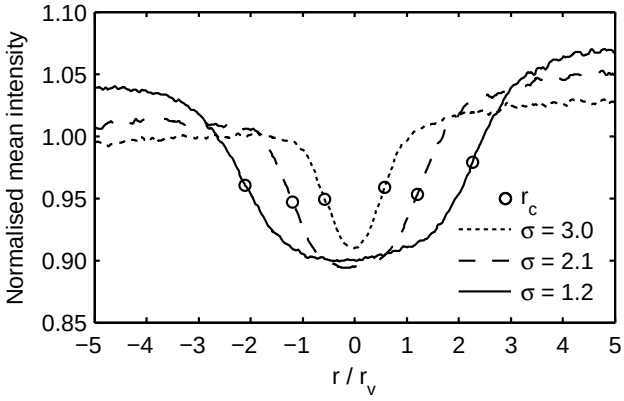

Figure 4.6: Normalised mean intensities of the shadow of the vortex cavity, with the open circles indicating the location of maximum gradient defined as the cavity edge radius r_c, normalised with wetted viscous core radius $r_v = 1.1\ mm$. Conditions: $z/c_0 = 1.14$, $C_L = 0.66$, $Re = 9.1 \times 10^5$ and $DO = 2.5\ mg/l$.

edge of the vapor-filled cavity.

The vector spacing in the present study was limited by the number of well-correlated particle image pairs in an interrogation area. The practical limit of sufficient particle image pairs for each time instance was reached at areas of 48 pixels × 48 pixels.

Once the positions of the vortex center were known, particle images with the vortex at the same location, were selected and processed together. The correlation maps of all the individual instantaneous particle images, at the same position of the vortex center, were summed to obtain a single vector field. This is based on the correlation averaging method by Meinhart *et al.* (2000), referred to here by SOC. In this manner, the number of well-correlated particle image pairs increases with the number of images used. Meinhart *et al.* (2000) also concluded that, the correlation averaging technique results in an improvement of vector correlation quality while allowing reduction in the size of the interrogation area.

For all streamwise locations except $z/c_0 = 5.50$, the size of the interrogation area was reduced to the values in Table 4.1. This shows the minimum area size, to be able to ensure at least 95% good vectors, at the vortex center positions, with the least number of available images. To benefit from this approach, a certain minimum number of images at a single vortex center position is needed. The minimum number of images used in the SOC for each streamwise location is given in Table 4.1. The number of vortex center positions is chosen such that an approximately equal total number of images is used for all cases. At $z/c_0 = 5.50$, the amplitude of the wandering of the vortex center is so large, that this minimum condition could not be met at an improved interrogation area size.

The vector calculation for the SOC approach is also based on multi-pass iterations. First, 3 passes on areas of 32 pixels × 32 pixels using 50% overlap, were followed by 2 passes at the area size given in Table 4.1 also with a 50% overlap. A minimum peak ratio of 1.5 was required for the three passes of a universal-outlier detection with a filter region of 5 vectors × 5 vectors. Empty spaces in the vector field were filled employing

Table 4.1: Properties for SOC processing. Due to insufficient number of images SOC is not applied at z/c_0 = 5.50. The results at that location are based on the conditional average.

z/c_0	0.50	0.74	1.14	1.75	5.50
Minimum # of images per position	38	22	13	8	–
Average # of vortex center positions	5	8	14	22	–
Interrogation area [$pixels$]	6×6	8×8	12×12	24×24	48×48
Vector spacing [μm]	42	55	83	165	332

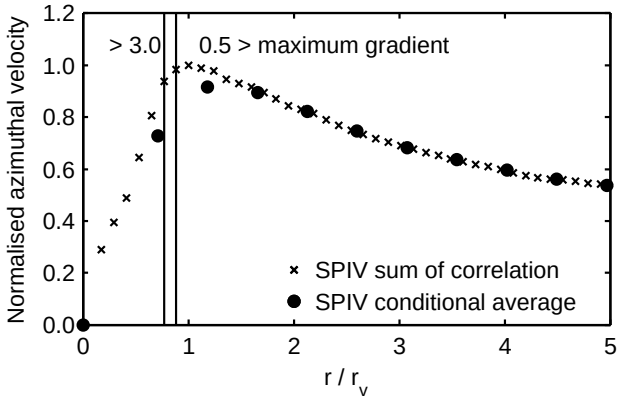

Figure 4.7: Result of SOC method given as contour-averaged data, normalised with the maximum azimuthal velocity $u_\theta = -6.7\ m/s$ and viscous core radius $r_v = 1.1\ mm$. Conditions: $z/c_0 = 1.14$, $C_L = 0.65$, $Re = 8.9\times10^5$, $\sigma = 4.2$ and $DO = 2.5\ mg/l$. The original conditionally averaged data is also given, to show the improvement in the description of the azimuthal velocity around the viscous core. The vertical lines indicate the limits for which the gradient is > 3.0 pixel and < 0.5 pixel per 48 × 48 pixels interrogation area. The region left of the > 3.0 pixel line is not properly resolved by the conditional average data (Westerweel, 2008). The allowable gradient for the SOC data is higher than the measured gradient inside the viscous core.

interpolation.

The result of SOC at the various positions could be considered as new 'instantaneous' vector fields. The new SOC vector fields were then displaced to match the earlier determined vortex center position. The final averaged SOC vector field was obtained by a weighted average based on the number of images used in the individual SOC vector fields. A sample of this approach is given in Fig. 4.7. This results in a dimensional vector spacing as given in Table 4.1, which is 2-8 times smaller than the original size of the interrogation area. The following results are based on vector processing using SOC except for $z/c_0 = 5.50$, for which vortex center conditional averaging was applied.

4.4. RESULTS

The results are presented as follows. A general overview of the properties of a wetted vortex flow field is given in subsection 4.4.1. This includes the residual error of the determination of the motion of the vortex center, the optical aberrations at several streamwise locations and the empirical model fit. In subsection 4.4.2, the wetted flow field is com-

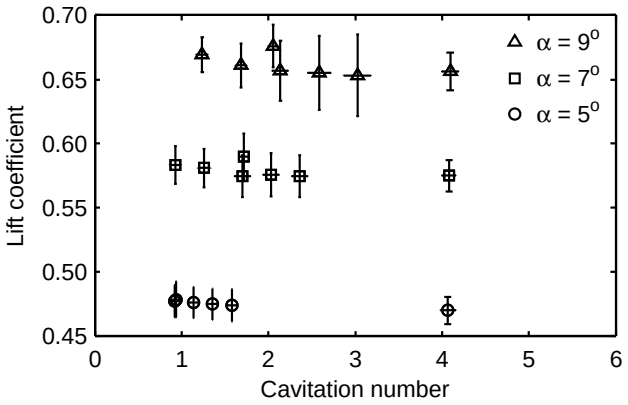

Figure 4.8: Effect of cavitation number on lift coefficient for three angles of attack (α) in degrees. Conditions: $Re = 9 \times 10^5$ and $DO = 2.5\ mg/l$.

pared to the one around the vortex cavity. Finally, in subsection 4.4.3, the obtained cavity angular velocity is used to calculate the resonance frequency of tip vortex cavitation.

4.4.1. FLOW FIELD WETTED VORTEX

The lift coefficient C_L is used throughout this study to indicate the condition for which the measurements were performed. This gives a measure of the strength of the tip vortex. Figure 4.8 shows the relation between the lift coefficient as function of cavitation number for three angles of attack α. At cavitation numbers below 4, a stationary tip vortex cavity was present. The effect of cavitation number on the lift coefficient falls below the amplitude of the signal variability, which is approximately equal to the repeatability error in setting the angle of attack. The drag force was an order of magnitude smaller than the lift force. Since this is not accurately resolved by the force sensor and was not important for the present study, it is not discussed further.

STATISTICS VORTEX WANDERING

The position of the vortex center can be used to describe the characteristics of the motion in two directions. In Fig. 4.9, the symbols are obtained from a histogram of the measured position of the vortex centers, with each bin equal to one vector spacing. The lines are normal distributions, based on the standard deviation of the motion of the vortex center. Figure 4.10 shows the relation between vortex center motion and the streamwise position.

In general, the vortex center motion was larger in the spanwise direction than in the lift direction. The only exception found was at $C_L = 0.66$ for the cross-flow plane at $z/c_0 = 5.50$. Except for this particular case, the amplitude of motion was hardly influenced by the lift coefficient. The amplitude of the motion increased in proportion to downstream distance.

Vector spacing limited the accuracy of determining the position of the vortex center. The residual motion was smeared out in the SOC approach. As studied by Deven-

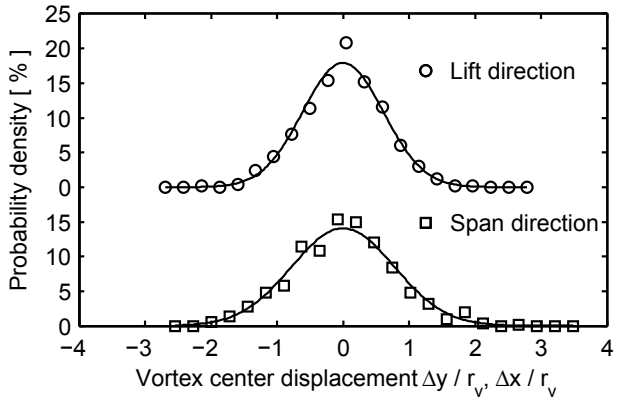

Figure 4.9: Probability density of displacement of the vortex center, normalised with viscous core radius $r_v = 1.2\ mm$. Lines are normal distributions based on standard deviations of location of the vortex center. Conditions: $z/c_0 = 1.75$, $C_L = 0.66$, $Re = 9.1 \times 10^5$, $\sigma = 4.1$ and $DO = 2.6\ mg/l$.

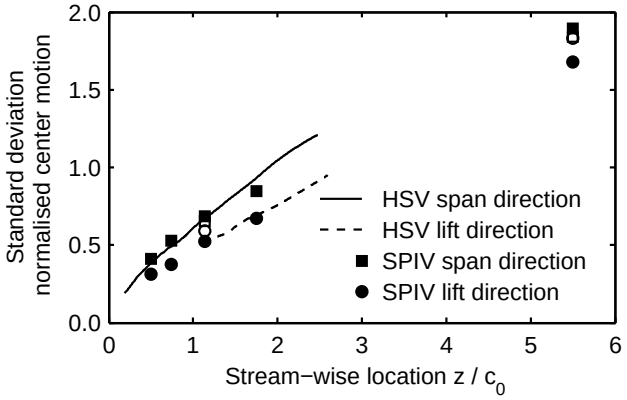

Figure 4.10: Standard deviation of motion of the vortex center, normalised with mean wetted viscous core size $r_v = 1.0\ mm$. The filled symbols are for flow without cavitation. The open symbols are for $\sigma = 1.26$ at $z/c_0 = 1.14$ and $\sigma = 1.72$ at $z/c_0 = 5.50$. The high-speed video (HSV) data is taken from Pennings *et al.* (2015*a*) at $\sigma = 1.20$. Conditions: $C_L = 0.58$, $Re = 9.3 \times 10^5$, $\sigma = 4.1$ and $DO = 2.6\ mg/l$.

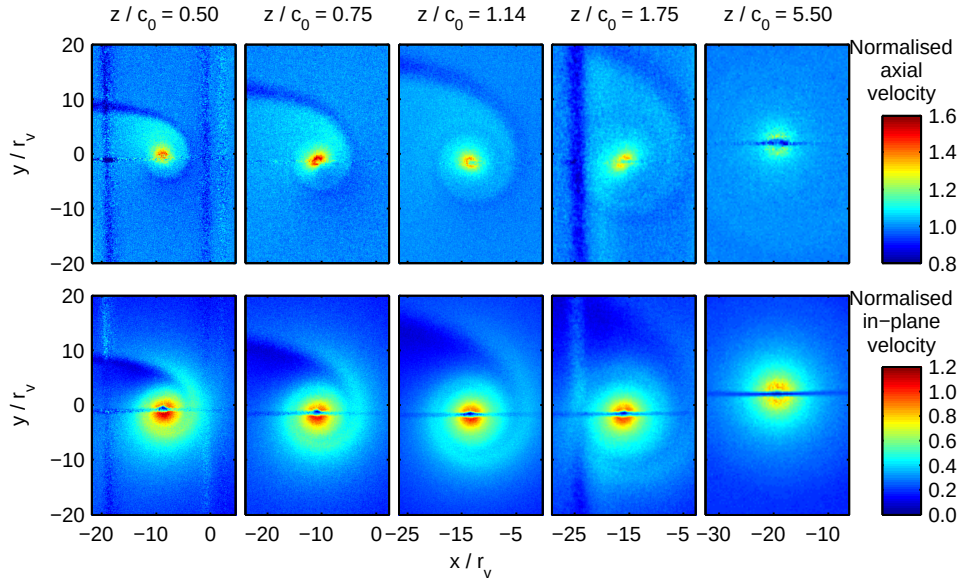

Figure 4.11: Streamwise development of magnitude of axial and in-plane velocity, normalised with free stream velocity $W_\infty = 6.8\ m/s$, coordinates normalised with mean viscous core size $r_v = 1.1\ mm$. Conditions: $C_L = 0.66$, $Re = 9.2 \times 10^5$, $\sigma = 4.1$ and $DO = 2.5\ mg/l$.

port *et al.* (1996) this residual motion was analytically estimated with good accuracy, as found by Bhagwat & Ramasamy (2012). For a laminar q-vortex, as described by Batchelor (1964), the ratio of the real size of the viscous core to the measured size of the viscous core is defined as:

$$\frac{r_{v(real)}}{r_{v(measured)}} = \sqrt{1 - \frac{2as^2}{r^2_{v(measured)}}}, \tag{4.1}$$

where $a = 1.25643$, and s is the residual motion standard deviation of the motion of the vortex center, within one vector spacing of $s = 0.33\ mm$. This value was 0.289 vector spacing for all cases or $0.289 \times 0.33\ mm = 96\ \mu m$. For the measured size of the viscous core $r_{v(measured)}$, the estimates of Fig. 4.13 were used. This caused a maximum overestimation of the size of the viscous core and subsequent underestimation of the peak of the azimuthal velocity of 2% for cross-flow plane at $z/c_0 = 0.50$. Typical residual errors for the other streamwise locations were 1% or lower and were therefore not considered significant.

STREAMWISE DEVELOPMENT

An overview of the development of the streamwise and in-plane velocity is given in Fig. 4.11. The case for $C_L = 0.66$ without cavitation was chosen, because it shows the highest velocities and strongest gradients. The origin of the coordinate system is the upstream wing tip. The horizontal axes in Fig. 4.11 were centered around the center of

the tip vortex. The vortex center is seen to move horizontally towards the root. Some features that reduced the quality of the results are described here.

The horizontal line through the velocity fields is related to the line in Fig. 4.3. At $z/c_0 = 0.50$ and $z/c_0 = 1.75$, vertical lines were also present. This was due to the seal of the water-filled prism. The prism was open on the side mounted to the test section windows. The edges were sealed using an o-ring. The results at five streamwise locations were obtained by moving the entire SPIV system comprised of prisms, cameras and light sheet in streamwise direction. The impression of the seal caused a deformation in the acrylic test section window, which was visible in the particle images and introduced errors in the calculations of the velocity vectors. Due to the order of the measurements, these vertical lines were absent at $z/c_0 = 0.75$, $z/c_0 = 1.14$ and $z/c_0 = 5.50$. These features as shown in Fig. 4.11 reduced the vector quality and limited the useful area for comparison. In case of cavitation, the upper central part was in the cavity shadow and is therefore not useful.

Since the wing was in a pitch-up position, with the suction side at the bottom, the trailing edge was located at positive values of the y-coordinate. The wake of the wing, in the streamwise, i.e. axial velocities, appears as a dark blue spiral. At $z/c_0 = 0.75$ the axial velocities in the vortex core were highest, which imposes a challenge for the SPIV method used here, due to the out of plane loss of particles. This was resolved by choosing a smaller time delay between exposures. This reduced the in-plane particle displacement, which however, reduces the accuracy of the vector calculation. The height of the correlation peak was finally increased by using correlation averaging. The axial velocity obtained from SPIV, at the outer edge of the field of view, was within 1% of the velocity obtained from the drop in pressure over the contraction. Downstream the effect of the roll-up of the wing wake reduces this excess of axial velocity.

A reference part of the plane was chosen as a wedge from the vortex center downward defined by a 90 degree angle. This wedge captures the region of the cross-flow plane with the highest velocities and is not hindered by the detrimental features such as the cavity shadow, cavity reflections and the deformation of the windows of the tunnel due to the prisms. An example of this region is presented in Fig. 4.5. In the case of the vertical distortions, the extent in x-direction of the wedge was limited. Using the identified vortex center, a polar coordinate system was used and the data was averaged over contours at constant radius.

PARAMETER ESTIMATION EMPIRICAL VORTEX MODEL

Most common viscous axisymmetric vortex models are collectively described by Wu *et al.* (2006). These include models such as the simple Rankine vortex, the families of Gaussian vortex models such as the Lamb-Oseen, Burgers and Batchelor (1964) vortex models or the empirical Burnham & Hallock (1982) vortex model. For these models two parameters are sufficient to describe the velocity field. These are usually the viscous core radius r_v and the vortex circulation Γ. In all of the above-mentioned models, the vorticity was strongly concentrated close to the vortex center. As can be seen in Fig. 4.11, the wake of the wing is still in the process of roll-up into the tip vortex and includes the wake of the wing boundary layer. The combination of a small viscous core, a reduced peak azimuthal velocity due to the wake, and a larger spread of the vorticity distribution, deems all of the above mentioned models unsuitable for fitting to the data of the present study.

The Winckelmans (Gerz *et al.*, 2005) model and the Proctor (1998) model are two closely related empirical vortex models, that include extra parameters to better match the contour-averaged data of the distribution of the azimuthal velocity.

The Winckelmans vortex model was used to obtain a complete description of the measurement data, using a large number of fit parameters. The Winckelmans model is the same as the Proctor model for $r > 1.15\,r_v$. Both models failed to accurately describe the size of the cavity within the wetted viscous core. The small size of the viscous core presented a model-scale issue and was not relevant for the resonance frequency of the vortex cavity on full-scale propellers. Therefore, inclusion of only the part of the distribution outside the wetted viscous core in the Proctor model, reduced the number of parameters.

In the vortex model of Winckelmans the azimuthal velocity u_θ is defined as:

$$u_\theta = \frac{\Gamma}{2\pi r}\left(1 - exp\left(\frac{-\beta_i\left(\frac{r}{B}\right)^2}{\left(1+\left(\frac{\beta_i}{\beta_o}\left(\frac{r}{B}\right)^{5/4}\right)^p\right)^{1/p}}\right)\right), \tag{4.2}$$

where Γ is the circulation. The value that gave a good description of the flow field was defined as $\Gamma = \frac{1}{2}c_0 C_L W_\infty \pi/4$. The total wing span B was 0.30 m. Three free parameters remain to be fitted to the experimental data. The outer scale β_o can account for the vortex roll-up and inclusion of the wing wake in the outer part of the vortex flow. The inner scale β_i sets the approximate relation for the viscous core as $r_v/B \approx (\beta_o/\beta_i)^{4/5}$. The value for p was used to match the peak velocity at the radius of the viscous core. The Winckelmans model was not intended for the description of the flow with vortex cavitation, but it appears quite capable to do so. The result of the model fit to the experimental data is given in Fig. 4.12.

All parameters revealed large changes in the velocity field close to the wing tip. The Winckelmans model is intended for well-developed airplane wing tip vortices. The variability of the parameter p might be an indication that the model is used outside the range of validity of the model. All values above 4 indicate much higher peak velocities than commonly found in the airplane wing tip vortices. This also applies to the high values found for β_i. The β_o value is strongly related to the azimuthal velocity close to the vortex core, and is most dependent on the lift coefficient. The roll-up of the tip vortex is related to the loading distribution on the wing. Higher lift coefficients have a larger gradient in loading close to the tip. This results in a faster roll-up and higher β_o value.

The Winckelmans vortex model fit gives an accurate estimation of the size of the viscous core of the vortex, which is the radial location of maximum azimuthal velocity. The development of the size of the viscous core for streamwise location and lift coefficient is given in Fig. 4.13. Here the core size is made dimensionless using an equivalent turbulent boundary layer thickness taken from Astolfi *et al.* (1999) as $\delta = 0.37 c_0 Re^{-0.2}$.

The values of r_v/δ in the present study, are significantly smaller than those reported by Astolfi *et al.* (1999). They found, between streamwise locations $z/c_0 = 0.5$ to 1.0, values between $r_v/\delta = 0.8$ and 1.1. These could be due to very high spatial resolution, small measurement volume, accurate vortex wandering removal due to SOC-weighted conditional-averaging and a cross sectional wing geometry designed for a large extent of the laminar boundary layer.

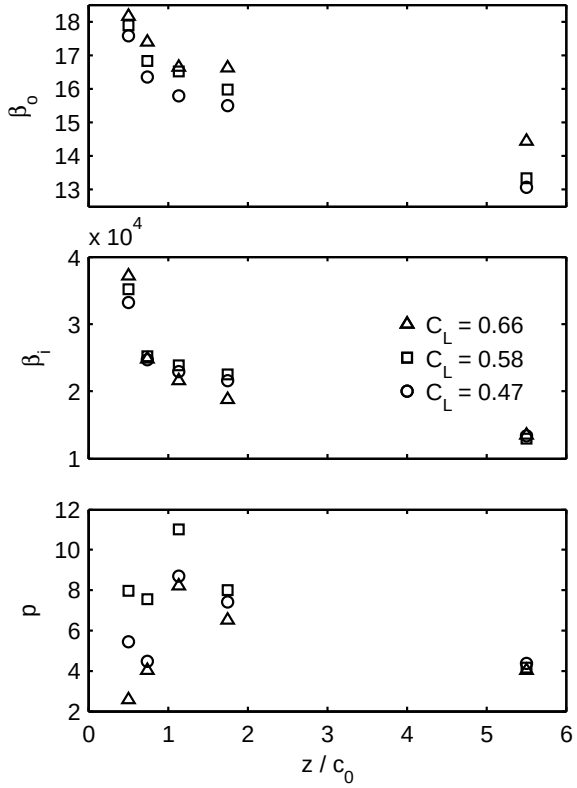

Figure 4.12: Parameters of Winckelmans' vortex model fit to contour-averaged data of the distribution of azimuthal velocity at conditions: $Re = 9.3 \times 10^5$, $\sigma = 4.1$ and $DO = 2.5\ mg/l$

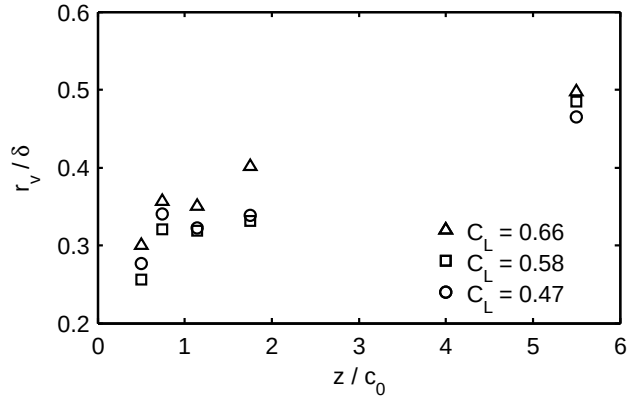

Figure 4.13: Dimensionless viscous core size obtained from location of maximum azimuthal velocity of Winckelmans vortex model fit of Fig. 4.12

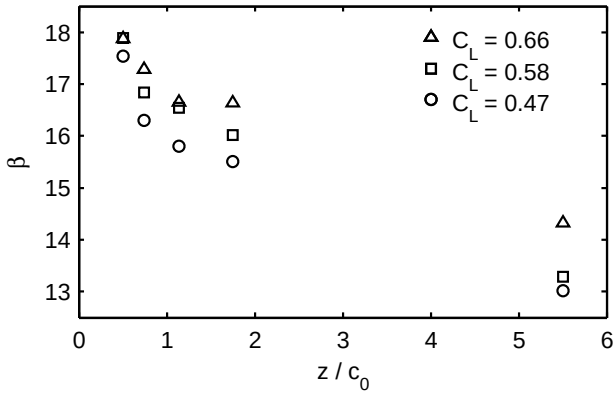

Figure 4.14: Parameter of Proctor vortex model fit to contour-averaged data at conditions: $Re = 9.3\times10^5$, $\sigma = 4.1$ and $DO = 2.5\ mg/l$

The results of r_v was used to select part of the flow that is outside the vortex core, i.e. $r \geq 1.15\, r_v$. This part was fitted using the simpler adapted Proctor (1998) vortex model. The azimuthal velocity u_θ is defined as:

$$u_\theta(r) = \frac{\Gamma}{2\pi r}\left(1 - exp\left(-\beta\left(\frac{r}{B}\right)^{0.75}\right)\right), \tag{4.3}$$

where the parameters Γ and B are equal to value of the corresponding parameters in the Winckelmans vortex model. The value for β could be taken equal to β_o, but for consistency the model is fitted directly to the experimental data. As the Winckelmans vortex model is intentionally similar to the Proctor model, outside the vortex viscous core, the values for β and β_o were found to be close. As an engineering model the Proctor model is preferred, as it needs only one fitting parameter and requires no prior knowledge of the viscous core size. The fit values of the Proctor vortex model are given in Fig. 4.14.

The Proctor vortex model is used to estimate the cavity size in the case of cavitation. Assuming axisymmetry and zero radial velocity, the equation for the conservation of radial momentum simplifies to:

$$\frac{dp}{dr} = \rho\frac{u_\theta^2}{r}. \tag{4.4}$$

At the tunnel wall, approximately 0.15 m from the vortex center, the pressure was assumed to be the free stream static pressure p_∞. By numerical integration of Eqn. 4.4 from the tunnel wall to the vortex center, the pressure distribution as function of the radius was obtained. The cavity radius is defined as the location at which the cavitation number is equal to minus the pressure coefficient $\sigma = -\left(p - p_\infty\right) / \left(\frac{1}{2}\rho W_\infty^2\right)$.

4.4.2. COMPARISON BETWEEN WETTED AND CAVITATING VORTEX

The measurement of the size of the vortex cavity was obtained using two methods. The first method was based on the maximum gradient of cavity shadow in the light sheet

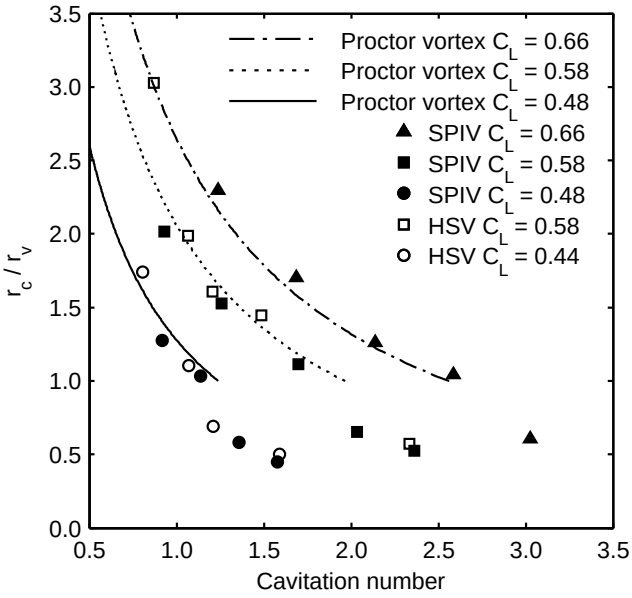

Figure 4.15: Cavity radius normalised with viscous core radius for wetted flow, $r_v = 1\ mm$, as determined from SPIV image shadow, compared with HSV data from Pennings *et al.* (2015*a*). Conditions: $z/c_0 = 1.14$, $Re = 9.2 \times 10^5$ and $DO = 2.5\ mg/l$. Proctor vortex model based on values from Fig. 4.14, which is specifically restricted to the region outside the viscous core to reduce the number of model parameters. The break in the experimental cavity size trend, inside the viscous core, is poorly described by either empirical vortex model.

shown in Fig. 4.6. The second method was the Proctor vortex model fit and Eqn. 4.4, to determine the location where the pressure equals the vapor pressure and thus the cavity radius. In Fig. 4.15 the cavity size based on these methods were compared to the previously obtained cavity size based on high speed video recordings.

The results of both these methods showed similar trends. There was a good agreement between the SPIV and HSV data. This verified the combined steps, of vortex center localisation and the use of the maximum intensity gradient in the shadow, for the estimation of the cavity diameter. The vapour-liquid interface in all following results were based on this post-processing method.

The fit based on the Proctor vortex model gave a good result up to values of r_c equal to r_v, the viscous core for wetted flow. The vortex model of Winckelmans, describes the distribution of the azimuthal velocity inside the vortex core well, but overestimated the cavity size in case $r_c < r_v$, i.e. in case the cavity size is smaller than the viscous core size.

With the cavity size known for all cases, the velocity field outside the cavity was compared to the velocity distribution of a wetted vortex, see Fig. 4.16 and Fig. 4.17. The lowest three cavitation numbers considered show varying cavity sizes. The standard deviation was given by vertical bars. The standard deviation of cavity diameter was given horizontally at the cavity interface radius.

All the cases with a vapor cavity core showed a region of significantly lower azimuthal

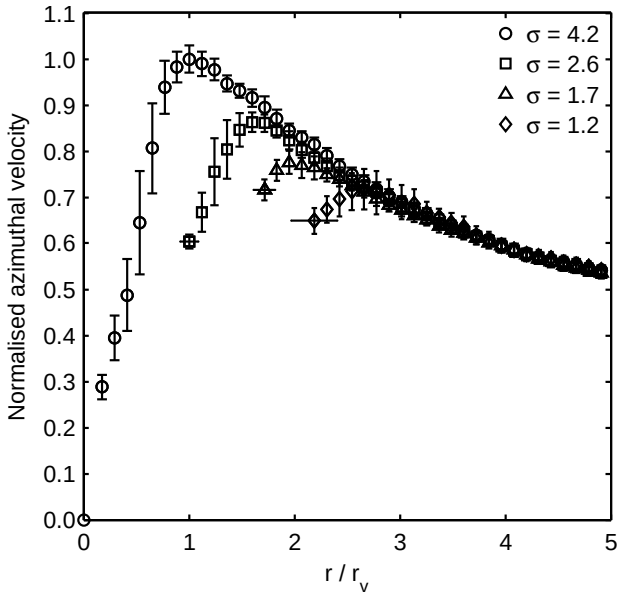

Figure 4.16: Comparison between the distribution of azimuthal velocity of wetted and cavitating vortex from SPIV, normalised with the maximum azimuthal velocity $u_\theta = -6.7\ m/s$ in wetted flow. The radius is normalised with the viscous core radius $r_v = 1.1\ mm$ for wetted flow. Conditions: $z/c_0 = 1.14$, $C_L = 0.66$, $Re = 9.0 \times 10^5$ and $DO = 2.5\ mg/l$.

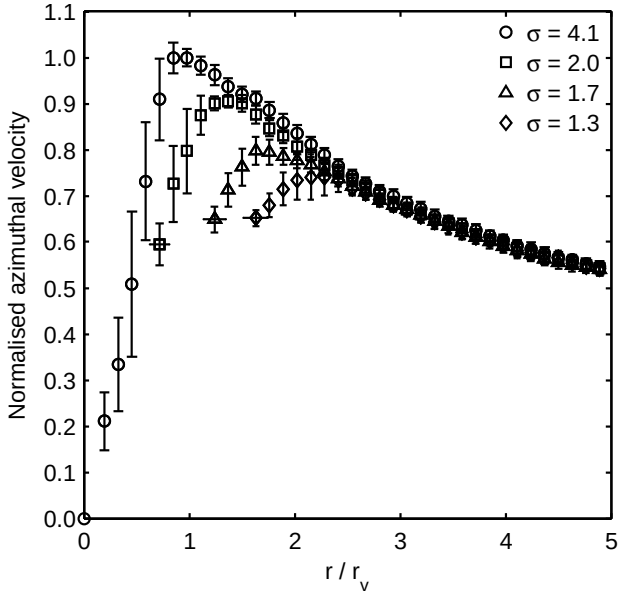

Figure 4.17: Comparison between wetted and cavitating vortex SPIV contour-averaged azimuthal velocity, normalised with the maximum wetted azimuthal velocity $u_\theta = -6.1\ m/s$. The radius is normalised with the wetted viscous core radius $r_v = 1.0\ mm$. Conditions: $z/c_0 = 1.14$, $C_L = 0.58$, $Re = 9.3 \times 10^5$ and $DO = 2.6\ mg/l$.

velocity with respect to the flow field without cavitation. Analogous to a viscous vortex core without cavitation, the velocity gradient in the layer close to the cavity interface resembles a solid body rotation. For cavities with $r_c > 3\,r_v$, the azimuthal velocity field was approximately equal to the wetted flow field.

4.4.3. TIP-VORTEX CAVITY-RESONANCE FREQUENCY

The analysis of HSV data, as shown in Fig. 4.2, in the wave number and frequency domain resulted in clear dispersion relations corresponding to waves travelling on the interface of the vortex cavity (Pennings *et al.*, 2015*a*). The dispersion relations of the three dominant deformation modes were described by a model based on a two-dimensional potential flow vortex in uniform axial flow. It was shown to be valid for a viscous vortex to first-order approximation. The model requires four input parameters: the speed of sound in water, the axial flow velocity, the cavity radius and the cavity angular velocity. The cavity angular velocity, which was the only unknown parameter in that study, was obtained by matching the model dispersion relations to experimental results.

Tip-vortex cavity-resonance frequencies were found directly from the oscillations of the cavity diameter in the frequency domain. These frequencies are accurately described by a zero group velocity condition on the dispersion relation of the $n = 0^-$, volume variation mode. Using the cavity angular velocity, found from the match of the model dispersion relations to the experiment, these frequencies are accurately described by the model. The measurements of the velocity distribution around the vortex cavity provide the opportunity to verify the validity model for the dynamics of the waves on the cavity surface, via direct measurement of the cavity angular velocity.

The azimuthal velocity at the cavity interface in Fig. 4.16 and 4.17 was normalised with the wetted azimuthal velocity at equal radius in non-cavitating flow. The results are presented in Fig. 4.18. As reference, the values of the cavity angular velocity obtained from the model fit of Pennings *et al.* (2015*a*) are included.

As already observed in Fig. 4.16 and 4.17, the values from SPIV were lower than the ones for the non-cavitating vortex. Strong correlation was found between the results from high-speed video and the vortex velocity field for non-cavitating flow. Its implication can be better appreciated by using the derived values to calculate the resonance frequency of the tip vortex cavity, see Fig. 4.19.

The open symbols are resonance frequencies directly obtained from HSV without any intermediate model. The solid symbols are based on direct measurement of the cavity angular velocity in the present study. Clearly the model for the resonance frequency of the tip vortex cavity is physically not correct. Based on the high correlation of the results from the HSV to the non-cavitating vortex reference in Fig. 4.18, a practical alternative was proposed. The cavity angular velocity was replaced by the angular velocity of the non-cavitating vortex at a radius equal to the cavity radius. Although this approach does not have a physical basis, it does give an accurate description of the resonance frequency of the tip vortex cavity. It could be applied to any loading distribution, by using the appropriate circulation Γ and roll-up parameter β.

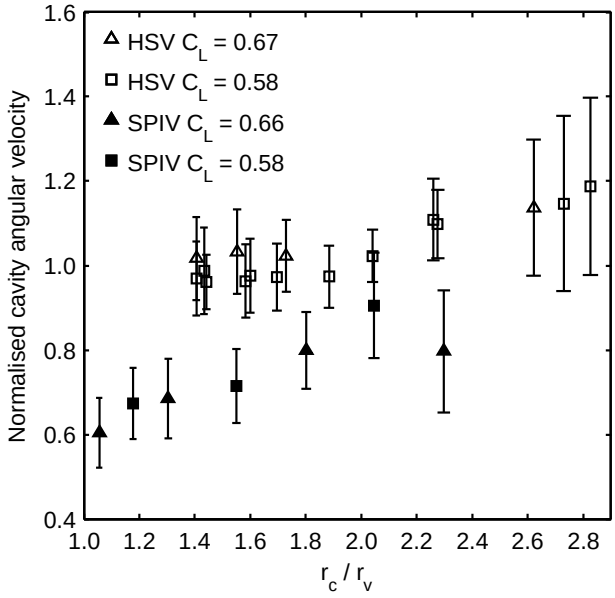

Figure 4.18: Cavity angular velocity as function of cavity radius, normalised with radius of viscous core for non-cavitating flow from SPIV measurements at $z/c_0 = 1.14$, $r_v = 1\ mm$. Solid symbols are obtained directly from data of cases with vortex cavitation in Fig. 4.16 and 4.17 at the cavity edge. Open symbols are based on model fit values from Pennings *et al.* (2015*a*). Range of cavitation number $\sigma = 2.8 - 0.9$.

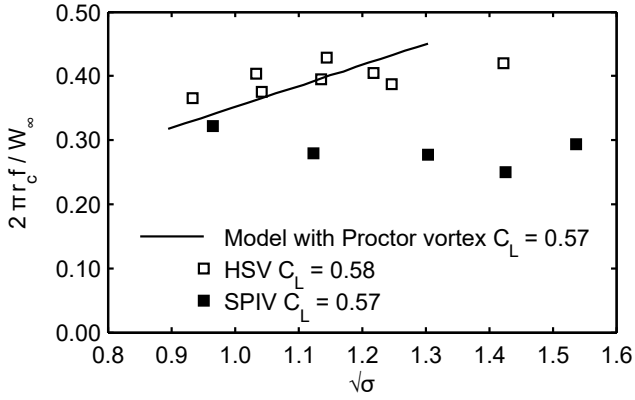

Figure 4.19: Non-dimensional cavity resonance frequency as function of square root of cavitation number. HSV resonance frequencies directly obtained from measurement. SPIV resonance frequencies based on resonance frequency model using measured cavity radius and cavity angular velocity. Wetted Proctor model based on resonance frequency model using wetted angular velocity at cavity radius as model input for the cavity angular velocity. Proctor model parameters: $\Gamma = 0.18\ m^2/s$, $\beta = 16$ and $B = 0.3\ m$. HSV results and model from Pennings *et al.* (2015*a*).

4.5. DISCUSSION

A 90 degree sector of the flow field was taken as representative for the description of the tip vortex. Due to the obstructions in the image, no accurate comparison could be made to the contour average based on the full field of view. Care should be taken when comparing the findings from the present study to other results.

The vector quality in the part of the sector that is closest to the center, was affected by the presence of the cavity interface. Variations in cavity diameter caused some of the interrogation areas to be inside the cavity. The resulting poor contribution to the correlation is expected to be less significant because of the use of correlation averaging. The interrogation areas outside the cavity will result in a higher correlation peak and contribute more to the final vector. In any case the interrogation areas outside the bounds of the variation of cavity diameter in Fig. 4.16 and 4.17, should not be affected.

Several speculations exist on the nature of the flow field surrounding a vortex cavity. Bosschers (2015) has derived an analytical formulation for the distribution of the azimuthal velocity around a two dimensional viscous cavitating vortex. The result is referred to as a cavitating Lamb-Oseen vortex. This distribution was derived using the appropriate jump relations for the stresses at the cavity interface. The shear stress at the vapor-liquid interface is approximately zero. The resulting zero shear stress condition creates a small region in the velocity distribution resembling a solid body rotation, as was found in the present experimental results of Fig. 4.16 and 4.17.

Alternatively, formulations based on a Gaussian distribution were proposed by Choi & Ceccio (2007) and Choi *et al.* (2009). These distributions differed from the previous formulation with an additional parameter describing the azimuthal velocity at the cavity interface. A range of interfacial azimuthal velocities from 0 to the velocity of a non-cavitating vortex was possible.

The behaviour of the model by Bosschers (2015) is very similar to that of the present measurements. However, the non-cavitating Lamb-Oseen vortex, which made an analytical treatment possible, poorly describes the non-cavitating vortex. It is therefore also incapable of quantitatively describing the velocity field around the vortex cavity. A detailed model of the flow field around vortex cavitation should be based on more realistic vortex models. Unfortunately an analytic treatment is then most likely no longer possible.

The same comments apply to the potential flow vortex, that is the basis of the model for the resonance frequency of a tip vortex cavity (Pennings *et al.*, 2015*a*). The origin of the resonance frequency could not have been explained analytically without a formulation based on a potential flow vortex. The quantitative usefulness of the model for the resonance frequency, including the corrected wetted flow input, should further be evaluated on real propeller flows in practice.

4.6. CONCLUSION

A method, based on the identification of the vortex center and correlation averaging, was successfully applied to stereo particle image velocimetry around a wing tip vortex for cavitating and for non-cavitating flow. This procedure provided results with sufficient resolution and accuracy for use in the following detailed observations.

The model based on the Proctor vortex, for the region outside the viscous core, is a good general description of a wing tip vortex close to the tip. It only relies on the empirical parameter β that depends on the wing loading distribution and the streamwise distance from the wing tip. It can also describe the cavity size as function of the cavitation number.

A general trend is found for the effect of cavitation on the velocity distribution in the tip vortex. The cavity interface is surrounded by a region of retarded azimuthal velocity. The velocity distribution close to the interface approximates that of a solid body rotation. Bosschers (2015) analytically derived the region of solid body rotation from the zero shear stress condition at the cavity interface. The region of retarded flow decreases in size for larger cavities until the flow field is equal to that of a non-cavitating vortex.

The tip-vortex resonance-frequencies found by Pennings *et al.* (2015*a*) could be described, by using the angular velocities of a non-cavitating vortex at the cavity radius as a model input for the cavity angular velocity. This approximation of the velocity distribution shows the limits of the approach based on the potential flow vortex.

REFERENCES

ABBOTT, I.H. & VON DOENHOFF, A.E. 1959 *Theory of Wing Sections*. Dover Publications.

ARNDT, R.E.A., ARAKERI, V.H. & HIGUCHI, H. 1991 Some observations of tip-vortex cavitation. *Journal of Fluid Mechanics* **229**, 269–289.

ARNDT, R.E.A. & KELLER, A.P. 1992 Water Quality Effects on Cavitation Inception in a Trailing Vortex. *Journal of Fluids Engineering* **114**, 430–438.

ASTOLFI, J.-A., FRUMAN, D.H. & BILLARD, J.-Y. 1999 A Model for Tip Vortex Roll-up in the Near Field Region of Three-Dimensional Foils and the Prediction of Cavitation Onset. *European Journal of Mechanics - B/Fluids* **18** (4), 757–775.

BATCHELOR, G.K. 1964 Axial Flow in Trailing Line Vortices. *Journal of Fluid Mechanics* **20**, 645–658.

BHAGWAT, MAHENDRA J. & RAMASAMY, MANIKANDAN 2012 Effect of tip vortex aperiodicity on measurement uncertainty. *Experiments in Fluids* **53**, 1191–1202.

BOSSCHERS, J. 2015 An Analytical Solution for the Viscous Flow around a 2-D Cavitating Vortex. *Submitted to Journal of Fluids Engineering* .

BOULON, OLIVIER, CALLENAERE, MATHIEU, FRANC, JEAN-PIERRE & MICHEL, JEAN-MARIE 1999 An Experimental Insight into the effect of Confinement on Tip Vortex Cavitation of an Elliptical Hydrofoil. *Journal of Fluid Mechanics* **390**, 1–23.

BURNHAM, D.C. & HALLOCK, J.N. 1982 Chicago Monostatic Acoustic Vortex Sensing System. *Tech. Rep.* DOT-TSC-FAA-79-18, IV. U.S. Department of Transportation.

CHANG, NATASHA, GANESH, HARISH, YAKUSHIJI, RYO & CECCIO, STEVEN L. 2011 Tip Vortex Cavitation Suppression by Active Mass Injection. *Journal of Fluids Engineering* **133**.

CHOI, JAEHYUG & CECCIO, STEVEN L. 2007 Dynamics and Noise Emission of Vortex Cavitation Bubbles. *Journal of Fluid Mechanics* **575**, 1–26.

CHOI, JAEHYUG, HSIAO, CHAO-TSUNG, CHAHINE, GEORGES & CECCIO, STEVEN 2009 Growth, Oscillation and Collapse of Vortex Cavitation Bubbles. *Journal of Fluid Mechanics* **624**, 255–279.

DEL PINO, C., PARRAS, L., FELLI, M. & FERNANDEZ-FERIA, R. 2011 Structure of trailing vortices: Comparison between particle image velocimetry measurements and theoretical models. *Physics of Fluids* **23**.

DEVENPORT, W.J., RIFE, M.C., LIAPIS, S.I. & FOLLIN, G.J. 1996 The structure and development of a wing-tip vortex. *Journal of Fluid Mechanics* **312**, 67–106.

DREYER, MATTHIEU, DECAIX, JEAN, MÜNCH-ALLIGNÉ, CÉCILE & FARHAT, MOHAMED 2014 Mind the gap: a new insight into the tip leakage vortex using stereo-PIV. *Experiments in Fluids* **55**.

FELLI, M., CAMUSSI, R. & DI FELICE, F. 2011 Mechanisms of Evolution of the Propeller Wake in the Transition and Far Fields. *Journal of Fluid Mechanics* **682**, 5–53.

FELLI, MARIO & FALCHI, MASSIMO 2011 Propeller Tip and Hub Vortex Dynamics in the Interaction with a Rudder. *Experiments in Fluids* **51**, 1385–1402.

FELLI, MARIO, ROBERTO, CAMUSSI & GUJ, GIULIO 2009 Experimental analysis of the flow field aroud a propeller-rudder configuration. *Experiments in Fluids* **46**, 147–164.

FOETH, EVERT-JAN 2008 The Structure of Three-Dimensional Sheet Cavitation. PhD thesis, Delft University of Technology, Delft, The Netherlands.

FRUMAN, D.H., CERRUTTI, P., PICHON, T. & DUPONT, P. 1995 Effect of Hydrofoil Planform on Tip Vortex Roll-Up and Cavitation. *Journal of Fluids Engineering* **117**, 162–169.

GERZ, THOMAS, HOLZÄPFEL, FRANK, BRYANT, WAYNE, KÖPP, FRIEDRICH, FRECH, MICHAEL, TAFFERNER, ARNOLD & WINCKELMANS, GRÉGOIRE 2005 Research towards a wake-vortex advisory system for optimal aircraft spacing. *Comptes Rendus Physique* **6**, 501–523.

GRAFTIEAUX, LAURENT, MICHARD, MARC & GROSJEAN, NATHALIE 2001 Combining PIV, POD and vortex identification algorithms for the study of unsteady turbulent swirling flows. *Measurement Science and Technology* **12**, 1422–1429.

HIGUCHI, H., QUADRELLI, J.C. & FARELL, C. 1987 Vortex Roll-Up from an Elliptic Wing at Moderately Low Reynolds Numbers. *AIAA Journal* **25** (12), 1537–1542.

LEE, T. 2011 PIV study of near-field tip vortex behind perforated Gurney flaps. *Experiments in Fluids* **50**, 351–361.

MAINES, B. & ARNDT, R.E.A. 1997 The Case of the Singing Vortex. *Journal of Fluids Engineering* **119**, 271–276.

MEI, R. 1996 Velocity fidelity of flow tracer particles. *Experiments in Fluids* **22**, 1–13.

MEINHART, CARL D., WERELEY, STEVE T. & SANTIAGO, JUAN G. 2000 A PIV Algorithm for Estimating Time-Averaged Velocity Fields. *Journal of Fluids Engineering* **122**, 285–289.

PENNINGS, P.C., BOSSCHERS, J., WESTERWEEL, J. & VAN TERWISGA, T.J.C. 2015*a* Dynamics of isolated vortex cavitation. *Journal of Fluid Mechanics* **778**, 288–313.

PENNINGS, P.C., WESTERWEEL, J. & VAN TERWISGA, T.J.C. 2015*b* Flow field measurement around vortex cavitation. *Experiments in Fluids* **56**.

PRASAD, A.K., ADRIAN, R.J., LANDRETH, C.C. & OFFUTT, P.W. 1992 Effect of resolution on the speed and accuracy of particle image velocimetry interrogation. *Experiments in Fluids* **13**, 105–116.

PROCTOR, F.H. 1998 The NASA-Langley Wake Vortex Modelling Effort in Support of an Operational Aircraft Spacing System. In *Proceedings of the 36th Aerospace Sciences Meeting & Exhibit*. AIAA, Reno, Nevada, USA.

SCARANO, F., VAN WIJK, C. & VELDHUIS, L.L.M. 2002 Traversing field of view and AR-PIV for mid-field wake vortex investigation in a towing tank. *Experiments in Fluids* **33**, 950–961.

STANISLAS, M., OKAMOTO, K. & KÄHLER, C. 2003 Main Results of the First International PIV Challenge. *Measurement Science and Technology* **14**, R63–R89.

VAN WIJNGAARDEN, ERIK, BOSSCHERS, JOHAN & KUIPER, GERT 2005 Aspects of the Cavitating Propeller Tip Vortex as a Source of Inboard Noise and Vibration. In *Proceedings of the ASME Fluids Engineering Division Summer Meeting and Exhibition*. Houston, Texas, USA.

WESTERWEEL, J. 2008 On velocity gradients in PIV interrogation. *Experiments in Fluids* **44**, 831–842.

WU, J.-Z., MA, H.-Y. & ZHOU, M.-D. 2006 *Vorticity and Vortex Dynamics*. Springer.

ZHANG, H.J., ZHOU, Y. & WHITELAW, J.H. 2006 Near-Field Wing-Tip Vortices and Exponential Vortex Solution. *Journal of Aircraft* **43** (2), 445–449.

ZVERKHOVSKYI, OLEKSANDR 2014 Ship Drag Reduction by Air Cavities. PhD thesis, Delft University of Technology, Delft, The Netherlands.

5

CONCLUSION

Experimental findings support the theory outlined by Bosschers (2009) for the description of broadband pressure fluctuations due to vortex cavitation. These show the origin of the center frequency of the hump in the power spectral density as function of frequency of propeller pressure fluctuations. Broadband pressure fluctuations are the result of the excitation of a long streamwise stretch of the tip vortex cavity by an implosion at the relevant frequency of the tip sheet cavity or another part of the tip vortex cavity. The frequencies of the broadband sound are thus determined by the properties of the tip vortex outside the cavity implosion region. The analysis of the frequency band and amplitude of the hump in the distribution of the power spectral density were outside the scope of the current study. The frequency band is affected by amplitude and phase modulation as stated by Bosschers (2009). The amplitude is expected to be related to the match of the excitation frequency and the resonance frequency of the tip vortex cavity. The novel results of the pursued study are indicating that:

- For a model-scale propeller a relation is demonstrated between the oscillations of the tip-vortex cavity-diameter and the dominant radiated-sound frequency (chapter 2)
- Dispersion relations between the frequency and wave number of waves, on the vapour-liquid interface of a tip-vortex cavity, are identified for three deformation modes (chapter 3)
- The group velocity of the volume variation mode is found experimentally as a criterion for the occurrence of a resonance frequency of the cavity (chapter 3)
- A region of retarded azimuthal velocity surrounds the vapour cavity in a tip vortex, giving a velocity distribution similar to that of a viscous core of a non-cavitating vortex (chapter 4)

There are two relevant conditions for these findings to be true. The first condition is that there is a sufficiently long stretch of the tip vortex cavity. However, there is not

yet a clear criterion of the minimum length required. In the present study this was clearly satisfied, as the tip vortex cavity persisted for at least a few propeller diameters in downstream direction. The second condition is the existence of a sufficient excitation in the flow to provide energy to the oscillation of the tip-vortex cavity-diameter (see section 2.4.3 of chapter 2). Energy from the implosion should be transferred to the tip-vortex cavity at the right frequency. The match between the implosion frequency and the frequency of the tip-vortex cavity-resonance affects the amplitude of the sound. As a cavity implosion contains a large range of frequencies it is expected that these conditions are present for most ships in varying intensity.

A proper physical understanding of a potential source of the broadband pressure fluctuations is the most important contribution in the analysis of industrial applications. This understanding could result in the decision to limit the excitation in order to prevent sound production or to estimate the amount of sound produced. The resonance frequency of a propeller tip-vortex cavity can be estimated with the model developed in the present study (see section 2.2 of chapter 2).

To design better propellers we still require two important elements. The first element is an accurate model for the description of a tip vortex in close proximity to the propeller tip (see chapter 4). The second is a detailed description of the amplitude as well as frequency band of broadband pressure fluctuations.

The mechanism for sound production by vortex cavitation is often present in the case of full-scale ship propellers, in the form of a stationary tip-vortex cavity together with an upstream wake excitation (chapter 2). The important question that still remains is: how relevant is this mechanism for full-scale propellers? Ships that suffer from broadband pressure fluctuations often also suffer from the effect of the dynamics of sheet cavitation. When cavities implode, high amplitude sound is produced. Because the tip vortex cavity is difficult to identify on full scale, its importance might be underestimated. The broadband sound found on model scale, described in this thesis, is found in the same frequency band as on full-scale. This thesis is concluded by a number of recommendations for improvement and for further study.

SUGGESTIONS FOR FURTHER STUDY

Model The model for the resonance frequency of tip vortex cavitation is essentially a 2D model (chapter 2). The underlying assumption is that the vortex cavity is several cavity diameters long in axial direction. In the present study the cavity satisfies this criterion for the case of a stationary wing (chapters 3 and 4) and the case of a propeller (chapter 2). The question remains how short the cavity can be and still be described by the model developed in chapter 2.

Small cavities are also more directly influenced by the local conditions in the wake peak from upstream. It is then less clear which parameters to use for the vortex circulation Γ and the roll-up parameter β (chapter 4). The global values of these parameters, valid in a large part of the propeller disk, are an appropriate first approximation for extended tip-vortex cavitation. As smaller cavities require an accurate representation of inception for each blade passage, this will pose an experimental challenge. The dominant sound production could in that case be related to the isolated implosion dynamics of the tip sheet cavity. The resonance frequency of the tip vortex in that case is less relevant.

Detailed high-speed video observations of the sheet cavity implosion synchronized with sound measurements could give more insight in the mechanism of this sound source.

The roll-up parameter β is the single remaining empirical value that is unknown in the the model for resonance frequency. The fit of figure 4.14 in chapter 4 shows a distinct trend of this parameter as function of the lift coefficient. The value for β obtained in chapter 2 fits well within this range. It is suggested to further study the relation of the β parameter as function of the gradient of the local loading close to the blade tip.

The question remains whether dissolved gas is relevant for the size of a stationary tip vortex cavity on full scale. Due to model scale issues it should be considered for model experiments. The current approach was to decrease the dissolved gas concentration. An alternative would be to account for the cavity pressure by addition of a partial gas pressure. This then replaces the vapour pressure condition in the estimation of the size of the cavity, using the numerical integration of the non-cavitating flow field.

Full scale The main path towards mitigation of broadband pressure fluctuations is the understanding of the sources of excitation. Here only the upstream wake was shown to be able to strongly excite the tip vortex cavity. On full scale there are a variety of upstream bodies (the hull, an inclined shaft or shaft brackets) and downstream bodies (the rudder) that could excite the tip vortex cavity. From a design point of view it is beneficial to know the maximum level of the excitation of the tip-vortex cavity that does not give significant sound production.

The findings in the present study give insight in the center frequency of the broadband pressure fluctuations of full scale propeller flows. The sources of these are typically hard to study, due to the limited optical access and limited availability of proprietary ship trial data. The time traces of measured sound in chapter 2 show amplitude and phase modulation. These contribute to the broadband character in the frequency spectrum of the initially tonal sound source. Johan Bosschers at MARIN is currently studying the shape of the broadband hump on full-scale ships. This is the next step in the empirical modeling of broadband pressure fluctuations.

Cavitation tunnel In the present study all experiments were performed in the cavitation tunnel at the Delft University of Technology. Due to the age of the tunnel, each separate experiment turned out to require replacement of one or more components. These updates included: a new test section for increased optical access, a closed-loop motor-control system to keep the free stream velocity stable, and finally electronic force sensors on the model propeller shaft to replace the analog balance arms.

The main concern in using the cavitation tunnel for further research is the water quality. It was shown in chapter 3 that dissolved gas can affect the size of a stationary tip-vortex cavity. This results in a change of the cavity resonance frequency. A representative low concentration of dissolved gas is required when investigating cavitation as source of sound production or erosion.

Currently there is no dedicated facility available at the Delft cavitation tunnel for degassing of the tunnel water. Also, the pressure in the tunnel could only be reduced with respect to atmospheric pressure. Both contributed to a relatively high concentration of

dissolved gas. To better control the gas content, it should be made possible to increase the static pressure in the tunnel.

The storage vessel that was used to lower the water level in the test section, is one of the oldest parts of the tunnel. Together with the pipes connecting it to the tunnel, these are the last parts still made of iron. After each increase of the water level, rust was introduced into the water. This contamination decreased optical access in the test section. If the system in the basement, including the storage vessel, filter system and plumbing, is replaced, then a dedicated degassing facility should be added.

The model propeller drive train is the other old part of the tunnel. Due to the limited motor torque, the maximum propeller rotation rate is limited. The reliability would be increased and the parameter range would be extended when the motor, bearings, seals and forces sensors are replaced. The combination of a high propeller rotation rate and increase in tunnel pressure, would make the facility more suited for cavitation erosion studies.

The main tunnel impeller suffers from cavitation at free stream velocities above 3 m/s. For acoustic studies, the level of background noise would be reduced by the replacing of the tunnel impeller.

REFERENCES

BOSSCHERS, JOHAN 2009 Investigation of Hull Pressure Fluctuations Generated by Cavitating Vortices. In *Proceedings of the First Symposium on Marine Propulsors*. Trondheim, Norway.

ACKNOWLEDGEMENTS

Research is essentially never finished. There is eventually a moment when it is time to stop and pass on your findings to others. There can be no end without a beginning. This beginning for me were the lectures by Harry Hoeijmakers, on the derivation of the Navier-Stokes equations. He was able to excite me for Engineering Fluid Dynamics. During these four years he was my mentor in the necessary preparations to undertake my biggest project to date.

In August 2011 he subtly transferred me to the capable care of Tom van Terwisga. If I was ever to undertake a Ph.D. project, it would be experimental research into vortex cavitation. I appreciate the personal touch to my supervision, always interested if I was still enjoying myself. I could always count on excited appreciation whenever I presented an experiment proposal, new results or a draft publication.

He was also the one to introduce me to the experts in the field to support my struggle for understanding. These were usually in the form of informal meetings in Wageningen with: Gert Kuiper, Do Ligtelijn, Edwin van der Weide, Faraz Khatami and Henry Bandringa. In the official counterpart we could get a feel for applications at FlowServe, IHC, Wärtsilä and MARIN. I am sure that by relying on their experience, I have been saved from many more problems.

Others that shared in the wonderful world of cavitation were Evert-Jan Foeth, Erik van Wijngaarden, Martijn van Rijsbergen and Johan Bosschers. Thank you for help in propeller design, interpretation of measurements, sharing conferences and getting to know the people behind the cavitation research at MARIN.

To fundamentally understand sound production by vortex cavitation I have had the privilege to work with Johan Bosschers. In the three days we could find in his full schedule to discuss my experimental data, I have received inspiration to fill three years of analysis. I am grateful that I could use his model to its full potential and that I could provide experimental evidence to support his hypotheses. This resulted in a fruitful discussion with Roger Arndt on the original 'singing' vortex phenomenon.

The experimental facility upgrades have truly been a team effort. In the initial stages by Oleksandr Zverkhovskyi, René Delfos, Peter Poot, Hans van der Hek, Frits Sterk, Steve van Herk, Adri van der Velde, Jan Kouwenhoven, Jasper Ruijgrok and others who have been involved. The measurements have been made a success by Jerry Westerweel, Edwin Overmars and Jan Graafland. Thank you for this cooperation. There can be no better example of a professor in experimental fluid dynamics, than one that goes swimming. Thanks to Jerry Westerweel for sharing a lot of laps in the great swimming pool De Windas, with the best measurement equipment I could have. My life at the office of the Laboratory of Aero & Hydrodynamics has been made possible and pleasant by Ria van der Brugge-Peeters and Caroline Legierse, Ad den Hollander, Rob van den Boogaard and Dineke Heersma.

Hard times are made bearable and success is made sweet by the people you share it with. In the first years Sedat Tokgöz would tell me it will all work out in the end, 'don't worry'. If only I would have known then, thank you for the great times together. All the fun we have had at the laboratory with: Hyoungsoo, Gosse, Jerke, Greta, Henk, Norbert, Arati, Melika, Hamza, Joost, Mark, Daniele, Mark, Maurice, Andries, Sasha, Marcel, Arnoud, Pedro, Ernst Jan, Aris, Mathieu, Florian, Sita, Marieke, Dries, Mark, Jasper, Manu, Wim-Paul, Daniel, Christian, Gerrit, Sören, Saad and Gem, was a perfect way to enjoy my time at the university.

My academic career is made possible by my parents, always stressing the value of education. It was good to experience academia and share in my fathers feelings of industry. My engineering career was kick-started by all the projects with friends, thank you for those awesome times. I feel honored to defend this thesis with my brothers at my sides. My final expression of gratitude goes to Rozemarijn. She is there for emotional support and is undoubtedly the most enjoyable part of a conference in an exotic place. Thank you for sharing with me.

CURRICULUM VITÆ

Pepijn Christianus PENNINGS

8-10-1986 Born in Enkhuizen, The Netherlands.

EDUCATION

1990–1998 Primary education
Openbare basisschool 't Vierspan, Grootebroek, The Netherlands

1998–2000 Secondary education
Martinus College, Grootebroek, The Netherlands

2000–2004 Secondary education
Atheneum: Natuur en Techniek / Natuur en Gezondheid
Hendrik Pierson College, Zetten, The Netherlands

2004–2011 B.Sc. and M.Sc. in Mechanical Engineering
University of Twente, Enschede, The Netherlands

2011–2016 Ph.D. Delft University of Technology, The Netherlands
Thesis: Dynamics of Vortex Cavitation
Promotors: T.J.C. van Terwisga & J. Westerweel

EXPERIENCE

2008–2009 World Solar Challenge 2009
Aerodynamic design, construction and testing of solar powered car
Preparation and participation during three month stay in Australia

2011 Cooperation between University of Twente and Vostermans Ventilation
Development of design method for efficient axial fans
Four month project including prototype testing

LIST OF PUBLICATIONS

4. **P.C. Pennings**, J. Westerweel, T.J.C. van Terwisga, *Cavitation tunnel analysis of radiated sound from the resonance of a propeller tip vortex cavity*, International Journal of Multiphase Flow (accepted, in press)(2016).

3. **P.C. Pennings**, J. Westerweel, T.J.C. van Terwisga, *Flow field measurement around vortex cavitation*, Experiments in Fluids **56** (2015).

2. R. Arndt, **P. Pennings**, J. Bosschers, T. van Terwisga, *The singing vortex*, Interface Focus **5**, (2015).

1. **P.C. Pennings**, J. Bosschers, J. Westerweel, T.J.C. van Terwisga, *Dynamics of isolated vortex cavitation*, Journal of Fluid Mechanics **778**, 288–313 (2015).